Genesis and controls on mineralization at the Hammer Zone silver showing, Mount Mye Trend, hosted by the Anvil Batholith, South-Central Yukon

by

Michael A. Rogers

A thesis submitted in partial fulfillment of the requirements for the degree of

Master of Science

Department of Earth and Atmospheric Science

University of Alberta

Abstract

When Silver Range resources acquired the Keg property in 2010, one of the prospects included was the Hammer Zone. Ensuing mapping and surface sampling found the Hammer Zone to be a small, bonanza-grade, epithermal silver system contained entirely within the Anvil Batholith. Initial petrographic observations described silver as being hosted by galena in rhodochrosite veins. However this study disagrees with galena as the primary host to silver, and suggests the majority of silver is hosted by freibergite found as crystalline inclusions in sphalerite and alongside galena.

Geochemical studies classify the Anvil Suite granite, primary lithology of the Anvil Batholith, as an ilmenite series, calc-alkaline, peraluminous, S-type granitoid forming from low degrees of partial melt, possibly in a post-collisional setting. Previous studies on the age of the Anvil Suite granite found it to be 106.6±1.0Ma. In addition previous studies also found alteration associated with the Hammer Zone to be around 100.6±1.1Ma, at least 3.8 million years younger. This study believes a difference in ages that great means the Anvil Suite granite is not the causal heat source for the Hammer Zone mineralization.

The Hammer Zone mineralization comprises four phases, identified by the gangue mineral hosting the sulfide mineralization. Calcite veining and associated sulfide mineralization including silver bearing minerals, dyscrasite, pyrargyrite, stephanite and acanthite constitute the first phase. The next phase involves quartz veining and minor amounts of sulfide mineralization; no silver is present in this paragenetic phase. Large rhodochrosite veins and an uptick in the amount of sulfides present including, sphalerite, galena, arsenopyrite and most importantly silver-bearing freibergite constitute the third phase of veining. The final phase of veining is composed of chlorite and minor quartz veining alongside hematite staining of the host rock Anvil Suite granite.

Stable isotope analysis of the carbonate paragenetic phases revealed that the initial fluid responsible for mineralization is meteoric water. The analysis also outlined the influence of a second source of fluid or stable isotope reservoir. In the calcite phase of mineralization there are two major influences, the sedimentary rocks hosting the Anvil Batholith and magmatic fluid. The quartz and rhodochrosite phases shows a dominant influence of only one other stable isotope reservoir, magmatic fluid. Analysis of carbon and oxygen isotopes in the carbonate phases also highlighted a change in depositional mechanism from boiling in the calcite phase to mixing in the quartz and rhodochrosite phases. All the conclusions drawn from studying stable isotopes are supported by fluid inclusions.

Mineral chemistry analysis using electron microprobe analysis and laser ablation inductively coupled plasma mass spectrometry discovered that in addition to influential fluids, the fluid chemistry changed considerably through the paragenetic phases. During deposition of the calcite phase, the fluid was reducing and low in sulfur. During the quartz and rhodochrosite ore stages there was a dramatic change in fluid chemistry to high sulfur, oxidizing fluid.

Through these changes in fluid chemistry and proportions of source fluids this study hypothesizes that the Hammer Zone moved from deposition akin to a low sulfidation system to closer to a high sulfidation system.

Preface

The project for this MSc. was coordinated by Dr. Sarah Gleeson, of the University of Alberta, and Archer Cathro. The author spent the summer of 2013 working in the Yukon, collecting field and core samples from the Keg Camp, Hammer Zone and Whitehorse core library of the Yukon Geological Survey. These samples were sent to Edmonton and work commenced on the thesis September 2013.

Sample collection was a collaborative effort of the author, Dr. Sarah Gleeson and Laurence Pryer, with all subsequent Edmonton based sample selection for analytical methods performed by the author. Many analytical techniques were used as part of this thesis, X-Ray Diffraction (XRD) was performed with the assistance of Dr. Diane Caird, electron probe micro-analysis (EPMA) with Dr. Andrew Locock, laser ablation secondary ion mass spectrometry (LA-ICP-MS) with Dr. Yan Luo, strontium isotope analysis by Chiranjeep Sarkar, LA-ICP-MS geochronology of monazites with Andy DuFrane and TIMS analysis of zircons by Larry Heaman (All U of A). In addition, Steve Taylor performed carbonate isotope analysis at the Univeristy of Calgary and oxygen isotope analysis of quartz was performed by Fred Longstaffe at the University of Waterloo.

The author created all figures and collected all samples for analysis unless otherwise stated.

Acknowledgements

Primarily I would like to acknowledge Dr. Sarah Gleeson for her endless patience, guidance and support through this master's thesis. Through her many hours of hard work and edits, I was able to complete such an in depth geochemical study. The great Archer Cathro crew of Mark Alban, Levi Knapp, Matt Dumala, and many more I have forgotten deserve endless credit for helping me sample and saw my way through core in the Whitehorse core library of the Yukon Geological Survey. I would also like to acknowledge Laurence Pryer, Neil Beaton, Joseph Magnall, Devon Smith and many more fellow graduate students at the University of Alberta for listening to even my most indecipherable rambling and helping me through times of scientific writers block. In addition there are many more University of Alberta staff and faculty members I would like to thank; Dr. Jeremy Richards for his help and guidance, primarily in the use of his fluid inclusion lab, but also with general questions about the direction of some of the finer parts of the thesis, Dr. Andrew Locock for all his guidance using and analyzing subsequent data from the EPMA, Dr. Yan Luo for her help with the LA-ICP-MS in the Arctic resources lab, Dr. Andrew DuFrane for his help with LA-ICP-MS analysis of monazite and Dr. Larry Heaman for his help with TIMS analysis of zircons.

A Collaborative Research and Development Grant alongside Archer Cathro primarily provided funding for this thesis to Sarah Gleeson courtesy of the Natural Sciences and Engineering Research Council of Canada NSERC, and subsequently teaching assistantships provided by the University of Alberta.

Table of contents

List of Tables

List of Figures

Chapter 1

Chapter 2

Chapter 3

Chapter 4

Chapter 5

Chapter 1: Introduction

1.1 Mineral Exploration in the Yukon.

Mineral exploration contributes significantly to the economy of the Yukon (Pigage et al., 2014). Historically, mineral exploration has been focused on gold deposits, as a result of the Klondike gold rush in the late 19th century. Despite this, there is a history of exploring for other commodities (Fig. 1.1A). For example, past and present exploration/mining projects for other commodities include (Lewis, 2009): base metal sedimentary exhalative (SEDEX) deposits (e.g. the Anvil and Faro Mines), base metal volcanogenic massive sulfide deposits (e.g. Marg deposit), porphyry copper deposits (e.g. Casino mine), skarn tungsten deposits (e.g. Mactung Mine) and polymetallic epithermal silver deposits (e.g. Keno Hill district).

In the Central Yukon (Anvil Belt), a linear band of SEDEX deposits was identified in the Faro area, (Faro deposit outlined in Fig. 1.1A: Cathro, 1967). This band of deposits includes the Faro, Vangorda and Grum deposits. To the north of the Anvil Belt prospectors conducted regional exploration projects, but only small mineralized base metal and silver prospects were found. These included the Keg, Owl/Zeno, Archimedes, Marks, Rebel and Cody-Snap-Risby-Cirque properties. In 2010, Silver Range Resources purchased these properties, bringing them together into the larger "Keg Property" (Fig. 1.1B; 1.2). This property includes the Hammer Zone prospect, which is the focus of this study.

Since 2011, Silver Range Resources' focus has been on extensive outcrop mapping of the Keg property, splitting it into 24 mineralized zones. Soil and rock-chip sampling was carried out, followed by drilling of the most interesting prospects. The surface expression of the mineralization within the Keg property forms two parallel, northwest trending belts; the Tay Trend to the north and Mount Mye Trend to the south (Fig. 1.2; Dumala, 2014). Sedimentary strata ranging in age from Cambrian to Jurassic host the Tay Trend prospects, which run sub-parallel to a number of Cenozoic thrust faults (Pigage and Cordey, 2004). The Mount Mye trend of prospects is almost entirely hosted by the Cretaceous Anvil Batholith, and includes the Hammer Zone prospect.

The Hammer Zone is located in the north East of the Anvil Batholith. It lies in a glacially cut-valley (Dumala, 2014), and was discovered after following up on an anomalous silver assay result obtained from a soil-sample. Further soil and rock chip sampling returned silver grades of up to 16,985 g/T (Dumala, 2014) and drilling started in 2012 with twenty-three holes. The Hammer Zone comprises 3 sub-vertical, space filling, quartz and carbonate veins with high silver (16,985 g/T), lead (8.41%) and zinc (8.47%) contents (Dumala, 2014). Company geologists interpret the Hammer Zone veins to be an example of polymetallic, epithermal-style, mineralization similar to the Bellekeno vein deposit (Alexco Resources) in the Keno Hill district (Lewis, 2009, Dumala, 2014). Since this thesis began, Silver Range resources have sold the property.

The next section (Ch. 1.2) discusses the main features of epithermal deposits to provide a context for the results presented in this study.

1.2 Epithermal mineralization.

Epithermal deposits are a very diverse group, and contain a variety of metals in various tectonic settings. Most epithermal deposits form at shallow levels in the crust (1-2km), at temperatures under 350°C and the nature of the mineralization is controlled by: the composition of the wall rocks, the pressure and temperature of formation, chemistry and source of hydrothermal fluids and (primary or secondary) permeability (White and Hedenquist, 1990, 1995). Epithermal deposits have been divided into low-, high- and intermediate-sulfidation systems from observations of the alteration and mineralization (White and Hedenquist, 1990). This nomenclature refers to the sulfidation states of the hypogene sulfide assemblage (Sillitoe and Hedenquist, 2003).

Low sulfidation deposits form in extensional tectonic settings (Sillitoe, 2002), distal from an intrusion/heat source (Corbett and Leach, 1998). Low sulfidation deposits have an alteration assemblage dominated by low temperature clay minerals such as sericite and adularia. Less commonly, roscoelite and smectite can occur (Sillitoe and Hedenquist, 2003). Quartz alongside fluorite and barite are the dominant gangue mineral types (Sillitoe and Hedenquist, 2003). The fluids in low sulfidation systems are dilute, moderately reduced, near neutral pH fluids that are derived from the deeply circulating groundwaters (Corbett and Leach, 1998). This dilution results in fluids with

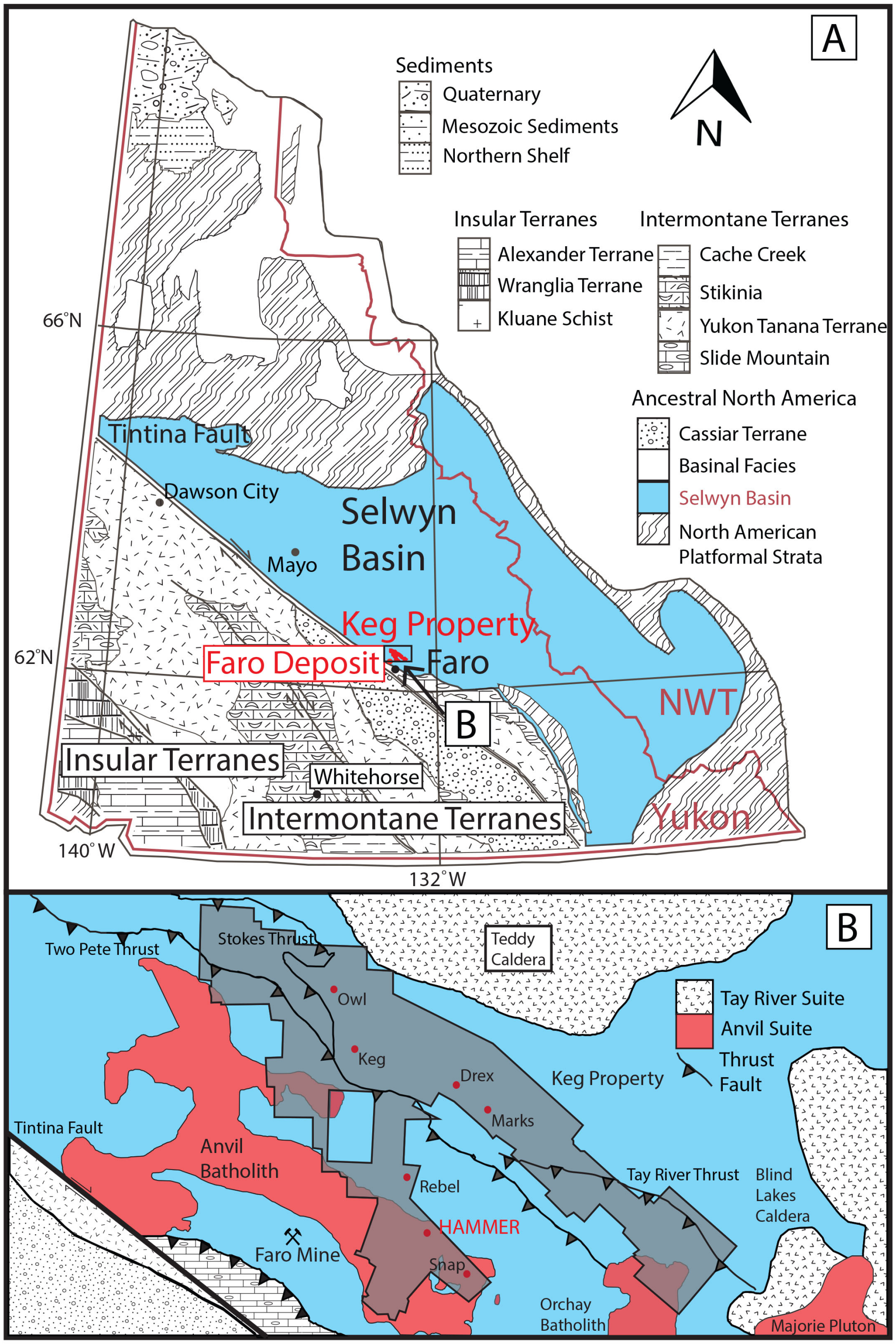

Both diagrams use the Key from Figure 1.1A

Figure 1.1A Terrane map of the Yukon Territory, and part of the Northwest Territories, highlighting the Selwyn Basin and in particular the Keg Property, Faro Deposit and the township of Faro (modified from Colpron and Nelson, 2011).

Figure 1.1B The Keg property (in grey) lies between two igneous bodies, the Teddy Caldera to the north and the Anvil Batholith to the south. Further to the south lies the dextral Tintina fault. Within the Keg Property, several of the more economically interesting prospects have been labeled.

low salinities (about 2 wt.% equivalent NaCl), and the reduced state means that the dominant sulfur species is H_2S (John, 2001). Mixing and dilution alongside boiling are usually responsible for sulfide deposition (White and Hedenquist, 2003). Low sulfidation epithermal deposits have a larger variation in mineralization styles and sulfide assemblages than other types of epithermal deposits due to the increasing number of external influences related to the larger distances the fluids travel (Corbett, 2002).

High sulfidation deposits typically form in compressive tectonic regimes more proximal to an intrusion/heat source (Sillitoe and Hedenquist, 2003). Due to the proximity to the heat source, the geological characteristics of high sulfidation deposits vary quite substantially from low sulfidation systems. High sulfidation deposits are characterized by an advanced argillic lithocap produced by highly acidic fluids (Sillitoe, 1995; 1999) of $pH<2$ (Stoffregen, 1987). The lithocap comprises high temperature aluminum-phosphate-sulfate, quartz-alunite, quartz-dickite and quartz-pyrophyllite alteration minerals (Sillitoe and Hedenquist, 2003). The gangue minerals deposited in high sulfidation deposits are dominated by silicates, predominantly; massive silicification and vuggy, residual quartz. Examples of this kind of mineralization are found at Potosi, Bolivia (Sillitoe, 1995), Yanacocha, Peru, and El Indio, Chile (White and Hedenquist, 2003). The fluids responsible for high sulfidation mineralization usually contain an abundance of magmatic volatiles (SO_2, HCl, CO_2, HF) and due to proximity to the intrusion have undergone limited dilution by groundwater (Corbett, 2002). When mixing with groundwater, the magmatic fluids cool and the sulfur species react forming sulfuric acid (Corbett and Leach, 1998). Mixing and fluid dilution are the most common processes causing sulfide deposition. The mineralizing fluids in these deposits display a range in salinities, from 2 to 45wt.% NaCl equivalent (Arribas, 1995). The hypersaline fluids have been observed at the base of high sulfidation systems or are associated with early phases of mineralization (Arribas, 1995). These fluids are interpreted as being more related to those involved in the mineralization of porphyry deposits (Arribas, 1995).

Intermediate sulfidation systems are most easily defined as a midway point between low and high sulfidation deposits. This statement is somewhat of a simplification, as it refers solely to the chemistry of the mineralizing fluids; all other factors can vary considerably. Intermediate sulfidation systems form in conservative to extensional tectonic settings and are usually hosted by felsic igneous rocks (Sillitoe and Hedenquist, 2003). The alteration associated with intermediate sulfidation deposits is dominated by illite and they have a more variable gangue mineralogy than high sulfidation systems. Silicates are present as vein filling crustiform and comb quartz often accompanied by carbonates including manganiferous varieties (e.g. at Fresnillo, Mexico and Baguio, Philippines; White and Hedenquist, 2003). Intermediate sulfidation deposits form from fluids with a higher pH to those that form high sulfidation deposits, and the fluid are, on average, more saline, with ore stage minerals regularly containing fluid inclusions with 10-12wt.% NaCl equivalent (Sillitoe and Hedenquist, 2003). However intermediate sulfidation systems have the unique characteristic of having very large fluctuations in fluid chemistry throughout their development meaning fluid inclusions can vary from <5 wt.% to 40 wt.% equivalent NaCl (Sillitoe and Hedenquist, 2003). The fluids usually contain large amounts of magmatic volatiles similar to high sulfidation deposits closest to the heat source (Giggenbach, 1995).

1.3 Thesis Aims and Outlines

Several different igneous bodies have intruded the Selwyn Basin sediments. These intrusive suites can be sub-divided based on age and composition. The band of mid-Cretaceous S-type granitoids to which the Anvil Batholith belongs has been underexplored as historically they were believed to be poorly mineralized, specifically with regards to gold. This is in contrast to older I-type and younger M-type granitoids that are associated with gold and Sn/W mineralization respectively (Hart et al., 2004; Rasmussen, 2013). As a result, these intrusions and the genesis of the associated mineralization are not well understood. However, the Anvil Batholith actually contains many silver showings (Fig. 1.2), including the Hammer Zone. Exploration for silver deposits in in the Yukon is rare, despite the presence of the Bellekeno Mine in Keno Hill, Central Yukon. The controls on silver deposition are not well understood in the area.

With this in mind, the aims of this study were developed to provide understanding about the genesis of the silver veins and what controls the mineral deposition; date the mineralizing system and the host Anvil Batholith intrusive phase and; elucidate a relationship between the two.

This paper-based thesis comprises three chapters. Chapter One gives an overview of the project and a summary of some literature on epithermal mineralization. In Chapter Two the results of the research are presented as a scientific paper. Chapter Three outlines the conclusions of the study and compares the genetic model of the Hammer Zone prospect to other deposits and puts forward possible ideas for future research.

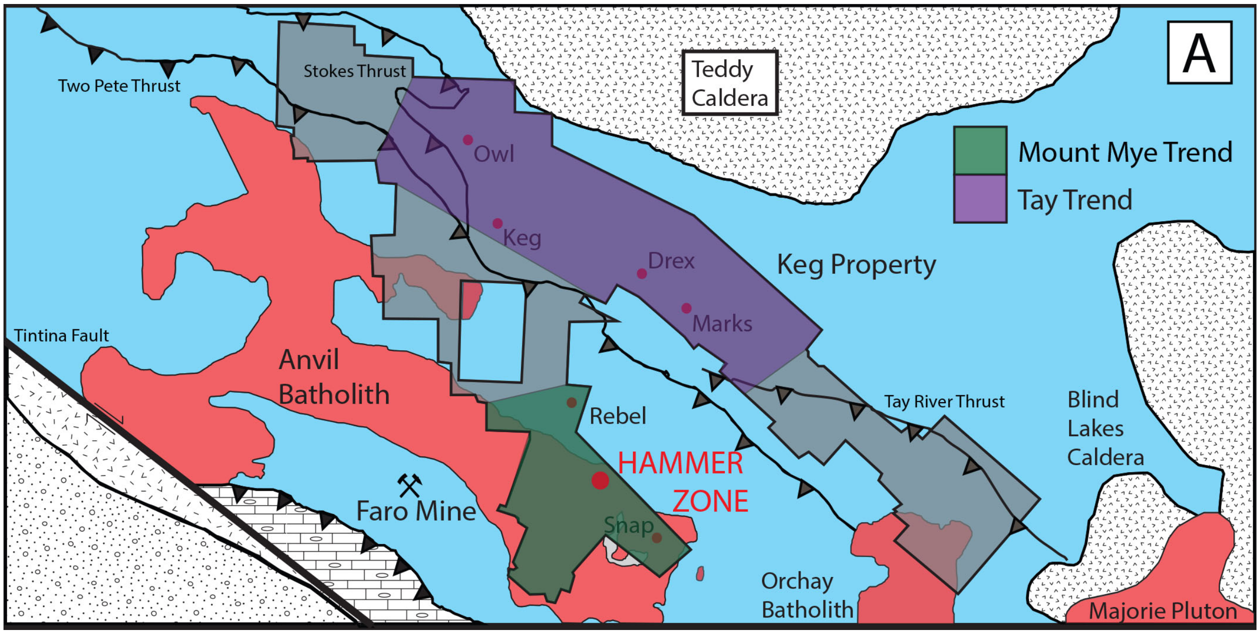

Figure 1.2 The location of the prospects of the Mount Mye and Tay Trends on the Keg property. This map uses the legend from Figure 1.1.

Chapter 2: Genesis of mineralization in the Hammer Zone, Anvil Batholith, Yukon

2.1 Introduction

Exploration in the Faro region of the Yukon increased with the discovery of the Sedimentary Exhalative (SEDEX) Faro Deposit in 1965 (Cathro, 1967; Dumala, 2014). Between 1965 and 1978 the Cretaceous Anvil Batholith and several small mineralizing systems were found, including Ag, and minor Au, epithermal systems within the batholith and skarns to the north (Foster, 1976; Betz, 1977; Foster and Holland, 1977; Holland 1977; Dumala, 2014). However, due to the lack of significant gold mineralization, exploration in the Anvil Batholith soon diminished. Later research classified the Anvil Batholith as a reduced S-type granite. Previous studies on reduced S-type granites (Hart et al., 2004) publicized a lack of (in particular gold) mineralization compared to oxidized intrusives. As a result, exploration and research on mineralization hosted by the Anvil Batholith was limited, with the exception of one publication (Mortensen and Ballantyne, 1992).

However, the Keg property contains several prospects hosted by the Anvil Batholith (Fig. 2.1). The Keg property is located roughly 30km north of the township of Faro in the south Central Yukon (Fig. 1.1a). It can be divided into two parallel ESE trending belts: the Tay Trend and the Mount Mye trend (Fig. 1.2). Each trend contains multiple mineralized showings. This study concentrates on the Mount Mye trend and, in particular, the Hammer Zone mineralization. The Hammer Zone is of interest due to the bonanza silver grades of up to 16,985 g/T. It has many similar characteristics to epithermal silver deposits: vein hosted mineralization, fracture filling gangue mineral textures, high metal grades and clay and hydrous mineral alteration associated with the veins (Dumala, 2014). However, the age and genesis of mineralization and relationship to the host Anvil Batholith are poorly understood. This study aims to elucidate this relationship using electron probe micro-analysis (EPMA), stable, (C, O,) and radiogenic isotopes (Sr) and a fluid inclusion study. In addition to investigating the nature of the mineralization, bulk rock geochemistry and U-Pb geochemistry of zircon and monazite in the host rocks are be used to try to assess the age and petrogenesis of the host rock. All the data are then integrated to form a genetic model for the Hammer Zone.

2.2 Regional Geology of the Yukon

The bedrock units of the Yukon have experienced a long geological history; beginning with the cratonization of Laurentia followed by Neoproterozoic to Mesozoic sedimentation and finally the Mesozoic accretion of allochthonous terranes (Thorkelson et al., 2005; Mair et al., 2006). Cratonization of Laurentia began roughly 2.1 Ga ago with the accretion of numerous terranes to the Canadian Shield (Norris and Dyke, 1997; Thorkelson et al, 2005). This accretion had stopped by 1.84Ga, when the final magmatic event associated with these collisions occurred and a passive margin was developed. The rocks deposited along this passive margin, between 1.4Ga to 728Ma, have been classified into four supergroups: Wernecke, Pinguicula, MacKenzie and Windermere, each with a distinct depositional environment (Hoffman, 1989; Rainbird et al., 1996; Falck, 2007). The deposition of the last of these, the Windermere Supergroup, occurred from 750Ma to 575Ma recording an unusually long period of intracontinental rifting and synrift sedimentation, preceding actual continental separation in the Cambrian (Bond and Kominz, 1984; Mair et al., 2006).

From 728Ma to 575Ma, the rifting of the Australian and Siberian paleo-continents from North America resulted in the break up of the supercontinent Rodinia (Bond and Kominz, 1984; Powell et al., 1993; Colpron et al., 2002). During the Lower Cambrian a passive margin was formed off the Western side of ancestral North America (Bond and Kominz, 1984). The change in tectonics created accommodation space into which the sedimentary rocks of the Selwyn Basin were deposited, on top of the Windermere supergroup, from the lower Cambrian to the Jurassic (Ross, 1991; Mair et al., 2006). Allochthonous terranes were accreted to the west coast of North America in the Early Jurassic to the Late Cretaceous (Coney et al., 1980; Monger et al. 1982; Mair et al., 2006), halting deposition of the sediments and converting the tectonic environment to one of compression. This compression resulted in the uplift and erosion of ancestral North America followed by decompression related plutonism in the mid-Cretaceous (Armstrong, 1988; Mair et al., 2006).

2.3 Regional Geology of the Selwyn Basin

The stratigraphy of the Selwyn Basin is summarized in a stratigraphic column, Figure 2.1

2.3.1 Sedimentary Rocks and Tectonics of the Selwyn Basin

The Selwyn Basin was deposited atop basement rocks as a number of sedimentary packages deposited continuously between the Lower Cambrian and the Late Triassic/Early Jurassic (Fig. 2.1) (Pigage, 2004). The oldest exposed unit, interpreted as the oldest rocks of the Selwyn Basin, is the Hyland Group. The Hyland Group consists of the interbedded sandstones and siltstones of the Yusezyu Formation overlain by the maroon weathering shale of the Narchilla Formation (Gordey and Anderson, 1993; Gordey, 2013). The Hyland Group was deposited during the latest Proterozoic as indicated by the presence of the trace fossil, *Oldhamia Radiata* (Hofmann and Cecile, 1981).

The first unit to be deposited on top of the Hyland Group was the Cambrian Mount Mye Formation, which now outcrops as a phyllite at greenschist facies and a quartz-muscovite-biotite schist at amphibolite grade (Pigage, 2004). Overlying the Mount Mye Formation is the Cambrian to Ordovician Vangorda Formation. The Vangorda Formation correlates with the Rabbitkettle Formation (Gordey and Irwin, 1987) and comprises grey, lustrous, quartz-rich phyllite, siltstones and limestones. The non-metamorphosed siltstones and limestones present in these units formed in an off-shelf setting (Gordey, 2013). The Menzies Creek Formation conformably overlies the Rabbitkettle/Vangorda formation and comprises mainly volcanic rocks (discussed in 2.3.2). Deposited on top of the Menzies Creek Volcanics is the Duo Lake Formation. The Silurian (Gordey, 2013) Duo Lake formation comprises black, carbonaceous, silty argillites interbedded with Menzies Creek Formation at the basal contact (Pigage, 2004). The silty grain size coupled with lack of other defining texture has prompted interpretations that the Duo Lake formation was deposited in an oxygen-starved, organism free, basinal environment (Gordey and Anderson, 1993). From the middle Devonian to the Mississippian the Selwyn Basin was subject to compression and uplift due to the Ellesmerian Orogeny (Goodfellow and Jonasson, 1986). The change in tectonic activity resulted in sediments being deposited in a fault controlled, submarine fan setting, as coarse clastic rocks, with graded bedding characteristic of sediment gravity flows. These units are named the Earn Group (Gordey, 1991; Gordey and Anderson, 1993; Gordey, 2013). Following the orogeny, as the Selwyn Basin subsided and sediments were deposited in deep-water conditions, there was a period of slightly energetic conditions during which more uniform shelf sedimentation occurred; the Mississippian Tay Formation. This unit comprises silt rich, fossiliferous limestones and calcareous siltstone (Gordey, 2013). Succeeding the shelf sediments of the Mississippian Tay Formation, and deposited in moderately deep-water, sub-wavebase conditions, is the chert dominated Permian Mount Christie Formation (Pigage, 2004, Gordey, 2013). The Jones Lake Formation unconformably overlies the Mount Christie formation (Gordey, 2013). This unit has rock types similar to the Mississippian Tay Formation, suggesting deposition occurred in a similar environment, however conodont fossils (Orchard, 1991) give a Triassic age for this unit. Sedimentation into the Selwyn Basin terminated shortly after the deposition of the Jones Lake Formation (Templeman-Kluit, 1979b). The hiatus in deposition is a result of the recommencement of accretion of allochthonous terranes and orogenesis in the Early Jurassic (Colpron et al., 2007). With the continuing accretion of terranes, the earliest exotic terranes were thrust on top of North America along the Inconnu Thrust fault (Murphy et al., 2002; Murphy et al., 2006; Gordey, 2013) and with this thickening of the upper crust, a large amount of igneous activity was initiated (see 2.3.2). The Early Tertiary, Tintina dextral strike slip fault accommodated 450km of displacement (Pigage, 2004).

2.3.2 Igneous Rocks of the Selwyn Basin

The Menzies Creek Formation contains the oldest outcropping igneous rocks in the Selwyn Basin. This unit comprises pillow basalts and massive basaltic flows consistent with a submarine setting, overlain by volcaniclastics (Pigage, 2004). The Menzies Creek Formation formed during the Ordovician and Silurian (Pigage, 2004). Geochemical analysis of the basalts classified them as within plate, alkaline basalts (Pigage, 2004).

Gabbro and pyroxenite dykes and sills found crosscutting the Rabbitkettle Formation are thought to be subvolcanic dykes and sills that fed the volcanics (Gordey, 2013).

The next period of igneous activity occurred in the Cretaceous, with three distinct periods of post-tectonic magmatism in the early-, mid- and late-Cretaceous. Each group of intrusions is classified by distinct lithologies, geochemistry, formational process, and distinct locations within the Selwyn Basin (Mortensen et al., 2000; Rasmussen, 2013). The early-Cretaceous arc magmatism started with production of I-type, oxidized, magnetite series granitoids and spatially related andesitic to dacitic volcanic rocks (Anderson, 1998, Hart et al., 2004). The Teslin Suite of intrusions (123-115Ma), located in south Central Yukon, is the most studied group of rocks belonging to this period of magmatism (Mortensen et al., 2000). The composition and mineralogy of these rocks have been interpreted to suggest that possibly they formed during continental arc magmatism that was the result of the subduction of oceanic crust under the western side of North America (Mortensen et al., 2000; Rasmussen, 2013).

The next period (115Ma-100Ma) of early- to mid-Cretaceous arc magmatism produced S-type, reduced, ilmenite>magnetite-series plutons broadly coeval with the continental arc magmas but were emplaced further inland (Rasmussen, 2013). Rocks of this composition, interpreted as genetically related, are found as far north as Alaska, offset by the Tintina fault (Werdon et al., 2004; Rasmussen, 2013). The Anvil Suite, including the Anvil Batholith, belongs to this group of intrusions. Extrusive equivalents of these units occur locally around the Selwyn basin as rhyolitic calderas (Mortensen, 2008) and ignimbrites (Thomson et al., 2011). The mineralization at the Hammer Zone has been dated at 100.6±1.1Ma (^{40}Ar-^{39}Ar), a similar age to intrusions from this period of magmatism.

The next suite of intrusions was formed in post-arc magmatic settings, and has ages between 99-90Ma. These rocks are metaluminous to peraluminous, ilmenite to magnetite-dominant plutons (Anderson, 1998, Mortensen, 2000). These felsic igneous intrusions are associated with two types of more mafic igneous rocks; lamprophyre dykes and gabbro intrusions. The Tombstone (central Yukon), Tungsten (southwestern NWT) and Tay River (southern Yukon) suites belong to this age of intrusions. Associated with this age of intrusions are several volcanic rock units including the South Fork volcanics. There have been several models produced for describing this evolution of igneous activity in the early to late-Cretaceous, the most commonly accepted model is continental arc magmatism resulting from subduction and dehydration of an oceanic plate followed by back-arc extension post slab rollback (Mortensen et al., 2000; Rasmussen, 2013).

Igneous activity during the late Cretaceous can be split into two periods, 84-78Ma and 78-67Ma. However this later stage of magmatism is less well understood and most of the geochronological constraints were made using methods of dating prone to resetting (e.g. ^{40}K-^{40}Ar). The older suite of igneous rocks comprises calc-alkaline plutonic suites emplaced during a dextrally transpressive regime (Mortensen and Hart, 2010). East of the 84-78Ma suite of rocks lies the 78-67Ma suite, these rocks are oxidized, alkaline plutonics with A-type geochemical affinities (Ray et al., 2000; Mortensen and Hart, 2010). These later suites are interpreted to have formed from crustal anatexis due to crustal thickening (Nelson and Colpron, 2007).

Igneous activity post-dating the late-Cretaceous event is under examined and poorly understood. The only published examples of post-Cretaceous igneous rocks are the 65Ma McQuesten plutonic suite and the 55Ma Ross group (Pigage, 2004, Rasmussen, 2013; Thiessen, 2013). Both these suites of rocks show A-type geochemical affinities consistent with formation in a dextral transtensional regime and extension of over-thickened crust (Pigage and Mortensen, 2004; Nelson and Colpron, 2007; Rasmussen, 2013).

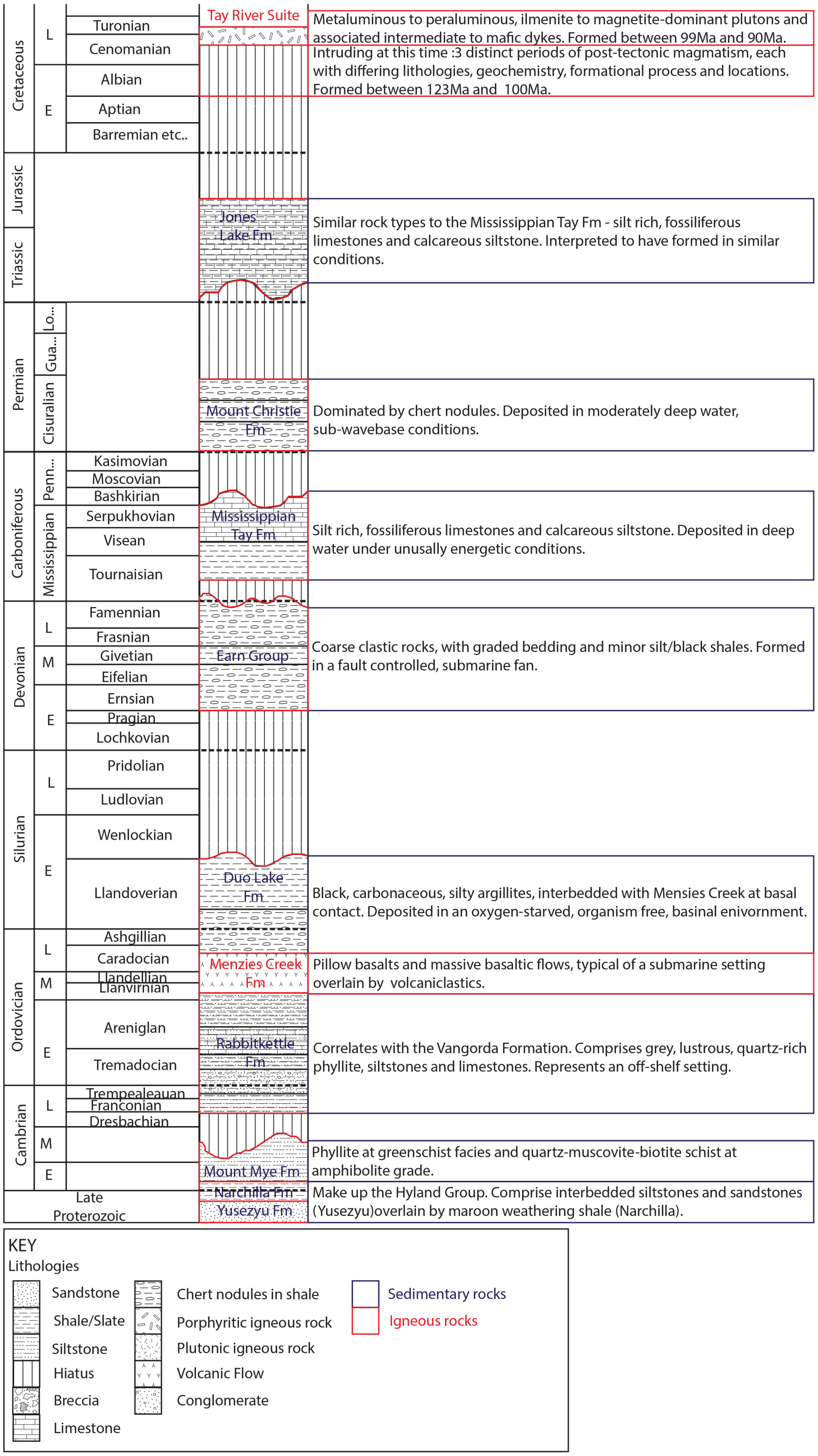

Metaluminous to peraluminous, ilmenite to magnetite-dominant plutons and associated intermediate to mafic dykes. Formed between 99Ma and 90Ma.

Intruding at this time :3 distinct periods of post-tectonic magmatism, each with differing lithologies, geochemistry, formational process and locations. Formed between 123Ma and 100Ma.

Similar rock types to the Mississippian Tay Fm - silt rich, fossiliferous limestones and calcareous siltstone. Interpreted to have formed in similar conditions.

Dominated by chert nodules. Deposited in moderately deep water, sub-wavebase conditions.

Silt rich, fossiliferous limestones and calcareous siltstone. Deposited in deep water under unusally energetic conditions.

Coarse clastic rocks, with graded bedding and minor silt/black shales. Formed in a fault controlled, submarine fan.

Black, carbonaceous, silty argillites, interbedded with Mensies Creek at basal contact. Deposited in an oxygen-starved, organism free, basinal enivornment.

Pillow basalts and massive basaltic flows, typical of a submarine setting overlain by volcaniclastics.

Correlates with the Vangorda Formation. Comprises grey, lustrous, quartz-rich phyllite, siltstones and limestones. Represents an off-shelf setting.

Phyllite at greenschist facies and quartz-muscovite-biotite schist at amphibolite grade.

Make up the Hyland Group. Comprise interbedded siltstones and sandstones (Yusezyu)overlain by maroon weathering shale (Narchilla).

Figure 2.1 The stratigraphy of the Selwyn Basin. Each formation has a short description of rock types and formational environments. Sedimentary rocks are highlighted blue, igneous rocks are highlighted red

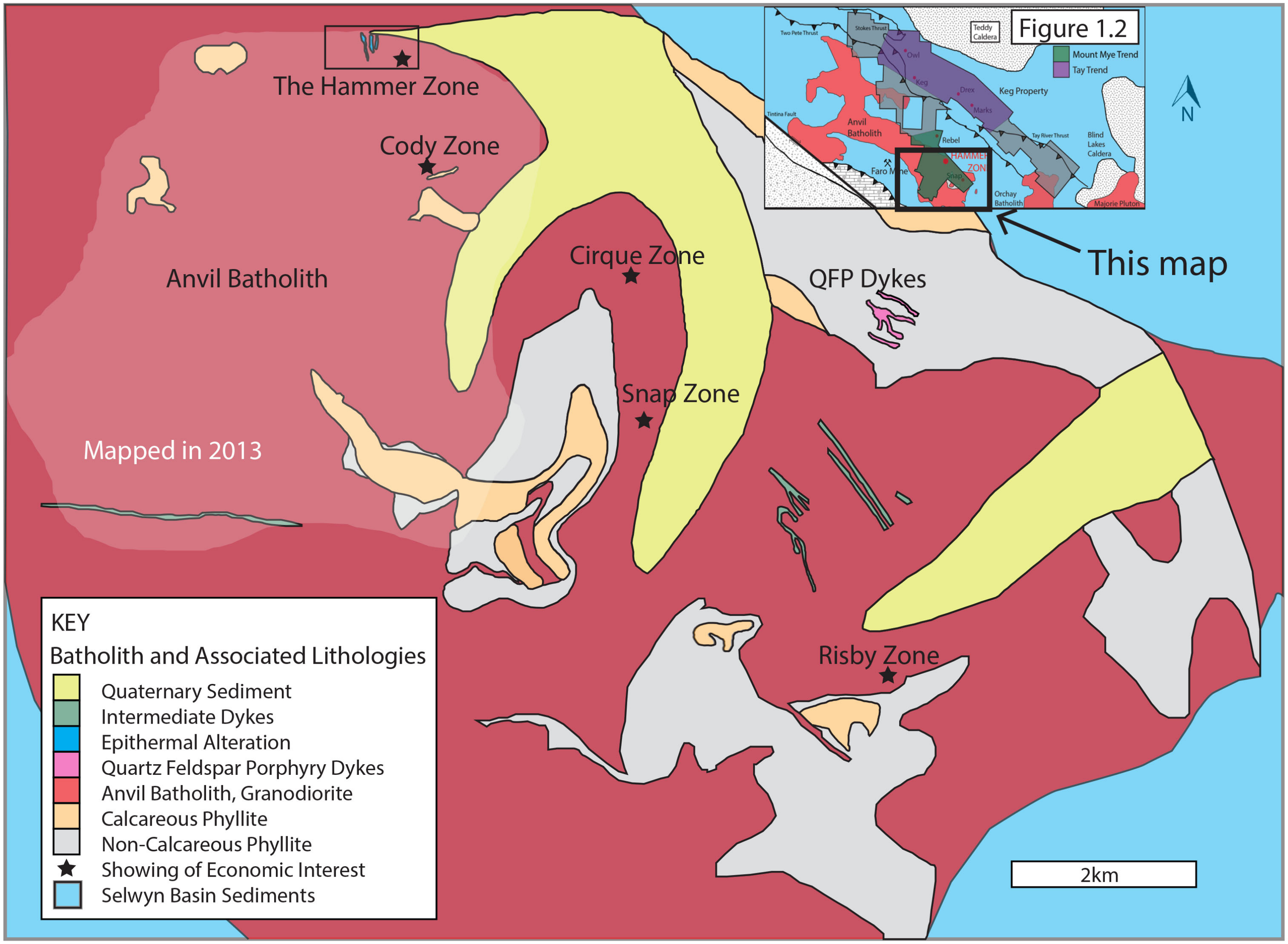

Figure 2.2: Map of the Anvil Batholith showing all prospects owned by Silver Range Resources. Hammer Zone is located in the North West of this map. The Batholith is surrounded by Selwyn Basin sediments including the Mississippian Tay and Earn Group

2.4 Property Geology

The Keg property lies to the northeast of the most eastern allochthonous terranes, the dextral Tintina fault and between two igneous bodies (Fig. 1.1B). The Keg property runs in two parallel trends (Tay and Mount Mye), which are subparallel to the regional tectonic structures (Fig. 1.1B; Fig. 1.2). Selwyn Basin sediments host the Tay Trend of prospects, which form a linear trend subparallel to the Twopete thrust. The Mount Mye trend is contained within the Anvil Batholith.

The Tay Trend of the Keg property comprises prospects hosted by the Rabbitkettle Formation, Earn Group, Mississippian Tay formation and Mount Christie Formation (Cobbett, 2012). These sedimentary units are cut by thrust faults and folded (Fig. 1.1B). The sedimentary units of the Tay Trend outcrop between the South Fork Volcanics (99-94Ma) to the north and the Anvil Batholith (109-104Ma) to the south (Pigage, 2004). There is a kilometer scale thermal aureole reaching amphibolite facies around the Anvil Batholith (Pigage and Anderson, 1985; Pigage, 2004).

The Anvil Batholith is a member of the Anvil Suite (Mortensen et al., 2000). Petrographically, the Anvil Batholith is a biotite, muscovite granitoid. Geochemically, it is an S-type, peraluminous, high-K, calc alkaline, ilmenite dominated, granite thought to have formed from low temperature partial melting of pelites via mica dehydration (Pigage 2004; Gordey, 2011; Rasmussen, 2013).

The Batholith is crosscut in several areas by dykes, which have been assigned to the Tay River suite (these dykes are thought to be feeders to the South Fork volcanics associated with the Tay River suite). These are mafic, biotite, hornblende porphyries and are about 10m.y. younger than the batholith (Mortensen et al., 2000, Pigage, 2004). The Tay River intrusives are not associated with any known mineralization.

2.5 Mineralization

The Hammer Zone outcrops as three linear recessions in the Anvil Batholith, close to the contact with the Gull Lake Formation to the northeast. Trenching across the recessive areas uncovered veins and related alteration zones. The mineralization in the Anvil Batholith was discovered through soil and chip sampling. The soil samples returned anomalous values for Zn, Pb, Ag, Sn, In, and Au in a number of locations (Appendix 1, Table 2.1 is adapted from Dumala, 2014). The Hammer Zone was recognized as a potentially lucrative prospect due to the high levels of Ag found in chip sampling, the highest values ranging from 2500 to 16985 g/T.

The Hammer Zone contains 3-4 discrete veins each with a width of 5-10 centimeters. Mineralization at the Hammer Zone comprises sulfides including: galena and sphalerite with minor arsenopyrite, pyrite and freibergite. The gangue mineralogy at the Hammer Zone was identified as quartz and rhodochrosite, supporting the initial interpretation of epithermal style mineralization. Initial studies on a few showings from the Mt. Mye trend (Robertson and Wallis, 1989) suggested that the Ag is hosted in galena. The veins are associated with sericitic, propylitic and argillic alteration. Some areas advanced argillic and silicic alteration are present in the field but not in core.

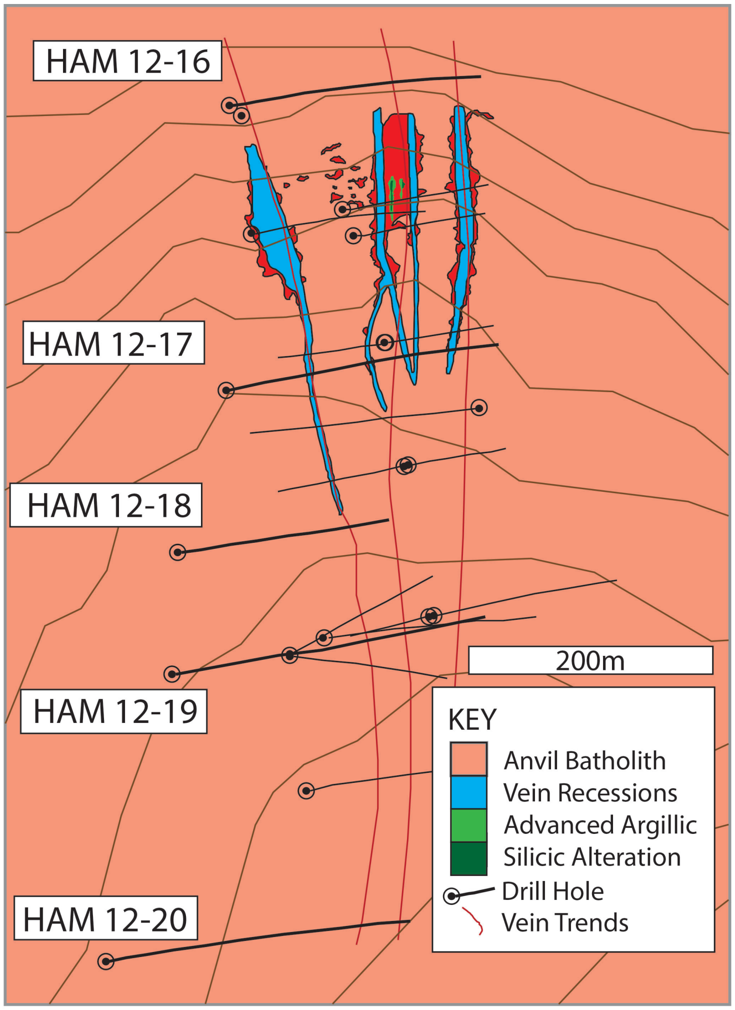

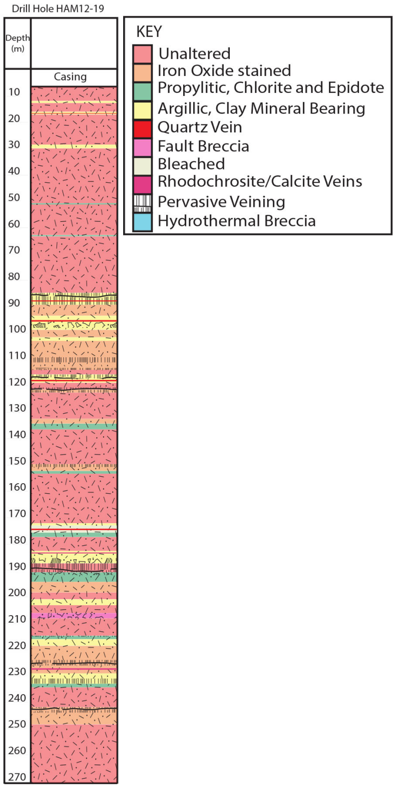

Figure 2.3 Map showing the veins and local geology of the Hammer Zone. Included is a log of core from the Hammer Zone showing extensive mineralization.

2.6 Methods and Analytical techniques

A total of 550 samples of drill core were collected from 5 holes (HAM12-16 to HAM12-20) in the Hammer Zone during the summer of 2013. Sample collection was based on lithology, alteration style and mineralization, including any paragenetic relationships of interest. Drill hole locations can be found in Figure 2.3. The core was located in the Yukon Geological Survey core library in Whitehorse, and was on loan from Silver Range Resources.

2.6.1 Petrography and EPMA

Petrography and electron probe micro-analysis (EPMA) were used to create a paragenetic sequence. Each of the 550 hand specimens were first described in the field and subsequently described in more detail in the lab. The descriptions focused on the mineralogy of the host rock and any veining or crosscutting relationships. Structural features were also noted. 90 samples were chosen for thin section analyses and sent to Vancouver Geotech Labs. Plane-polarized light (PPL), cross-polarized light (XP) and reflected light (RL) petrography was used to characterize each sample and identify sulfide and gangue mineralogy and relationships.

EPMA was used to investigate the chemistry of the sulfides and carbonates. The analyses were conducted on a JEOL 8900 instrument at the University of Alberta Electron microprobe Lab under the supervision of Dr. Andrew Locock. EPMA techniques used included electron dispersive spectrometry (EDS), wavelength dispersive spectrometry (WDS), X-ray elemental mapping, backscattered electron imaging (BSE) and secondary electron imaging (SE). Electron dispersive spectrometry was used for initial elemental identification of unknown phases; this was followed by wavelength dispersive spectrometry for quantitative information on sulfide trace element composition and/or carbonate major element composition. X-ray mapping, backscattered electron imaging and secondary electron imaging were used to qualitatively examine the spatial distribution of elements in certain phases based on elemental mass. Conditions of operation for the WDS analysis changed depending on the sample being analyzed (Appendix 1). WDS analysis required calibration from standards and, as major and minor elements were being analyzed together, several different analytical crystals were used e.g. pentaerythritol (PET), lithium fluoride (LIF), thallium acid phthalate (TAP), and a layered dispersive element (LDE). The concentrations of specific elements were calibrated to the following standards for analysis of carbonates: sanbornite for Ba, Co metal for Co, dolomite for Mg and Ca, strontianite for Sr, rhodonite for Mn, willemite and sphalerite for Zn, siderite for Fe and synthetic lead tungstate for Pb. For sulfides, the standards used were: galena for Pb and S, indium arsenide for In, gallium arsenide for As, Sb metal for Sb, sphalerite for Zn, Cu metal for Cu, Ag metal for Ag, cadmium selenide for Cd and Se, Mn metal for Mn, Sn metal for Sn, bismuth telluride for Bi and Te, and Fe metal for Fe.

2.6.2 LA-ICP-MS

Laser ablation, inductively coupled plasma mas spectrometry (LA-ICP-MS) was conducted at the Arctic resources lab in the University of Alberta under the supervision of Dr. Yan Luo. The LA-ICP-MS was used to quantitatively identify trace elements present in sulfides that were under the limits of detection of the EPMA. A Resonetics Laser Ablation system equipped with a 193 nm argon fluoride excimer laser was used with a Thermal XR ICP-MS run at medium mass resolution. For all analyses a beam diameter of 23µm was used with a laser frequency of 10Hz and laser energy of 100mJ. The sample was analyzed, without ablating, for elemental background levels for 30 seconds followed by a 40 second ablation time. Standard MASS-1 and reference material NIST-612 were used to standardize for the unknowns. The elements measured for sulfide analyses ^{51}V, ^{59}Co, ^{60}Ni, ^{61}Ni, ^{65}Cu, ^{66}Zn, ^{67}Zn, ^{69}Ga, ^{74}Ge, ^{75}As, ^{78}Se ^{95}Mo, ^{98}Mo, ^{107}Ag, ^{109}Ag, ^{111}Cd, ^{114}Cd, ^{121}Sb, ^{123}Sb, ^{125}Te, ^{197}Au, ^{202}Hg, ^{205}Tl and ^{209}Bi on the MASS-1 standard and ^{85}Rb, ^{88}Sr, ^{89}Y, ^{90}Zr, ^{133}Cs, ^{137}Ba, ^{139}La, ^{140}Ce, ^{141}Pr, ^{146}Nd, ^{147}Sm, ^{153}Eu, ^{157}Gd, ^{159}Tb, ^{163}Dy, ^{165}Ho, ^{166}Er, ^{169}Tm, ^{172}Yb, ^{175}Lu, ^{178}Hf, ^{232}Th, ^{238}U on the NIST-612 reference material. As well as standardizing to an external standard, an internal standard was used. In this case the weight percentage of Fe, as measured by WDS analysis, was used for all three sulfides analyzed. A single faraday detector was used to detect isotopes of the different elements separated depending on their mass to charge ratio in the mass spectrometer. The Iolite computer program was used to process the raw data from the

LA-ICP-MS. The effectiveness of the MASS-1 standard and NIST-612 reference material was judged based on the values analyzed compared to the published values on GEOREM. Analyzing the accuracy of analyses on the known standards using GEOREM, allowed verification of the detection limits calculated through Iolite. Limits of detection varied depending on whether the unknowns or the standards were being analyzed. For the unknowns, limits of detection were calculated by Isoplot and given in the same spreadsheet. These varied by analysis point and element analyzed. Each limit of detection was converted into a limit of quantification, which decided the points of analyses to use.

2.6.3 Carbon and Oxygen Isotopes

Powdered samples of carbonate veins from different generations of the paragenesis were prepared at the University of Alberta using a hand drill. The samples were sent to Steve Taylor at the University of Calgary's Isotope Science Lab for analysis. The powders were dissolved in anhydrous phosphoric acid at 25°C overnight and the CO_2 produced was analyzed in a Thermo Finnigan Gasbench mass spectrometer coupled to a Delta Vplus to determine the $^{13}C/^{12}C$ and $^{18}O/^{16}O$ (and $\delta^{13}C$ and $\delta^{18}O$ values) ratios (Kim et al., 2009). Internal lab reference materials were used to standardize the measurements and correct for any drift in the machine during analysis. All internal lab standards were calibrated to international VPDB (Peedee Belemnite) and VSMOW (standard mean ocean water) standards to ensure accuracy in the $\delta^{13}C$ and $\delta^{18}O$ values produced. The $\delta^{13}C$ and $\delta^{18}O$ values have an uncertainty of 0.2‰.

Powdered quartz vein samples were analyzed for oxygen isotopes at the Laboratory for Stable Isotope Science, University of Western Ontario. For all samples, 8mg of sample powder was loaded in sample holders and evacuated overnight at 150°C. Following this the samples were placed in nickel reaction vessels and heated for a further 3hours at 300°C and then reacted at 580°C with ClF_3 overnight (Borthwick and Harmon, 1982). The released oxygen was converted to CO_2 over red-hot graphite for isotopic measurement using a Prism II dual inlet, stable isotope ratio mass spectrometer to find the ratio of $^{18}O/^{16}O$. The results are displayed with the δ notation in parts per thousand (‰) and are standardized against VSMOW. Sample reproducibility was better than ±0.1‰ (Polat and Longstaffe, 2014).

The $\delta^{13}C_{PDB}$ and $\delta^{18}O_{SMOW}$ values of the fluid that precipitated the quartz and carbonates were back calculated. Each calculation of fractionation required a temperature of formation from fluid inclusion studies and a 1000lnα fractionation factor (between two compounds), unique for each mineral and isotopic system.

In the data collected for calcite, a spread in both the oxygen and carbon isotopic data due to boiling complicated the back-calculation to an initial fluid value. For both these isotopic systems, a plot of fractionation curves for various initial fluid values, over a range of temperatures was used to estimate an initial fluid composition before boiling. The fractionation factors used were O'Neil et al. (1969) for oxygen and Ohmoto and Rye (1979) for carbon. The range of temperatures included those found via fluid inclusion studies.

For oxygen isotopes in quartz, homogenization temperatures from each sample were used. If no homogenization temperature had been measured for a sample, an average temperature for that paragenetic stage was used. For all the samples, the temperature was used with a quartz-water fractionation factor from Clayton et al. (1972).

There are no published fractionation equations between a fluid and rhodochrosite thus the 1000lnα had to be calculated from 1000lnβ (reduced partition ratio) values. For $\delta^{13}C_{PDB}$ analyses,

$$1000\ln\alpha(\mathrm{rds\text{-}CO_2}) = 1000\ln\beta(\mathrm{rds}) - 1000\ln\beta(\mathrm{CO_2})$$

where: $1000\ln\beta(\mathrm{rds}) = R_0+R_1(10^3/T)+R_2(10^6/T^2)+R_3(10^9/T^3)+R_4(10^{12}/T^4)$

$$1000\ln\beta(\mathrm{CO_2}) = C_0+C_1(10^6/T^3)+C_2(10^9/T^3)+C_3(10^{12}/T^4)+C_4(10^{15}/T^5)-C_5(10^{18}/T^6)$$

where R_x and C_x are constants and T is temperature in Kelvin (Deines, 2004; Chacko pers. comms.).

For $\delta^{18}O_{SMOW}$, a similar method was used.

$$1000\ln\alpha(\text{rds-}H_2O) = 1000\ln\beta(\text{rds}) - 1000\ln\beta(H_2O)$$

$1000\ln\beta(\text{rds})$ has already been calculated, thus $1000\ln\beta(H_2O)$ must be calculated (Chacko and Deines, 2008):

$$1000\ln\beta(H_2O) = H_0+H_1(10^6/T^3)+H_2(10^9/T^3)+H_3(10^{12}/T^4)$$

2.6.4 Sulfur Isotopes

Samples of galena and sphalerite from paragenetic sets were analyzed for sulfur isotopes. Samples were separated from the vein using a hammer and tweezers and subsequently powdered using a mortar and pestle. The samples were analyzed at the Isotope Science Laboratory, University of Calgary using the method of Glesemann et al. (1994) by Continuous Flow-Isotope Ratio Mass Spectrometry (CF-EA-IRMS) using a Carlo Erba NA 1500 elemental analyzer interfaced to a VG PRISM II mass spectrometer. The sulfide samples were combusted at 1050°C in a high-temperature combustion reactor. The SO_2 gas produced was transmitted to the mass spectrometer where the sulfur isotopic ratio was measured. The raw data are normalized to the international standard VCDT (Canyon Diablo Triolite). The analyses produced are precise to 0.3 ‰.

2.6.5 Strontium Isotopes

Chiranjeeb Sarkar at the University of Alberta analyzed the isotopes of strontium in calcite and rhodochrosite using methods described by Buzon et al. (2007). Twelve powdered samples of carbonate were prepared using a hand drill to extract at least 0.1mg of sample. The sample was dissolved in concentrated HCl overnight. Any solid residue, most likely from inclusions of quartz, was removed by decanting the carbonate solution into another container. Column chemistry was used to separate the strontium from all other elements. The total strontium solution was analyzed for isotopic ratio on the Neptune multi-collector inductively coupled plasma mass spectrometer (MC-ICP-MS), with each strontium isotope (^{84}Sr, ^{86}Sr, ^{87}Sr, and ^{88}Sr) collected on a different faraday cup. The $^{87}Sr/^{86}Sr$ was calculated from these results. The reference material used was SRM987, an internationally accepted standard. The samples returned results with an internal error of 0.00001 to 0.00003.

2.6.6 Whole Rock Geochemistry

Half core samples of the host rock granodiorite, granodiorite altered by Hammer Zone mineralization and pegmatite were sent away to ACTLABS for the whole rock geochemistry *4E Research and ICPMS* package. This package covers all the essential major, minor and trace elements needed for classification of igneous rocks. The samples were dried and crushed to better than 70% passing 2mm grain size and then a 250g aliquot was pulverized to better than 75μm. The *4E Research and ICPMS* package uses various methods for different elements. For trace element analyses, the sample undergoes instrumental thermal neutron activation (INAA) where an element is irradiated, allowed to decay and the gamma-ray given off during that decay is measured, with each element's gamma-ray having a unique energy (see: Hoffman, 1992). For major and selected trace elements the method involves mixing the sample with lithium metaborate/lithium tetraborate and fusing the resultant material with a graphite crucible before dissolving in nitric acid, to give a solution for ICPMS analysis. Base metals are dissolved using four different acids, HF, HNO3, HCLO4 and HCl. With each acid different silicate phases are dissolved. For all methods, the samples were analyzed using a Varian Vista ICP and one internal standard is processed for every 11 unknowns. This internal standard is calibrated to an internationally recognized standard. All analyses measured in wt% have a limit of quantification of 0.01%. Analyses reported in ppm have a limit of quantification between 0.1 and 1 ppm.

2.6.7 U-Pb Dating (LA-ICP-MS and TIMS)

Laser ablation inductively coupled plasma mass spectrometry was utilized to find an *in situ* U-Pb age of monazites from the alteration assemblage in thin section. Analyses were conducted under the supervision of Andy DuFrane in the Radiogenic Isotope facility in the Department of Earth and Atmospheric Sciences, University of Alberta using a NuPlasma MC-ICP-MS and the UP213 laser ablation system (Simonetti et al., 2006).

Monazite from Madagascar, analyzed by ID-TIMS in Larry Heaman's lab was used as a reference material and standard. The spot size for the reference monazite was 10μm and for the unknown monazites was 20μm. The monazites were identified by EDS on the EPMA before being analyzed on the LA-ICP-MS. Images of all monazites were taken to achieve accuracy in placing the spots. Many samples displayed large amounts of initial Th thus a correction was applied to try and achieve a more accurate age. However this correction caused the data to become less concordant and was disregarded. In order to correct for common lead inclusion all analyses were plotted on a Tera-Wasserberg diagram, rather than a Concordia plot.

Thermal Ionization Mass spectrometry was utilized to find the U-Pb crystallization ages of zircons from the host granodiorite. A full method for separation and analysis of zircons can be found in Heaman et al. (2002). The zircons were separated from the host granodiorite via a jaw crusher and disk mill to produce a powder finer than 100mesh. The sample was applied to the Wilfley table to obtain a heavy mineral separate. Magnetic separation was carried out using a Frantz isodynamic separator and density separation used methylene iodide to isolate U bearing minerals for analysis. Following separation from the whole rock powder, U bearing minerals, especially zircon, were picked by hand. After separating zircons, those that did not have inherited cores were picked and photographed. The zircons without inheritance were partitioned into populations based on shape, size or clarity and were ready for analysis. Zircons were split into populations to maximize U and Pb count.

Zircons were cleaned in 4N HNO_3 ethanol and acetone before being left for one hour in 4N HNO_3. Zircons were cleansed with water to remove the HNO_3 and acetone to remove the water. After cleaning, each population was weighed and moved from weighing boats into Teflon vials for spiking and dissolution. The zircons were dissolved in a 15:1 mixture of 48% HF and 7N HNO_3 and 2.94mg of a spike solution comprising $^{205}Pb/^{235}U$ was added. The samples were placed in Manel Bombs and positioned in an oven at 215°C for 3 days to dry. Following this the samples were checked for complete dissolution and added to 3.1N HCl before being left in the oven overnight at the same temperature. Following the preparation stage, the zircon solution was added to chromatography columns and clean water was used to extract the U. Then, 6.2N HCl was added to extract the Pb. After this, the sample consists of just U and Pb. Finally the samples were added to more 3.1N HCl and were ready for analysis in the TIMS. The isotopic analysis was performed on a VG354 thermal ionization mass spectrometer operating in single collector Faraday and analogue Daly photomultiplier detector peak-hopping mode. Typical Pb and U isotopic analysis consisted of between 80 and 150 isotopic ratios collected in a temperature range between 1450-1600°C and 1500-1650°C respectively. Analysis under these conditions can achieve internal precision better than 0.05%. Ages were calculated using ISOPLOT software (Ludwig, 1992) and represent discordia line upper and lower intercept ages determined by two-error linear regression treatment of the data. The ages were calculated using the ^{238}U ($1.55125x10^{-10}a^{-1}$) and ^{235}U ($9.8485x10^{-10}a^{-1}$) decay constants and the present day $^{238}U/^{235}U$ ratio of 137.88 determined by Jaffey et al. (1971). The error ellipses and all age uncertainties are reported at two sigma (2σ).

2.6.8 Microthermometry

Thin sections used for fluid inclusion studies are doubly polished, 100-150μm thick wafers. After fluid inclusions are found, and highlighted, the wafer was separated from the glass slide by acetone. Based on the criteria outlined in Roedder (1984), the fluid inclusions in quartz, rhodochrosite and calcite were characterized at room temperature into primary, pseudosecondary and secondary fluid inclusion assemblages (FIA as defined in Goldstein and Reynolds, 1994)) and the phase assemblage were described. Quartz and calcite do not contain any growth zonation, thus large, randomly orientated inclusions were considered to be primary fluid inclusions. Rhodochrosite has obvious growth zones, thus the fluid inclusions were situated in specific growth zones and could be confidently classified as primary. Pseudosecondary fluid inclusions were defined as trends or linear arrangements of inclusions, which terminated within the crystal or primary growth zone. Secondary assemblages were the most common and were defined as later, linear trends of inclusions that crossed primary growth zones or crystal boundaries. The phase assemblages were then described using the following terminology; Lw = liquid water, Vw = water vapor, Sd = daughter mineral, So = opaque mineral. For each FIA, the microthermometric data was collected in the same run. All microthermometric analyses were conducted on a Linkam THMSG600 heating/freezing stage mounted on an Olympus BX50 microscope equipped with a 40x SLCPlan long-working distance fluorite objective lens, 2x image magnifier and a video camera located in Dr. Jeremy Richards lab. The heating stage has a working range from -150°C up to 600°C. At high temperatures a water pump was used to cool the stage. Calibration was performed using synthetic fluid inclusions from Synflinc labs, before and after microthermometry. Calibration was completed using pure CO_2 inclusions (melting point of -56.6°C), and pure water inclusions (melting point 0°C and critical point 374.1°C). Accuracy below 0°C is ±0.2°C and above 0 is ±2°C. Reported salinities have been calculated from the melting point using equations from Bodnar for ice melting (Bodnar, 1992). Salinities are reported in weight percent NaCl equivalent (wt.% NaCl eq.)

2.6.9 X-Ray Diffraction

X Ray Diffraction (XRD) was used to identify unknown clay minerals in the alteration package around the mineralized sections. Diane Caird at the University of Alberta performed the XRD analyses. The equipment used included a Rigaku Geigerflex Powder Diffractometer equipped with a cobalt cathode ray tube, a graphite monochromator and a scintillation detector. Multiple drill core samples were selected from each alteration assemblage and powder was collected using a hand drill. The powder had to be relatively homogenous and very fine so a mortar and pestle was used to grind the powder to as fine a grain size as possible. As all the samples had a simple mineralogy, they were mounted and analyzed on a quartz plate.

2.7 Analytical Results

The results are briefly outlined in a paragenetic sequence (Fig. 2.4) and a table of results organized by analytical technique (Table 2.1)

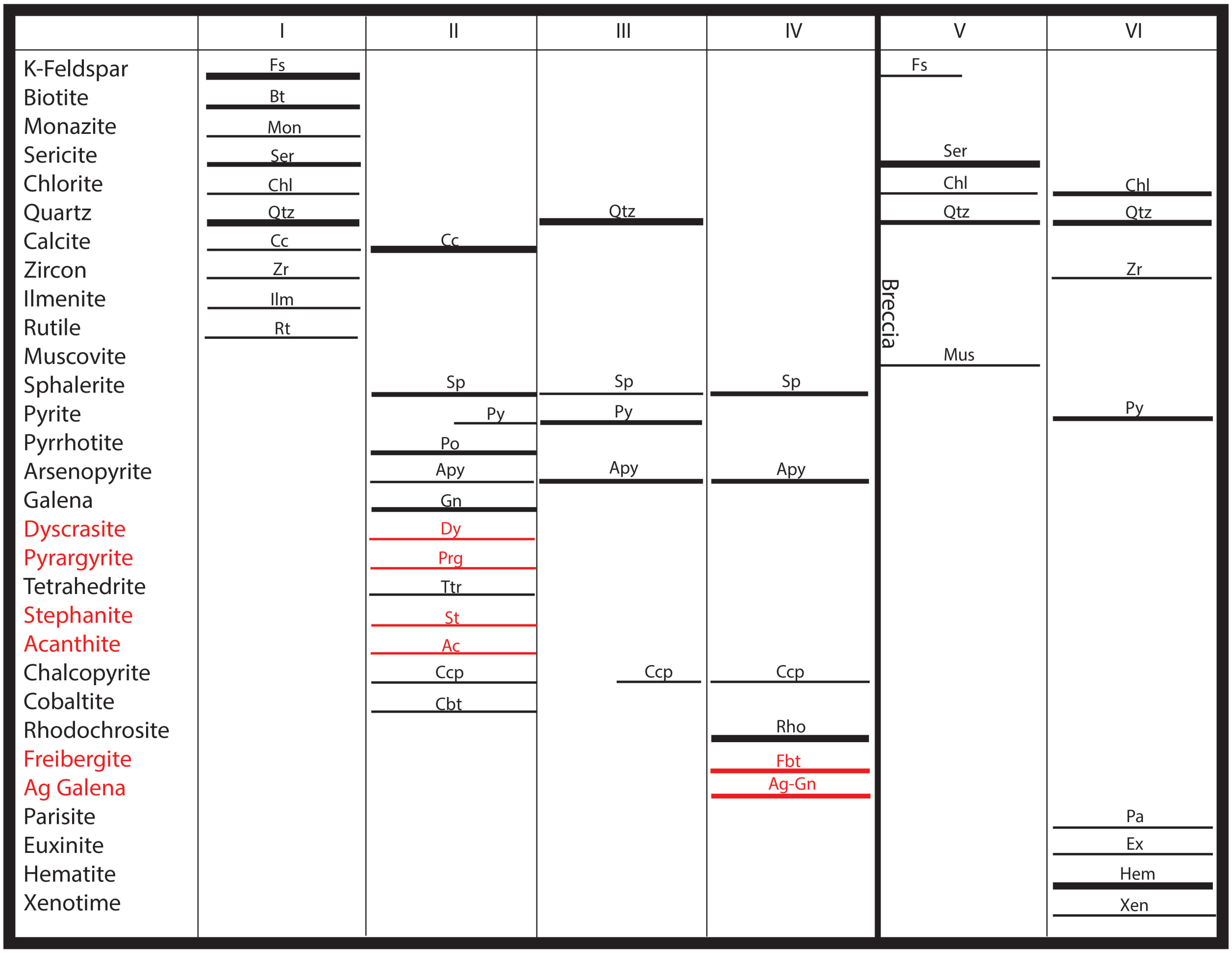

Figure 2.4 Paragenetic sequence of the Hammer Zone. It is a detailed summary of the minerals present in each paragenetic phase. I: Potassic alteration of the Anvil Suite granite, II: Calcite veining phase, III: Quartz veining phase, IV: Rhodochrosite veining phase, V: Alteration associated with phases II to IV, VI: Post Ore oxide phase. Thickness of line represents the prominence of a mineral in a paragenetic phase. Silver bearing minerals are highlighted in red.

Table 2.1 (next page) Table of all the results from the vein mineralization phases (II to IV) sorted by paragenetic phase and analytical technique.

	Calcite		Quartz		Rhodochrosite	
Petrography	*Gangue*	*Sulfides*	*Gangue*	*Sulfides*	*Gangue*	*Sulfides*
	Vein calcite	Dominated by pyrrhotite. Galena and sphalerite secondary minerals. Silver bearing minerals are varied and rare.	Vein quartz	Replacement of sulfides from calcite phase by arsenopyrite and chalcopyrite from this phase. Pyrrhotite has been replaced by pyrite as dominant FeS phase.	Vein rhodochrosite and kutnahorite	Pyrite still dominate over pyrrhotite. Galena and sphalerite are the most dominant sulfides. Silver bearing minerals are less varied but much more common as freibergite and silver bearing galena.
EPMA (WDS)	*Gangue*	*Sulfides*	*Gangue*	*Sulfides*	*Gangue*	*Sulfides*
	As expected, Ca dominates but minor amounts of Mn, Fe and Mg are present at concentrations up to 15wt.%.	Pyrrhotite and galena have uniform chemistries, with no minor elements present. Sphalerite contains Mn and Fe in addition to Zn and S.	N/A	N/A	Two carbonate minerals are present, kutnahorite (CaMn(CO$_3$)$_2$) and rhodochrosite (MnCO$_3$). Of which rhodochrosite is the most common.	EPMA analysis was performed on a number of sulfides (Sp, Gn, Frei, Ccp, Apy) all of which displayed minor element concentrations in addition to the "usual" major elements.
LA-ICP-MS	Carried out on Sp and Po. Sp- above detection: Cu, Ag, Cd, Co, Se, Ga and In. Also: REE. Po- 2 samples: CP32: Co, Ni, Ag, Zn, Cu, Mo, Sb, Bi and REE. CP26: Co, Ni, Ag, Cu, As, Sb, Bi, Ge, Au, Tl, Zn and Cd.		N/A		Carried out upon Sp and Py. Sp- above detection: Cd, Co, Cu, Ga, Se, Ag and In. Py: Co, Ni, Cu, An, Ge, As, Se, Ag, Cd, Sb, Au, Tl and Bi.	
Micro-thermometry	Two phase and single phase inclusions: Th: 215.0-270.0°C Salinity: 8.1-9.9wt.%		Two phase inclusions: Th: 268.1-310.7°C Salinity: 3.6-8.1wt.%		Two phase inclusions: Th: 205.0-290.0°C Salinity: 3.4-13.0wt.%	
Isotopes	Oxygen: -2.0 - 5.0‰ Carbon: -9.0 - 3.0‰ Strontium:0.735 – 0.740		Oxygen: 2.7 – 11.7‰		Oxygen: -4.0 - 9.0‰ Carbon: -8.0 - -6.0‰ Sulfur: 9.0-11.0‰ Strontium: 0.735 – 0.755	

2.7.1 Anvil Batholith

The Anvil Batholith is the host rock for the Hammer Zone mineralization and the first stage of the paragenetic sequence (Fig. 2.4). Overall, the Paragenetic sequence comprises potassic alteration of the host rock Anvil Suite granite (Phase I), vein mineralization phases and associated alteration (Phase II-V) and the post ore oxide phase (Phase VI).

2.7.1.1 Petrography and mineralogy (hand specimen, thin section, EPMA WDS and EDS, BSE and XRD)

Anvil Suite Granite

The Anvil Suite Granite samples have two textural types. The first end member texture (Fig. 2.5A, B) is best described as phaneritic and holocrystalline; the other (Fig. 2.5C) is porphyritic or poikilitic, and holocrystalline with phenocrysts of K-feldspar. Both end members have hypidiomorphic-granular textures and the mineralogy and the proportions of minerals in each of these textural types are estimated to be the same.

The Anvil Suite Granite is altered and the original composition is unknown. The composition of samples collected in the Hammer Zone, is 45% K-Feldspar (K-fs), 20% quartz (qtz), 15% biotite (bt), 15% plagioclase and 5% comprising zircon (zr), monazite (mon), myrmekite (myr) and ilmenite (il). K-feldspar forms poikiloblastic crystals, containing inclusions of plagioclase, quartz and biotite (Fig. 2.5D). K-feldspar displays simple (Carlsbad) twinning, typical of sanidine. Igneous and alteration biotites are present as lath shaped crystals, each with a different preferred orientation in places. Previous studies on the granite have interpreted this as an S-C fabric (Pigage, 2004) (Fig. 2.5E). The quartz crystals in the Anvil Suite Granite have plumose extinction (Fig. 2.5F). Plagioclase crystals are polysynthetically twinned and under crossed nicols have extinction angles of 15°, suggesting they are dominantly albite (Michel-Levy method). Zircon forms euhedral crystals and is randomly distributed in the samples. Ilmenite and rutile are spatially associated, with the ilmenite forming late on the rims of rutile crystals (Fig. 2.5G). Myrmekite forms on the rims of K-feldspar crystals as both wartlike and rim types (Philips, 1974) (Fig. 2.5F).

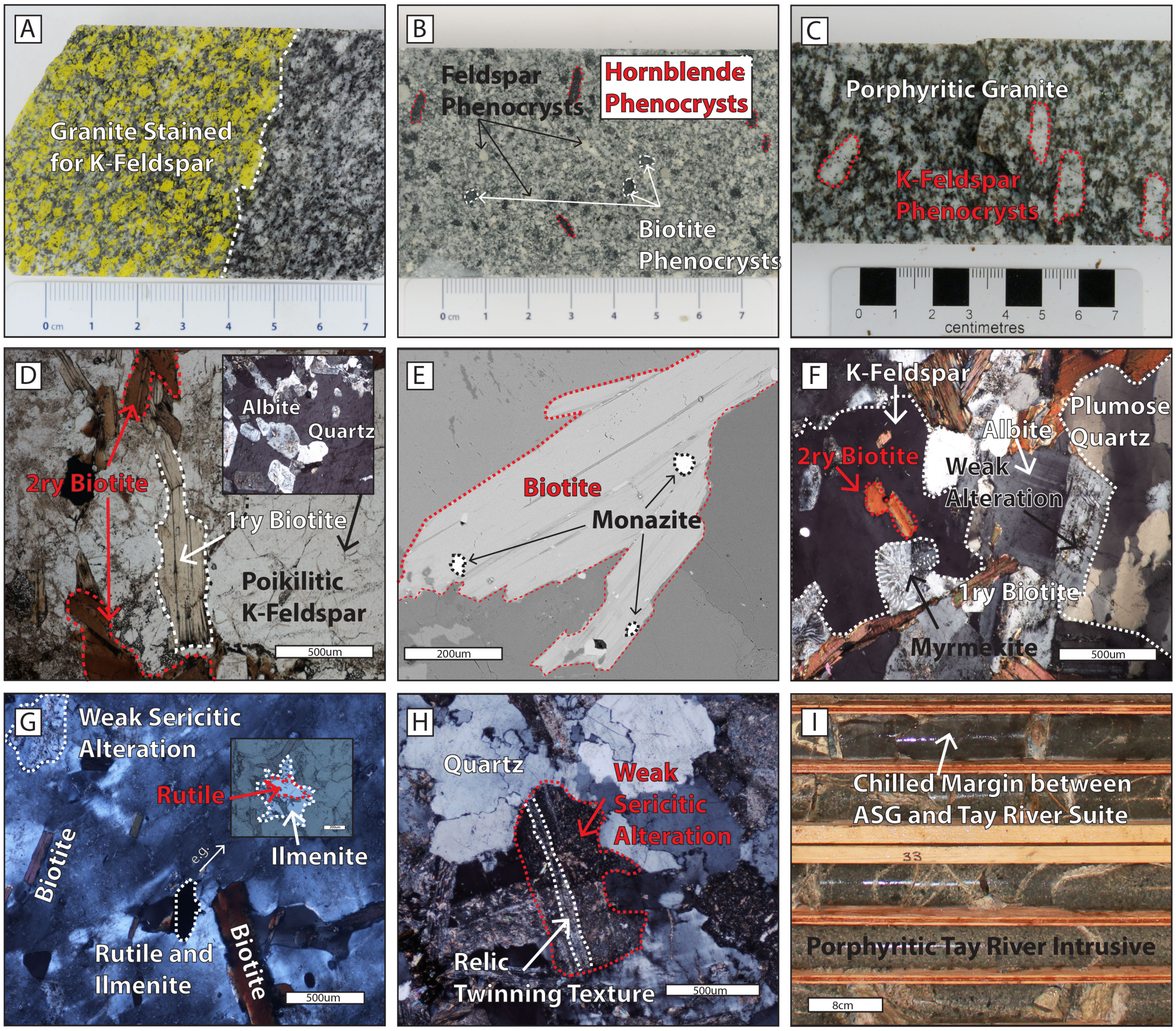

Figure 2.5 Various features associated with the Anvil Batholith. (A) Equigranular Anvil Suite Granite showing high proportion of K feldspar. (B) Porphyritic Tay River intrusive with phenocrysts of feldspar, hornblende and biotite. (C) Porphyritic Anvil Suite Granite with large potassium feldspar phenocrysts. (D) Photomicrograph of primary (pleochroic) and secondary (non-pleochroic) biotite alongside poikiloblastic K feldspar. (E) Back Scattered Electron (BSE) image of biotite and monazite. (F) Photomicrograph of biotite and K feldspar with weakly altered albite, plumose quartz and myrmekite (G) Large potassium feldspar phenocryst with biotite, sericite and rutile chadacrysts. Rutile shows alteration to ilmenite. (H) Photomicrograph of albite with weak sericitic alteration with relict twinning textures still present. (I) Chilled margin between Anvil Suite Granite (ASG) and Tay River intrusive.

Potassic Alteration of Anvil Suite Granite ***(Phase I)***

The Anvil Suite granite samples contain more K-feldspar than would be typical for an igneous rock; staining the potassium feldspars with Na-cobaltinitrate highlighted this (Fig. 2.5A). The plagioclase feldspars are weakly altered to sericite with twinning and relict textures still present (Fig. 2.5H). There are two forms of biotite present; igneous (from the unaltered Anvil Suite granite) and alteration or secondary. Alteration related biotites do not form lath-shaped crystals with one strong cleavage indicative of igneous biotites (Deer et al., 1963); instead they appear as rhomb shaped biotites, lacking any strong cleavage (Fig. 2.5D, F) and are interpreted to be secondary. The secondary biotites do not display pleochroism, in contrast to the igneous biotites. Monazite occurs as euhedral to subhedral crystals and is spatially associated with igneous and secondary biotites (Fig. 2.5D). These factors suggest it is likely the Anvil Suite Granite has undergone potassic alteration; the source of this alteration is unknown.

Tay River Suite Intrusions

Intruding the Anvil Suite granite at both a regional and local scale is a porphyritic, hypidiomorphic granular rock of intermediate composition (Fig. 2.5B). The petrographic description of a rock with porphyritic texture, comprising an aphanitic groundmass and phenocrysts of plagioclase feldspar, biotite and, rarely, hornblende matches previous descriptions of the Tay River intrusive suite (Mortensen et al., 2000; Pigage, 2004). The Tay River Dykes are bordered by a chilled margin that varies from 1cm to 1m (Fig. 2.5I).

2.7.1.2 Whole Rock Geochemistry

Major, minor and trace element analysis (Fig. 2.6.1; Fig. 2.6.2; Fig. 2.7; Appendix 3) were carried out on eight samples of the Anvil Suite Granite, all the samples have some degree of potassic alteration.

The Anvil Suite Granite samples returned SiO_2 values between 67 and 71wt.% (Fig 2.6.2A). Using the ilmenite/magnetite diagram designed by Ishihara (2000) the samples analyzed plot in the ilmenite field (Fig 2.6.2A). On a plot of Al_2O_3/Na_2O*K_2O vs $Al_2O_3/Ca_2O*Na_2O*K_2O$ the granite plots in the peraluminous, S-type granite field according to Shand's classification scheme (1943) (Fig. 2.6.2B). A major element plot of Na_2O+K_2O vs SiO_2 was used to classify the granite as subalkaline vs alkaline (Fig. 2.6.2C). Similar elements are used in a FeOt (total iron oxide) vs Na_2O+K_2O vs MgO ternary plot to classify the granite as calc-alkaline vs tholeiitic (Fig 2.6.1).

Minor and trace element plots can be used to investigate the formation settings of the igneous rock. Many discriminant plots have the Anvil Suite Granite plotting in the arc formational environment; Rb vs Nb + Y (Fig. 2.6.2D), Ta vs Yb (Fig. 2.6.2E) and Nb vs Y plots (Fig. 2.6.2F)(Pearce et al., 1984). Trace element plots can also be used to elucidate information about the conditions of formation. Sm/Yb, and La/Sm ratios are both above 5 (Fig 2.7A) (Kay et al., 1991, Kay and Mpodozis, 2001). The La/Yb ratios plot above 30 (Fig. 2.7B) (Kay et al., 1991). All of these trace element ratios suggest the Anvil Batholith formed from source rocks that had resided deep in the crust. Spider plots of trace element data show positive Pb and negative Ti anomalies, and negative Eu (Fig. 2.7C-D). The possible effect of the alteration on these plots will be discussed below.

Figure 2.6.1 Ternary plot of FeOT (total) vs Na_2O+K_2O vs MgO showing the analyses of the Anvil Suite Granite plotting in the Calc-Alkaline field

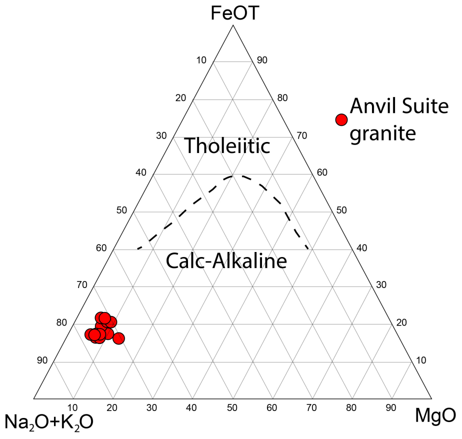

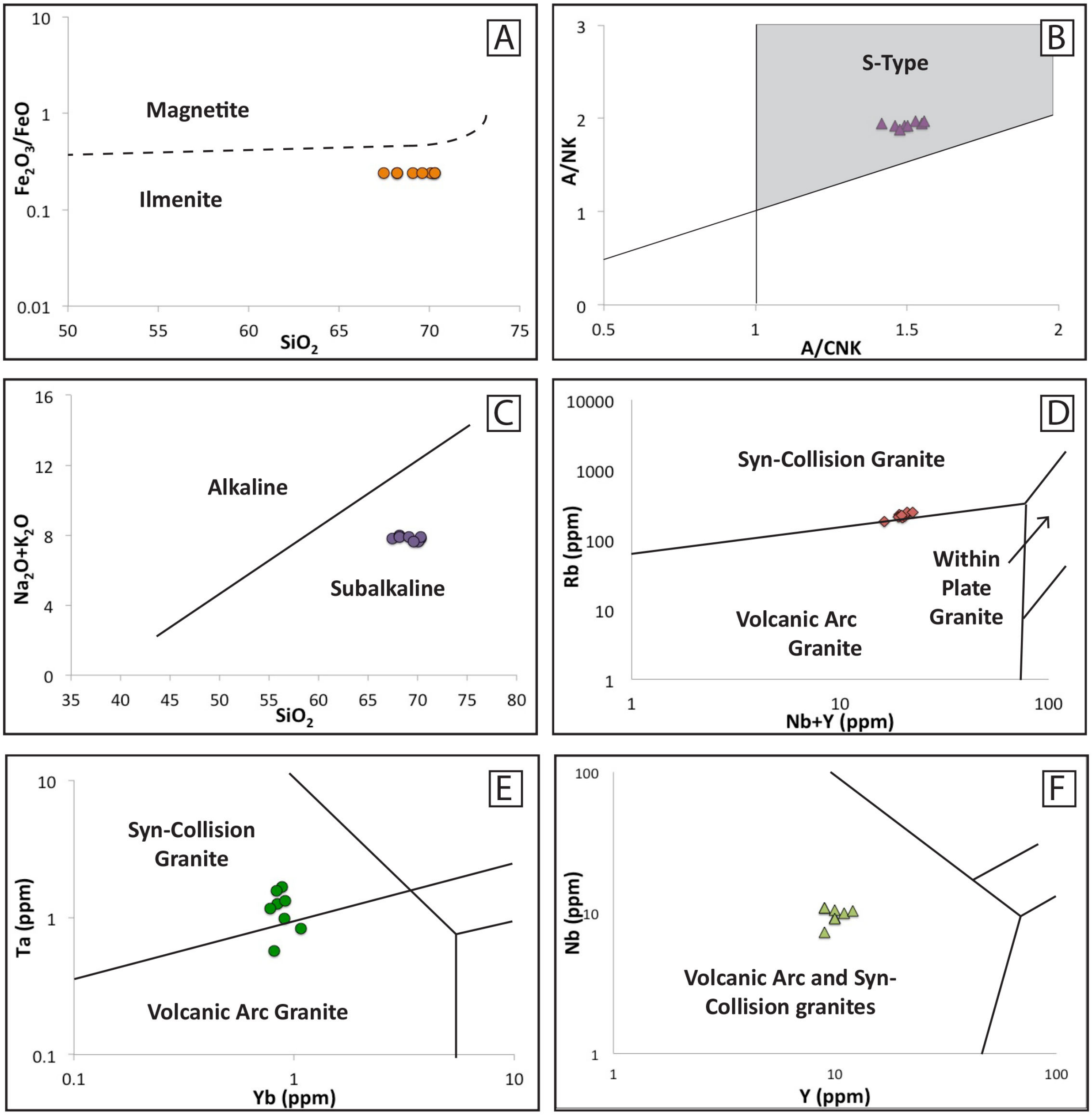

Figure 2.6.2 Graphs plotted of whole rock data from potassically altered Anvil Suite Granite samples. (A) Magnetite vs. Ilmenite series granitoid compositions based on Fe_2O_3/FeO vs SiO_2 (Ishihara et al., 2000). (B) Al_2O_3/Na_2O*K_2O (A/NK) vs $Al_2O_3/Ca_2O*Na_2O*K_2O$ (A/CNK) plot used for classification of granite into A-type, S-type or I-type (Shand, 1943). (C) Major element plot of Na_2O+K_2O vs SiO_2 used to discriminate between subalkaline and alkaline igneous rocks *(D-F) Trace element plots of (D) Rb vs Nb+Y, (E) Ta vs Yb and (F) Nb vs Y.*

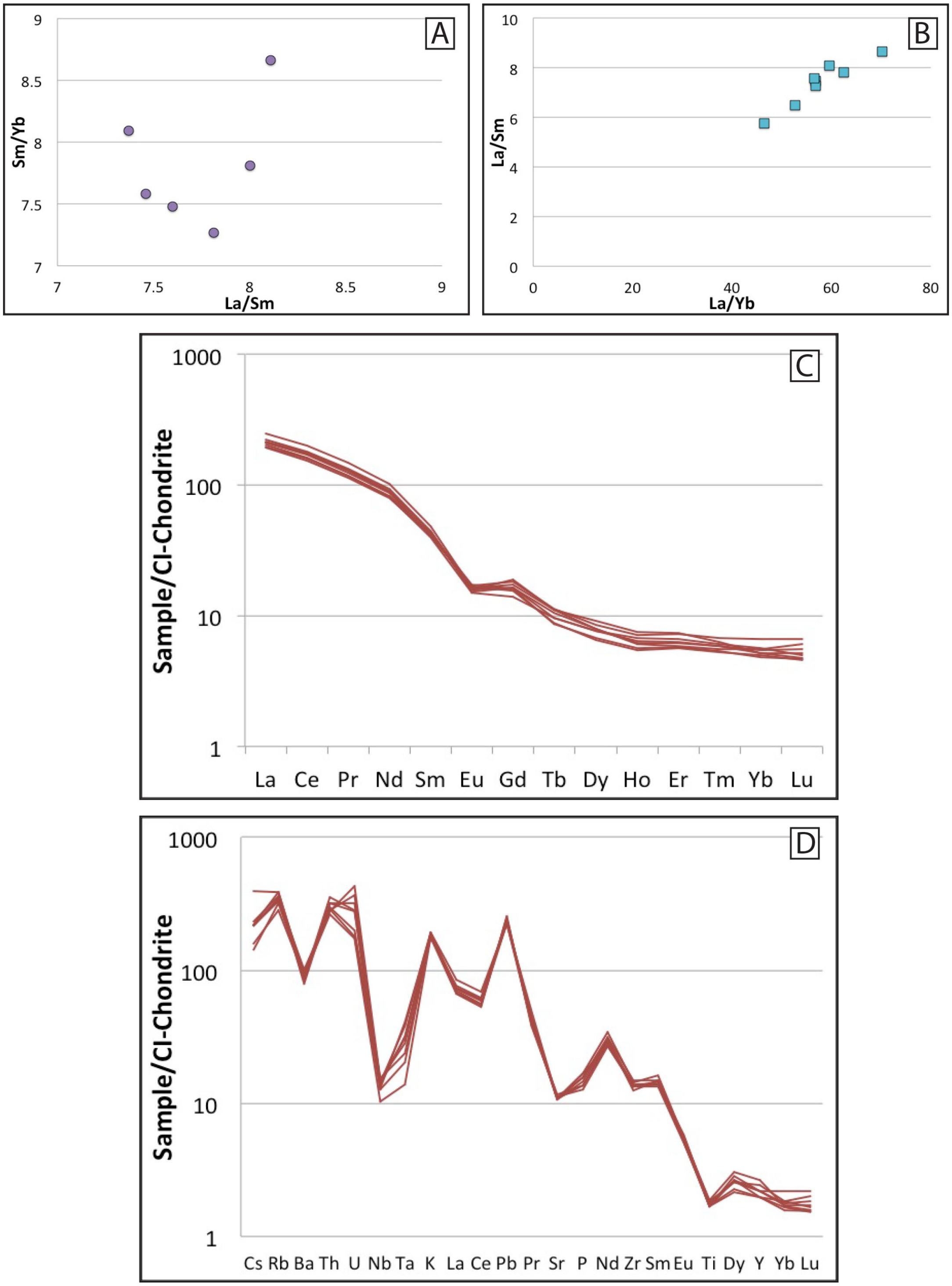

Figure 2.7 Plots of whole rock data from Anvil Suite Granite samples. (A) Trace element plot of Sm/Yb vs. La/Sm and (B) La/Sm vs La/Yb. (C) Multi-element diagram of rare earth elements normalized to chondrite values from Sun and McDonough. (D) Mulitelement diagram of elements, normalized to chondrite values according to Sun and McDonough, (1995).

2.1.7.3 U-Pb dating

U –Pb dating was performed via two methods. LA-ICP-MS dating was performed *in situ* on monazites associated with the secondary biotites. TIMS dating was carried out on zircon separates from the Anvil Suite Granite. All the data can be found in Appendix 6.

TIMS dating of zircon

Ten mineral separates of zircon were collected from crushed whole rock samples of equigranular Anvil Suite Granite (Fig. 2.8A) for analysis on the TIMS. Large, clear, euhedral zircons were targeted, cleaned and analyzed by TIMS as outlined in section 2.4. Each of the three populations collected returned good analytical results, however the ages were not concordant. Figure 2.8 displays the analyses; discordance resulted in the very large errors on the ages returned, likely due to large inherited cores. As a result these data cannot be used to date the host rock.

U-Pb Monazite via LA-ICP-MS

Twenty-seven monazite crystals associated with the potassic alteration were identified via BSE imaging and EDS analysis by EPMA. The majority of monazites found were small, ranging from 20 to 50µm in diameter (Fig. 2.9A, B). Analyses were carried out on larger crystals using one or two 20µm spots on each monazite. The majority of monazites analyzed returned robust data with a total of thirty-five points returning ages. Six points were disregarded due to an extremely high discordance of over 95% (Appendix 6) on the Tera-Wasserberg plot (discordant values plot above the Concordia) which was attributed to being the result of excess common Pb.

A second type of discordance causes data to plot below the Concordia and is the result of excess ^{206}Pb (Scharer, 1984). Hydrothermal monazite can contain elevated levels of ^{206}Pb due to elevated levels of ^{230}Th, and, although a correction for ^{206}Pb is hypothetically possible, the exact composition of the formational fluids must be known (Parrish, 1990). Since the nature of the fluids that altered the granite was not known different initial ^{230}Th values for monazite values were used via a trial and error method to try and reduce discordance. However, this approach resulted in more extreme discordance, therefore, a correction factor was not applied to the data for excess ^{206}Pb.

Discarding the discordant data for ^{204}Pb and using Isoplot (Ludwig, 2003) the monazite crystallization age was interpreted to be **106.6±1.0Ma** (Fig. 2.9C).

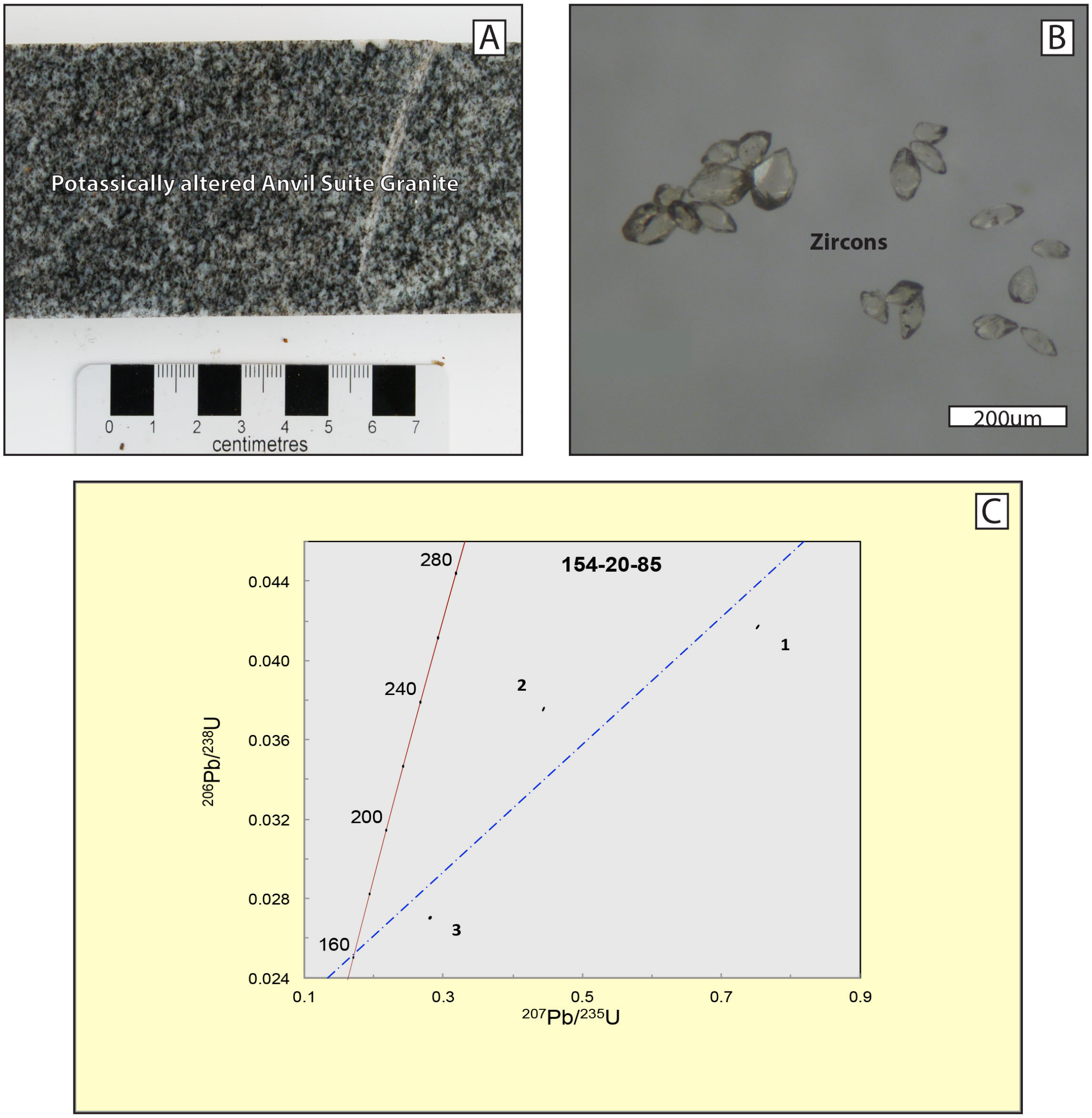

Figure 2.8 (A) Photograph of the rock sample used for TIMS analysis, note lack of alteration. (B) Photograph of sample zircons used for dating. (C) Highly discordant data from the three populations of zircons dated.

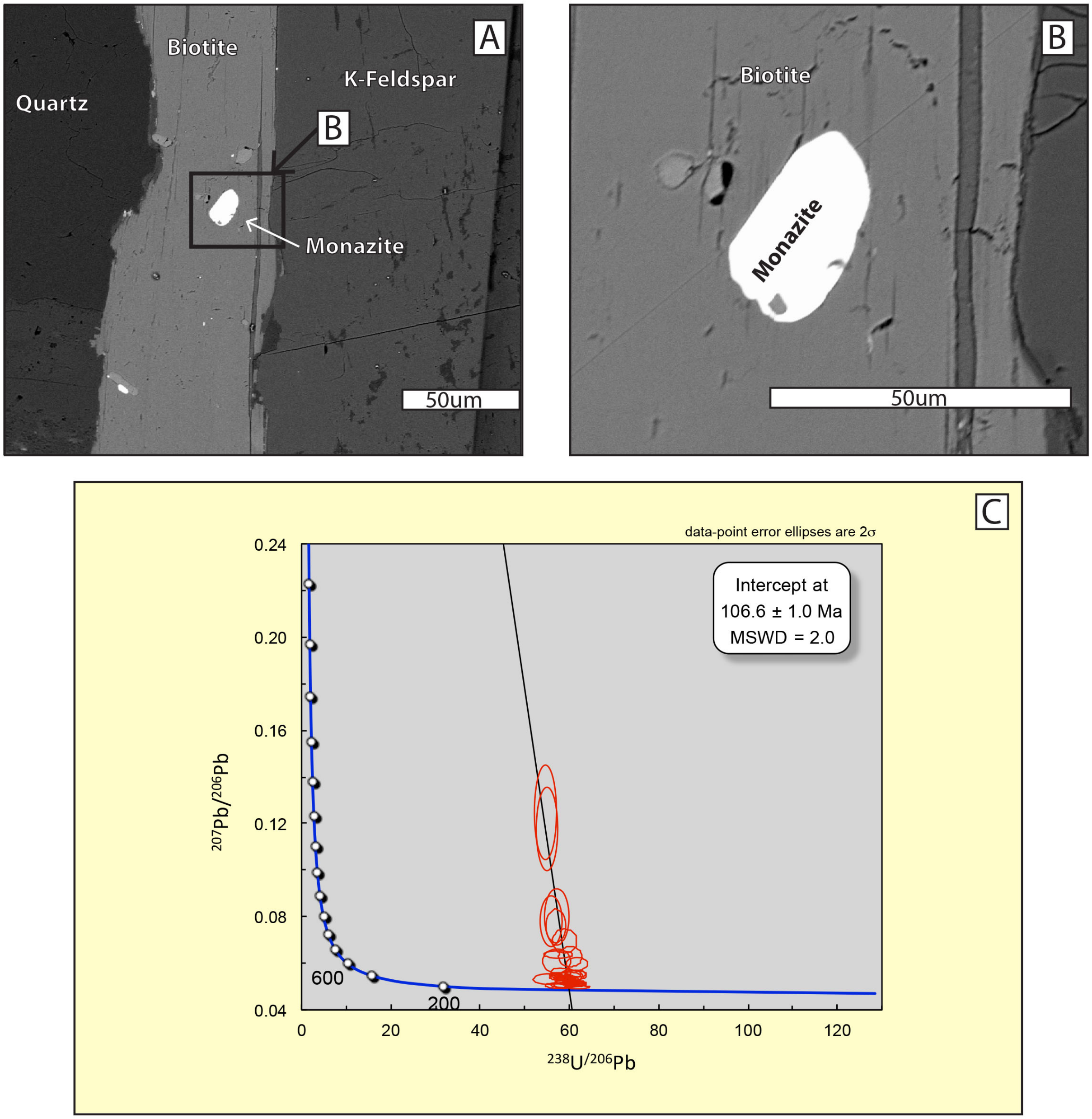

Figure 2.9 Typical monazite grain in secondary biotite and results of monazite analysis (A, B). (C) Terra-Wasserberg plot, with calculated age of ***106.6±1.0Ma****.*

2.7.2 Vein mineralization (Phase II-V)

The vein mineralization comprises three generations of sulfide bearing veins and one generation of alteration. Each vein mineralization phase has a different gangue mineral composition: calcite and rhodochrosite veins host the majority of sulfide mineralization, with quartz veins containing minor, non silver bearing sulfides.

2.7.2.1 Calcite Veins (Phase II)

2.7.2.1.1 Petrography and mineralogy (hand specimen, thin section, EPMA and XRD)

Phase II, calcite veins are the earliest veins in the Hammer Zone. The veins occur as solitary, planar, 0.2-1cm wide carbonate veins (Fig. 2.10A, B). They contain massive, anhedral, high relief calcite crystals with sweeping extinction (Fig. 2.10C). Bordering many of the calcite veins is an iron rich carbonate, which is interpreted to have formed during the final paragenetic phase (VI) and will be discussed in section 2.7.2.6 (Fig. 2.10B, I).

The most common sulfides present in the calcite veins are pyrrhotite (Po), galena (Gn) and sphalerite (Sp) (Fig. 2.10D). These occur as euhedral to subhedral grains forming in spaces between, or on grain boundaries, of the calcite crystals. Commonly, Po, Gn and Sp have a mottled texture, with quartz (from a later veining event, Phase III) partially replacing the sulfides (Fig. 2.10D, E). The ruby red sphalerite of Phase II is lighter in color compared to other paragenetic generations of sphalerite.

Also present are minor to trace amounts of other sulfides. These can be divided into two groups; non-Ag-bearing minerals; arsenopyrite, chalcopyrite, tetrahedrite, cobaltite and Ag-bearing minerals; dyscrasite, acanthite, pyrargyrite and stephanite (Fig. 2.10F, G; Fig. 2.11). All of these minerals occur proximal to pyrrhotite (Fig. 2.10F; Figure 2.11). Veins and minerals associated with later ore stages, quartz and rhodochrosite, as well as the post ore oxide phase, cross cut or overgrow the calcite veins (Fig. 2.10H, I).

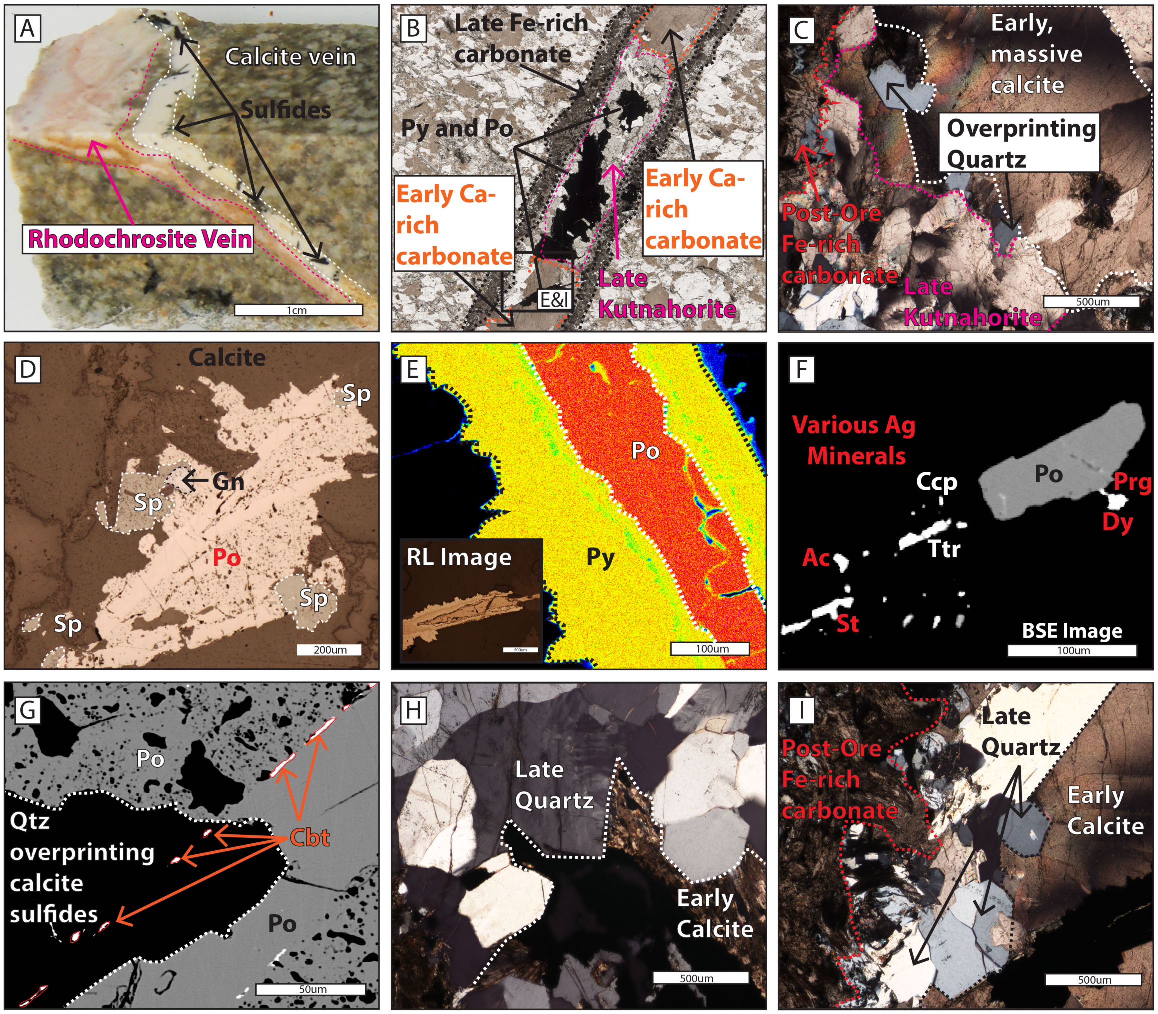

Figure 2.10 (A) Photograph of sulfide bearing calcite vein alongside rhodochrosite vein in altered host Anvil Suite Granite. (B) Portion of a thin section scan showing three generations of iron carbonate and sulfides. (C) Photomicrograph of massive calcite overprinted by quartz, in turn overprinted by rhodochrosite. (D) Reflected light photomicrograph of galena, sphalerite and pyrrhotite hosted by the calcite. (E) Elemental map (Fe) of the relationship between late, rhodochrosite stage pyrite and pyrrhotite. (F) BSE image of the minor sulfides associated with the calcite veins, alongside a pyrrhotite grain. All abbreviations are described in the paragenetic sequence (G) Small cobaltite inclusions in pyrrhotite and quartz. (H) Late, vein quartz overprinting early calcite. (I) Post ore oxide phase, Fe-rich carbonate overprinting both quartz and calcite.

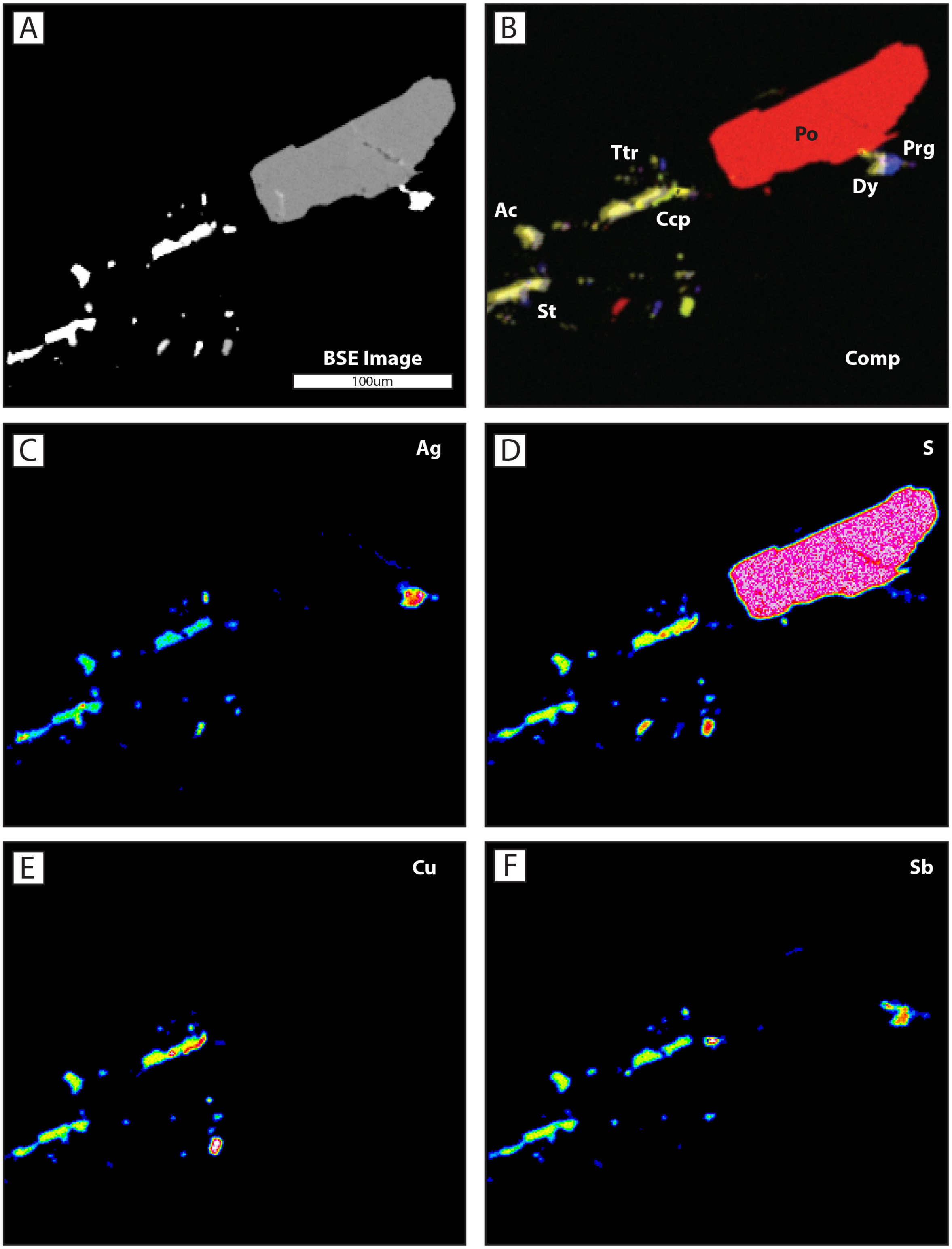

Figure 2.11 Plate showing (A) a BSE image, and (B) a composite elemental map made of maps for four different elements (C) Ag, (D) S, (E) Cu and (F) Sb. Minerals present; acanthite (Ac), stephanite (St), tetrahedrite (Ttr), chalcopyrite (Ccp), dyscrasite (Dy), pyragyrite (Prg) and pyrrhotite (Po), are labeled in (B).

2.7.2.1.2 EPMA Analysis (WDS and elemental mapping)

All EPMA data can be found in Appendix 1 and are discussed below.

Sulfides

The sole iron sulfide in the calcite phase is pyrrhotite, which has Fe concentrations between 42.0 and 43.0 weight percent (wt.%), and S concentrations between 52.0 and 53.0wt.% (Appendix 1; Fig. 2.12A; Fig. 2.13A) The pyrrhotite contains no other major elements. In some instances, this pyrrhotite has been overgrown by pyrite from later vein phases (Fig. 2.12).

Analyses of sphalerite returned values for Zn (54.0-58.0 wt.%), S (32.0-34.0 wt.%), Fe (8.0-11.5 wt.%) and Mn (0.2 to 0.6 wt.%) (Fig. 2.13B-D). Galena had an end-member composition with Pb and S concentrations that range from 85.0 to 86.3 wt.% and 12.6 to 13.8 wt.% respectively (Fig. 2.14A-C).

Carbonate

The calcite contains minor amounts of Mn, Fe and Mg and 40.0 wt.% Ca in the darker brown, massive, anhedral crystals (Fig. 2.15). The other major elements (Mn, Fe and Mg) have concentrations below 15 wt.%.

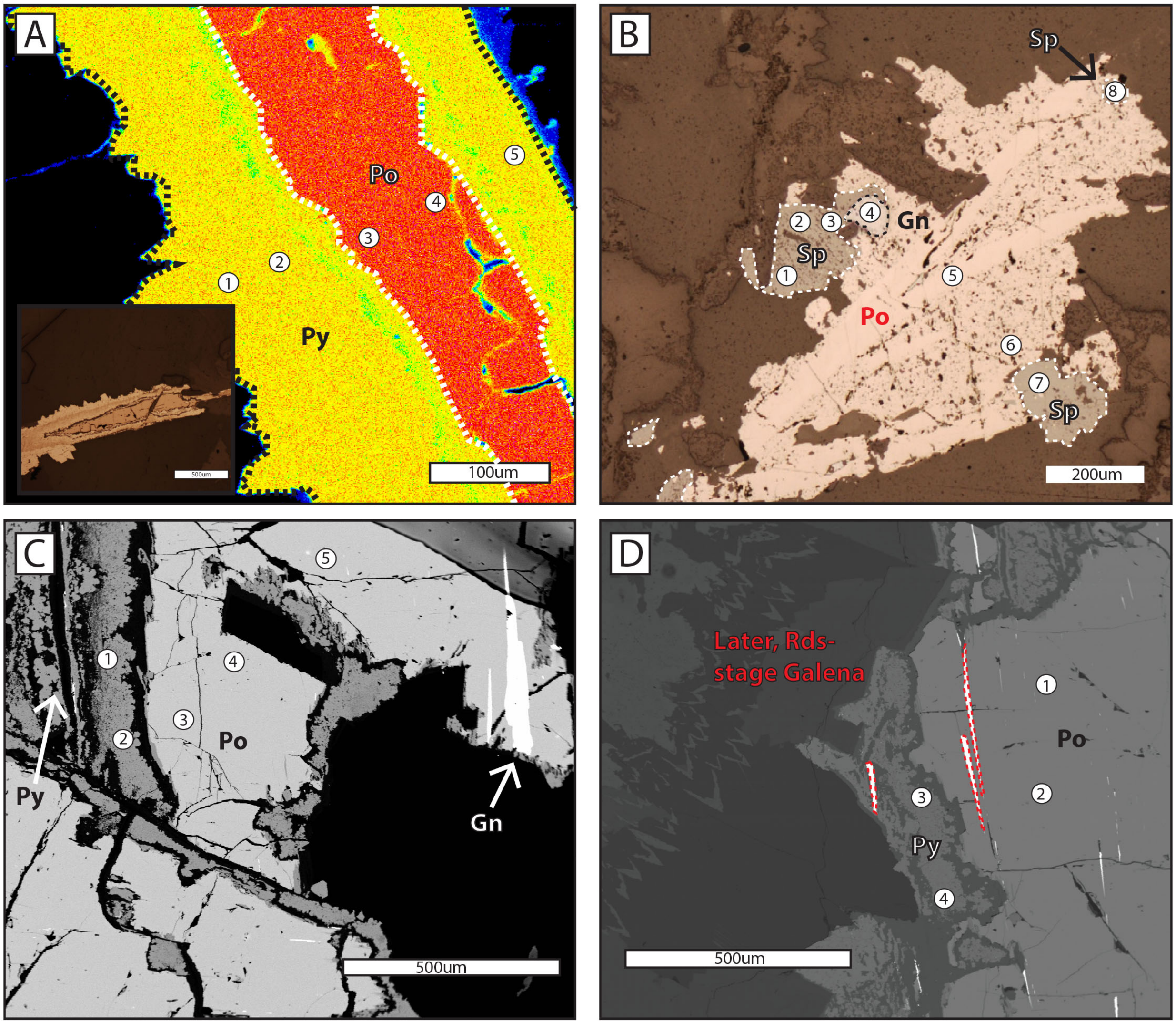

Figure 2.12 EPMA quantitative (WDS) analysis points for sulfides from the calcite and rhodochrosite phases. (A) BSE image of a transect across early pyrrhotite and later pyrite (B) Reflected light microphotograph of points from sphalerite, galena and pyrrhotite in calcite veins. (C) BSE image of points taken from pyrite from rhodochrosite phase and pyrrhotite from calcite phase. (D) BSE image of points in pyrrhotite and pyrite. Data for all points is given in Table 2.1.

Element	***Pb (wt.%)***	***S (wt.%)***	***Fe (wt.%)***	***Sb (wt.%)***	***Zn (wt.%)***	***Cu (wt.%)***	***Mn (wt.%)***	***Total (wt.%)***
A								
1	~	*52.73*	*45.62*	~	~	*0.08*	~	*98.53*
2	~	*52.93*	*45.29*	~	~	*0.07*	~	*98.51*
3	~	*39.78*	*60.21*	~	~	~	~	*100.21*
4	~	*40.24*	*60.03*	~	~	~	~	*100.51*
5	~	*52.75*	*45.67*	~	~	*0.09*	~	*98.64*
B								
1	~	*33.45*	*10.30*	~	*54.50*	*0.16*	*0.26*	*98.87*
2	~	*33.50*	*9.64*	~	*55.23*	~	*0.31*	*98.96*
3	~	*32.92*	*8.24*	~	*57.36*	~	*0.16*	*98.93*
4	*86.17*	*13.06*	~	*0.16*	~	~	~	*99.63*
5	~	*38.37*	*60.16*	~	~	~	~	*98.78*
6	~	*33.46*	*60.15*	~	~	~	~	*99.27*
7	~	*33.56*	*11.33*	~	*54.19*	~	*0.34*	*99.66*
8	*85.15*	*13.20*	~	*0.16*	~	~	~	*98.70*
C								
1	~	*52.82*	*45.72*	~	~	*0.11*	~	*98.76*
2	~	*52.85*	*45.64*	~	~	*0.08*	~	*98.70*
3	~	*40.53*	*60.16*	~	~	~	~	*100.91*
4	~	*39.93*	*60.11*	~	~	~	~	*100.41*
5	~	*40.15*	*60.15*	~	~	~	~	*100.59*
D								
1	~	*39.54*	*60.33*	~	~	~	~	*100.08*
2	~	*40.06*	*60.11*	~	~	~	~	*100.23*
3	~	*52.84*	*45.66*	~	~	*0.07*	~	*98.68*
4	~	*52.40*	*46.56*	~	~	*0.02*	~	*99.36*

Table 2.2 shows data for Figure 2.12. Capital letters refer to image in plate, number in left column refers to analysis point. "~" symbol indicates data below detection limits, which are given in Appendix 1.

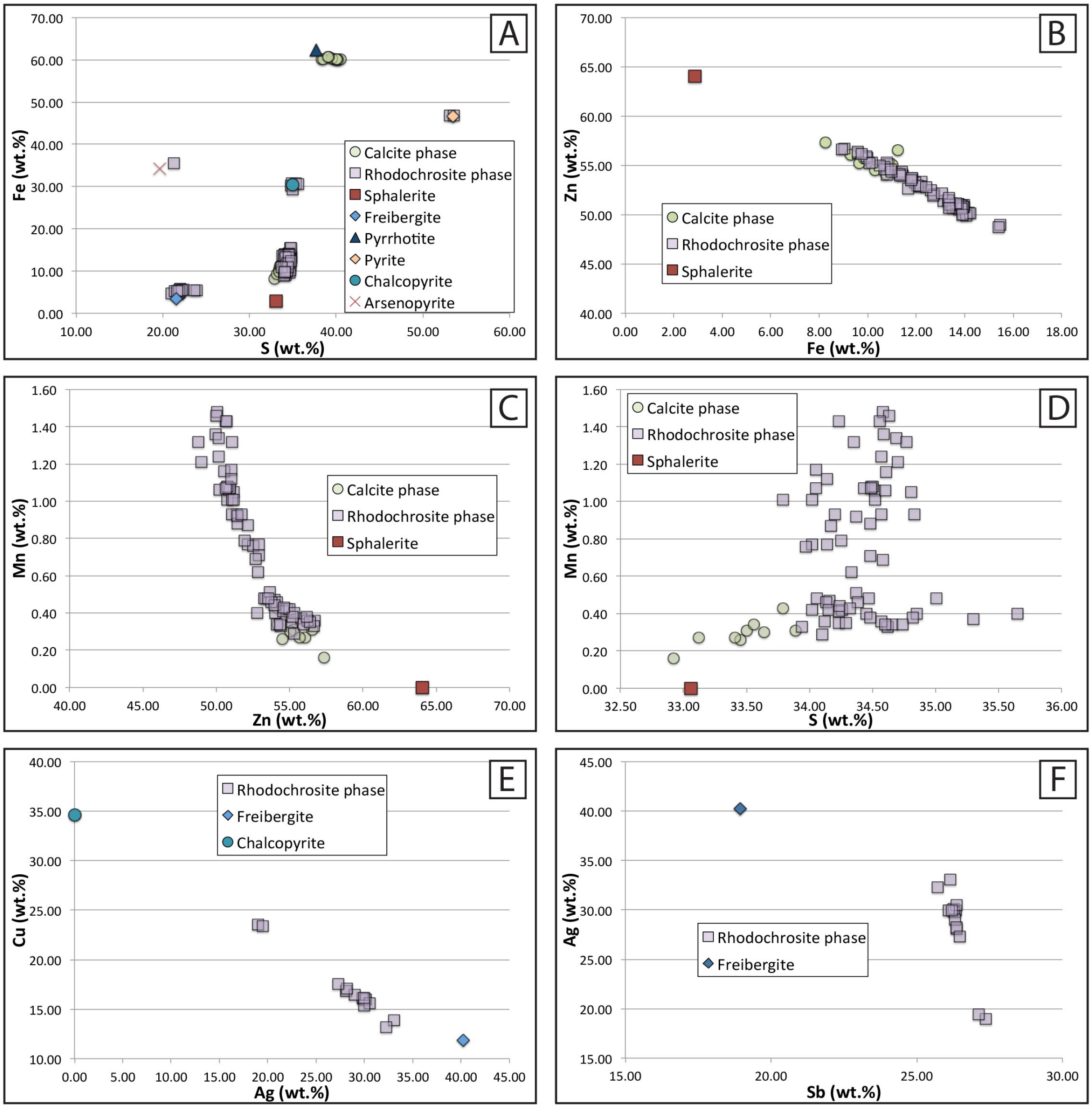

Figure 2.13 (A) Fe vs S concentrations in pyrrhotite and sphalerite from the calcite phase and pyrite, sphalerite, arsenopyrite, chalcopyrite and freibergite from the rhodochrosite phase. (B) Zn vs Fe of sphalerite in both the calcite and rhodochrosite phases, (C) Mn vs Zn of sphalerite in both the calcite and rhodochrosite phases, (D) Mn vs S of sphalerite in both the calcite and rhodochrosite phases, (E) Cu vs Ag from freibergite in the rhodochrosite phase and (F) Ag vs Sb from freibergite in the rhodochrosite phase.

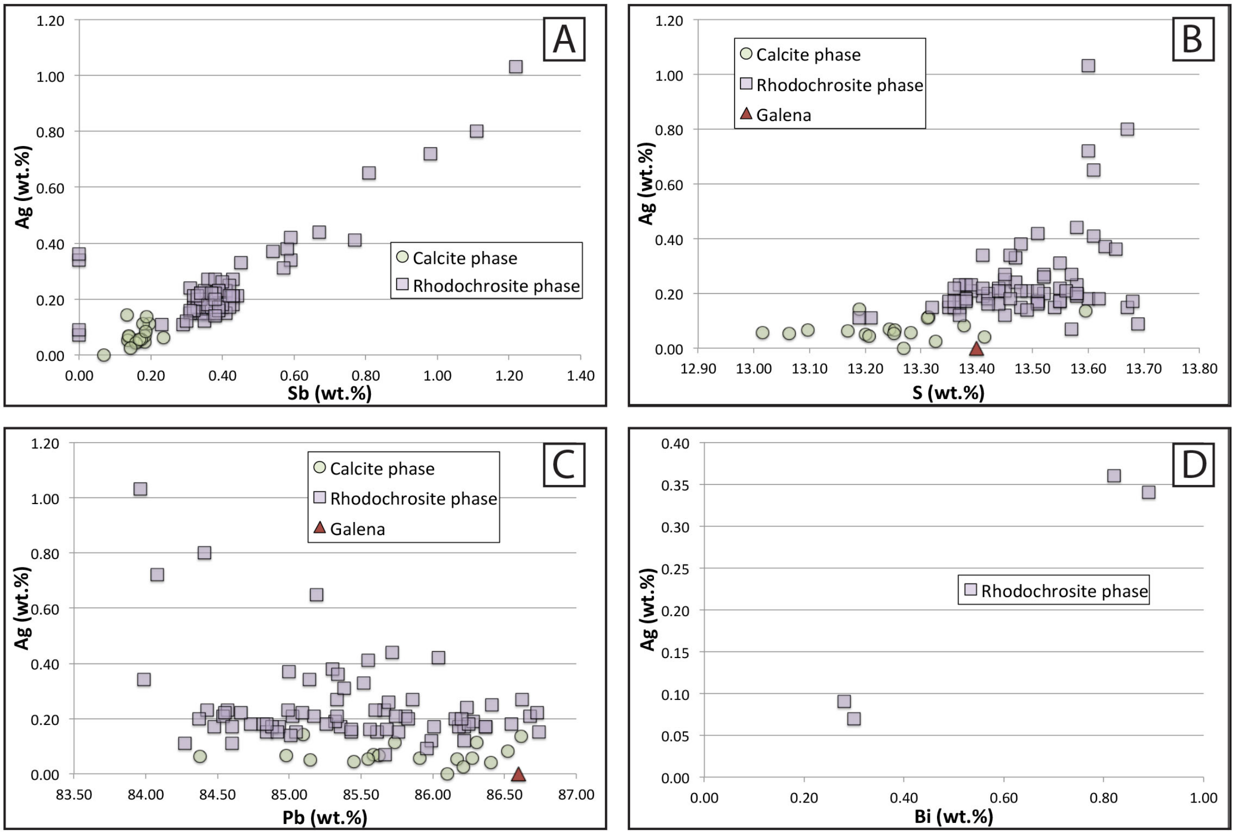

Figure 2.14 Four X-Y plots of elemental data collected from galena from the calcite and rhodochrosite phases, (D) only contains data from the rhodochrosite phase. (A) Ag vs Sb, (B) Ag vs S, (C) Ag vs Pb and (D) Ag vs Bi. Red triangle shows theoretical end member galena.

Figure 2.15 (next page) Plate showing transects of EPMA WDS analysis across calcite veins. Numbers on transect lines correspond to numbers the graphs in each image. (A) 12 point transect from Fe carbonate through calcite back to Fe carbonate. (B) 16 point transect from Fe carbonate through calcite back to Fe carbonate. (C) 12 point transect through a calcite vein (D) 12 point transect through a calcite vein, showing slight composition change at point 7.

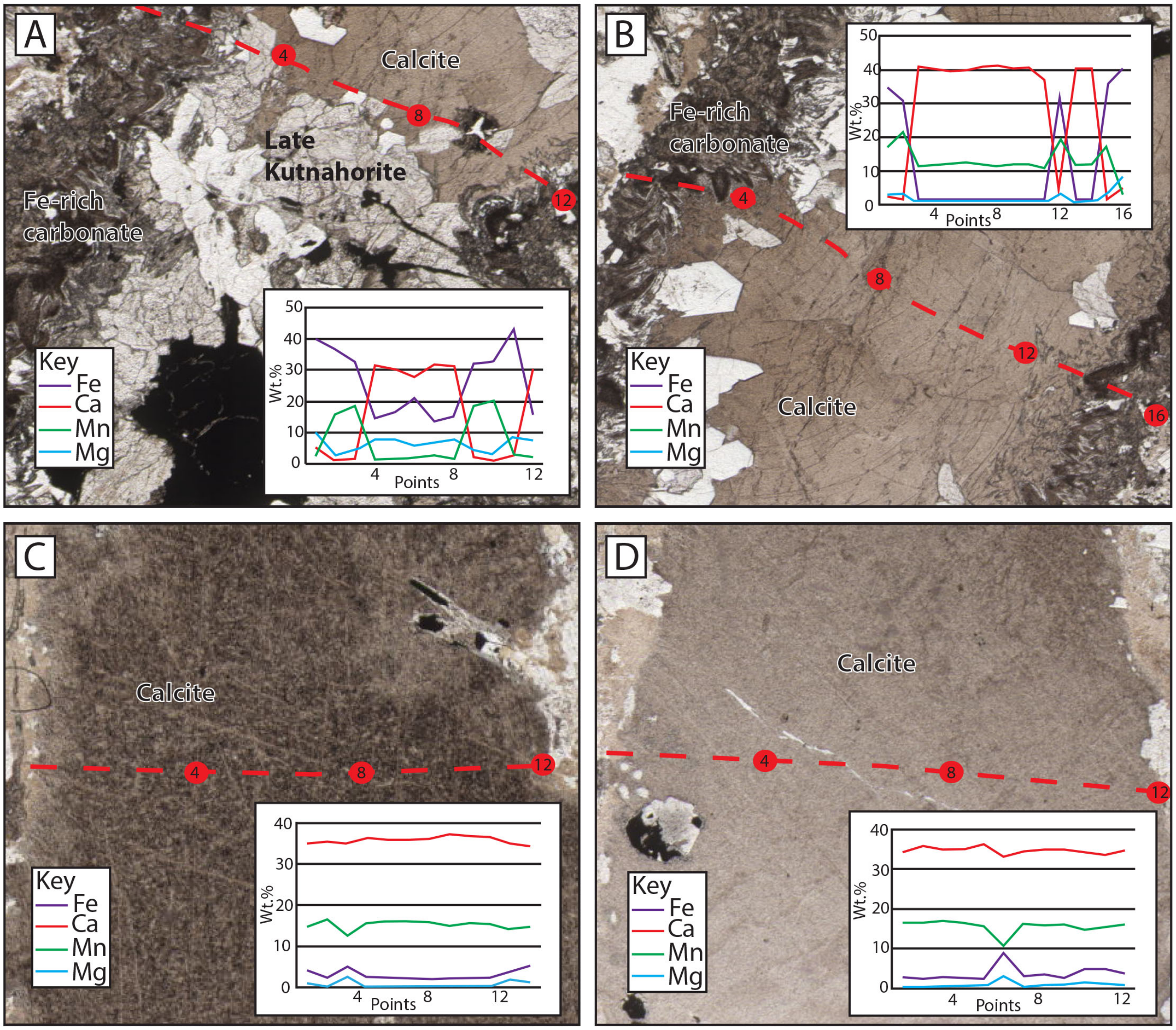

2.7.2.1.3 LA-ICP-MS analyses

LA-ICP-MS analyses were carried out on sphalerite and pyrrhotite in sample CP32 collected from hole HAM 12-17 at a depth of 273.06m and CP26 from hole HAM 12-17 at a depth of 137.92m. These samples were chosen due to the range of sulfides present, meaning multiple analyses could be performed on one thin section. All data collected during these analyses can be found in Appendix 4.

Sphalerite

Sphalerite was analyzed for minor and trace element data from six spots in thin section CP32 (Fig. 2.16A). Analysis of sphalerite returned values above detection for Cu, Ag, Cd, Co, Se, Ga and In (Appendix 4; Fig. 2.16B-D). In addition to the minor and trace elements, sphalerite also returned values for REE above detection (Fig. 2.17A). When normalized to chondrite composition (Sun and McDonough, 1989), the REE have a steeply dipping trend from LREE to HREE with a positive Eu anomaly (Fig. 2.17).

Pyrrhotite

Pyrrhotite from the calcite veins was analyzed for trace and minor element abundances from 12 spots in two thin sections, CP26 and CP32 (Fig. 2.18A, B). Despite belonging to the same paragenetic phase, the abundances of elements vary between these thin sections. The points analyzed from pyrrhotite in CP32 returned above detection concentrations of Co, Ni, Ag, Zn, Cu, Mo, Sb and Bi (Appendix 4). In comparison, analyses of elements from CP26 returned concentrations above detection for Co, Ni, Ag, Cu, As, Sb, Bi, Ge, Au, Tl, Zn and Cd (Fig. 2.18C-F; Appendix 4). Analyses of pyrrhotite from CP32 returned values above detection for REEs. Like the sphalerite, when normalized to chondrite compositions (Sun and McDonough, 1989), the REE have a steeply dipping trend from LREE to HREE with a positive Eu anomaly (Fig. 2.17B).

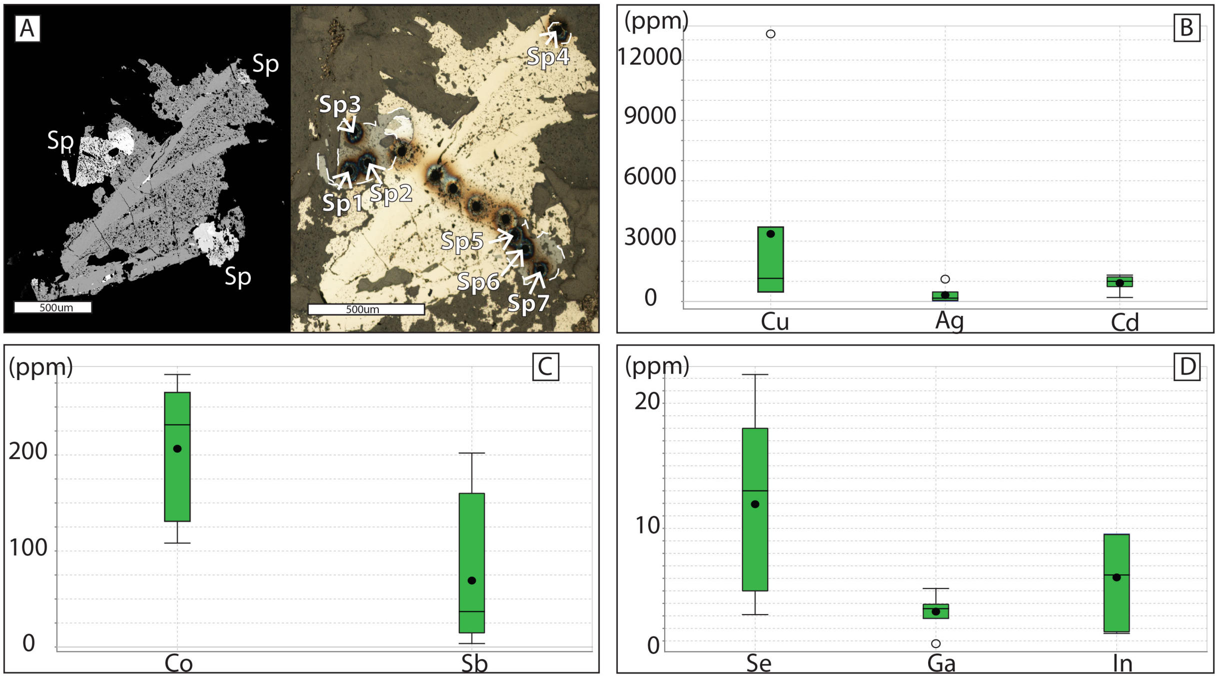

Figure 2.16 Plate showing LA-ICP-MS points from sphalerite (A) and the data collected as box and whisker plots. (B) Cu, Ag and Cd, (C) Co and Sb, (D) Se, Ga and In.

Figure 2.17 (next page) Two multi-element, REE plots for sphalerite and pyrrhotite from the calcite veins. (A) sphalerite and (B) pyrrhotite. Both sets of data have been normalized to chondrite composition (Sun and McDonough 1989). In both sets of data, Gd did not return values above detection.

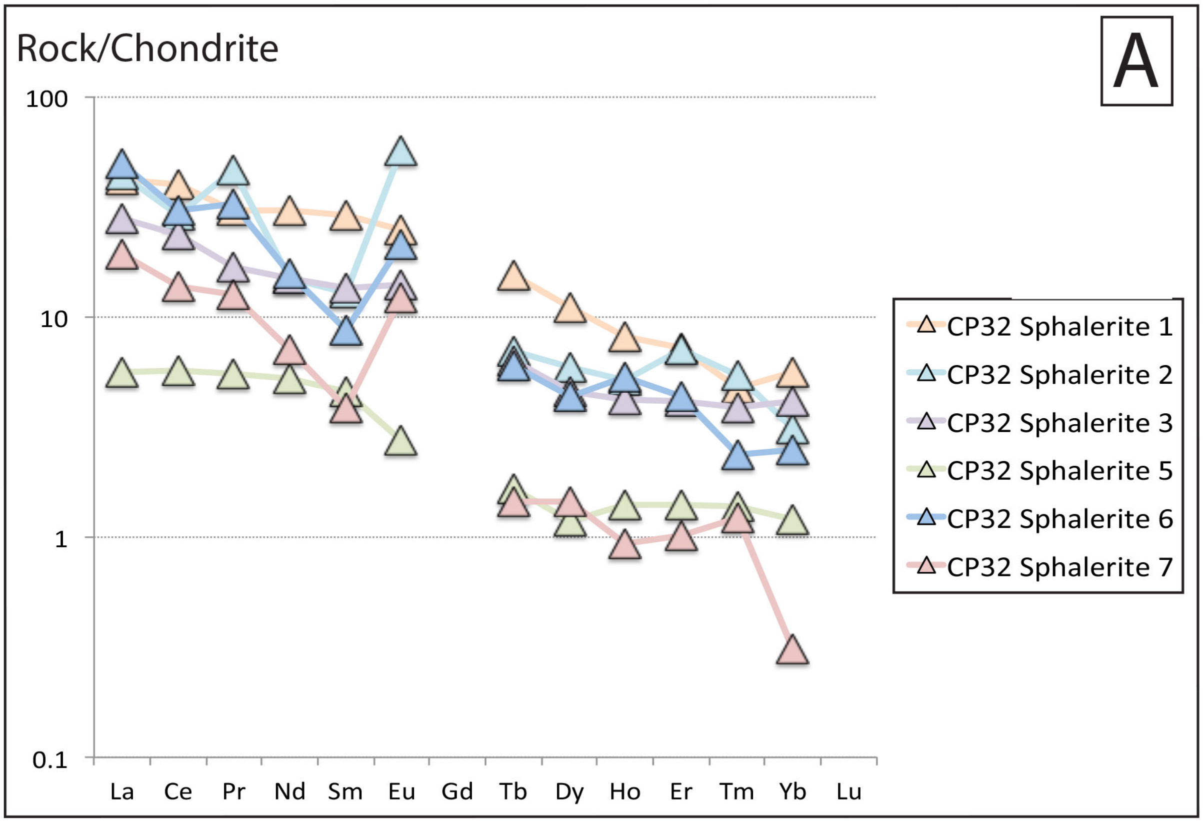
Rock/Chondrite
A
100
10
1
0.1
La
Ce
Pr
Nd
Sm
Eu
Gd
Tb
Dy
Ho
Er
Tm
Yb
Lu
CP32 Sphalerite 1
CP32 Sphalerite 2
CP32 Sphalerite 3
CP32 Sphalerite 5
CP32 Sphalerite 6
CP32 Sphalerite 7

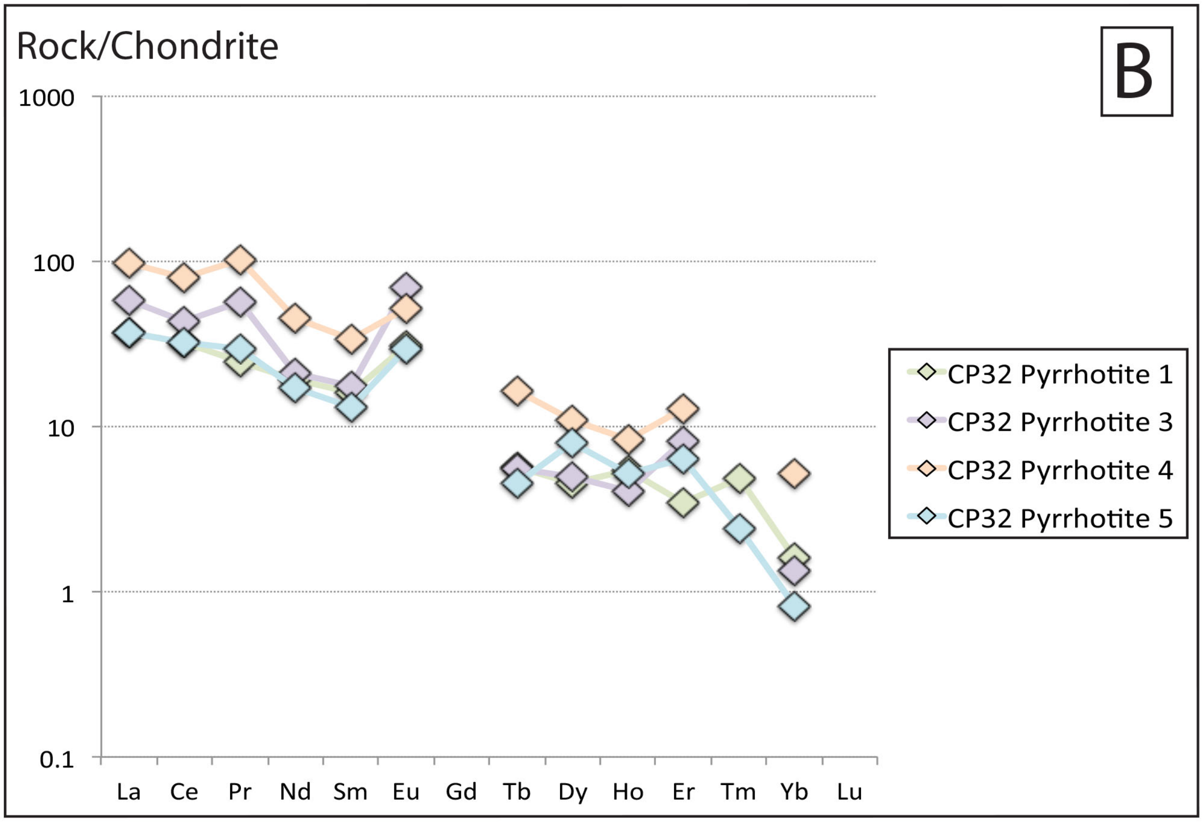
Rock/Chondrite
B
1000
100
10
1
0.1
La
Ce
Pr
Nd
Sm
Eu
Gd
Tb
Dy
Ho
Er
Tm
Yb
Lu
CP32 Pyrrhotite 1
CP32 Pyrrhotite 3
CP32 Pyrrhotite 4
CP32 Pyrrhotite 5

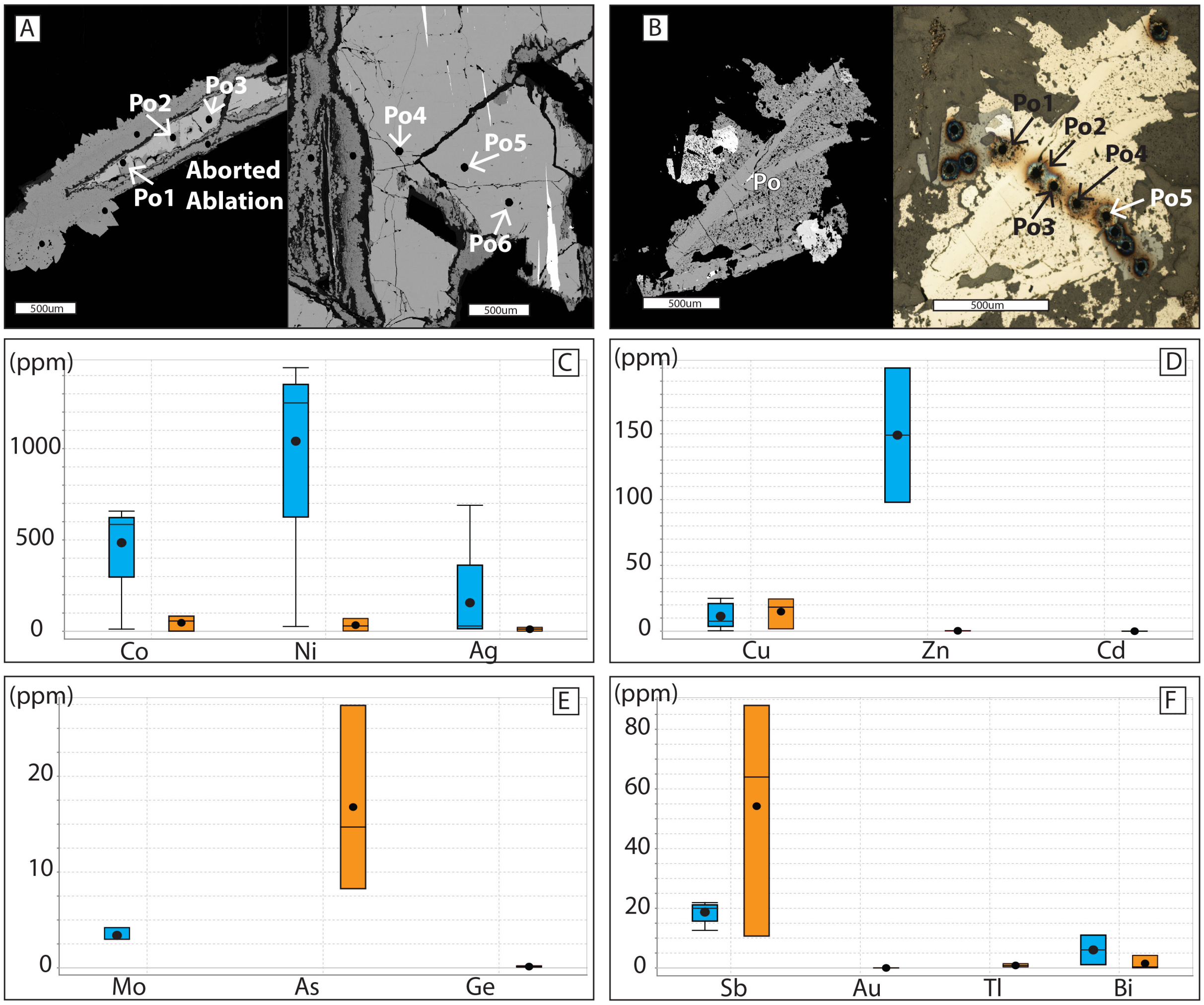

Figure 2.18 (A) Points of analysis from thin section CP26 (blue data). (B) Point of analysis from thin section CP32 (orange data). (C) Results of Co, Ni and Ag analyses (D) Cu, Zn and Cd analyses, (E) Mo, As and Ge analyses and (F) Sb, Au, Tl and Bi analyses.

2.7.2.1.4 Microthermometry

Microthermometric analyses were carried out on fluid inclusion assemblages (FIA) in two samples of the calcite veins. Calcite displayed no obvious growth zones in thin section, and isolated inclusions in random orientation within the mineral were considered to be primary (Roedder, 1984). Pseudosecondary inclusions were identified as those, which occurred on planes and terminated within a single crystal of the host mineral. Inclusions that appeared necked or decrepitated were not measured. For calcite hosted fluid inclusions, the inclusions were heated first before being cooled to avoid stretching of the fluid inclusions at low temperatures.

Fluid inclusions were rare in the majority of samples of calcite due to the opaque nature of the host mineral. However primary inclusions were found in one sample (HAM12-20-1922b). In this sample the majority of inclusions were around 10-15μm in diameter. Two FIA were identified within the center of calcite crystals (one pictured: Fig. 2.19A, B); FIA-33 and FIA-34 (Figure 2.21; Appendix 5).

Both FIA comprise two types of primary fluid inclusions with 80:20 proportions of liquid water to water vapor (Lw:Vw). Also present are single phase, Vw inclusions (Fig. 2.19A, B). Measurements of homogenization temperature and ice melting temperature (Tmi) were made on the two-phase inclusions. Homogenization temperatures (Th) ranged between 250.0°C and 255.0°C with one outlying measurement of 270°C in FIA-33 and between 215.0°C and 232.0°C in FIA-34. Ice melting (Tmi) occurred between -5.2°C and -5.8°C for FIA-33 and -5.9°C to -6.2°C for FIA-34, which translates to an equivalent NaCl salinity between 8.1 and 9.2 wt.% and 9.18 and 9.9 wt.% NaCl equiv (Bodnar, 1993).

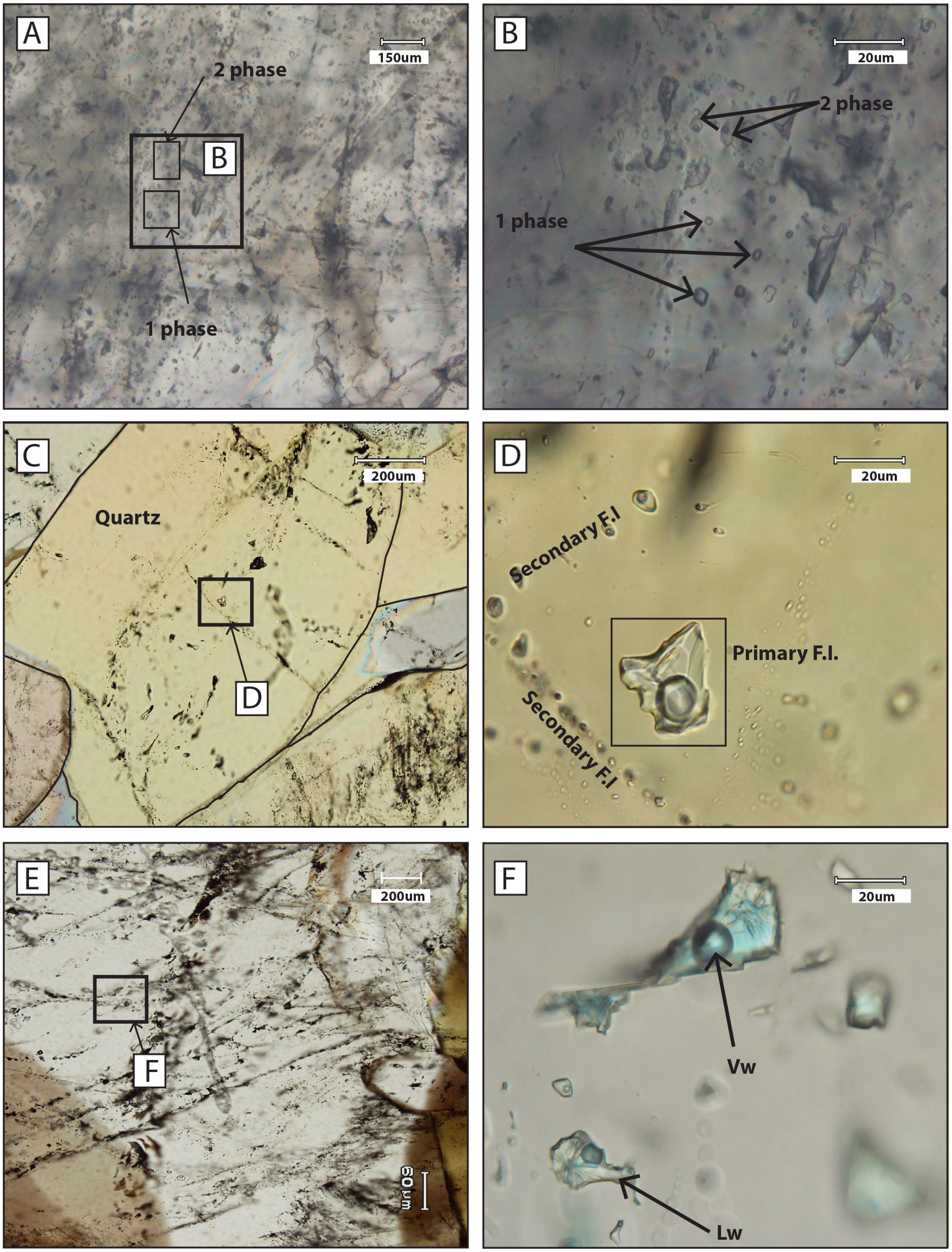

Figure 2.19 Plate of photomicrographs of fluid inclusion assemblages (FIAs). (A, B) two phase and single phase fluid inclusions from calcite veins (FIA-33). (C, D) single two phase inclusion from the quartz veins (FIA-7). (E, F) Two phase primary inclusions from the quartz veins (FIA-14). All terms are defined in 2.6.8 Microthermometry

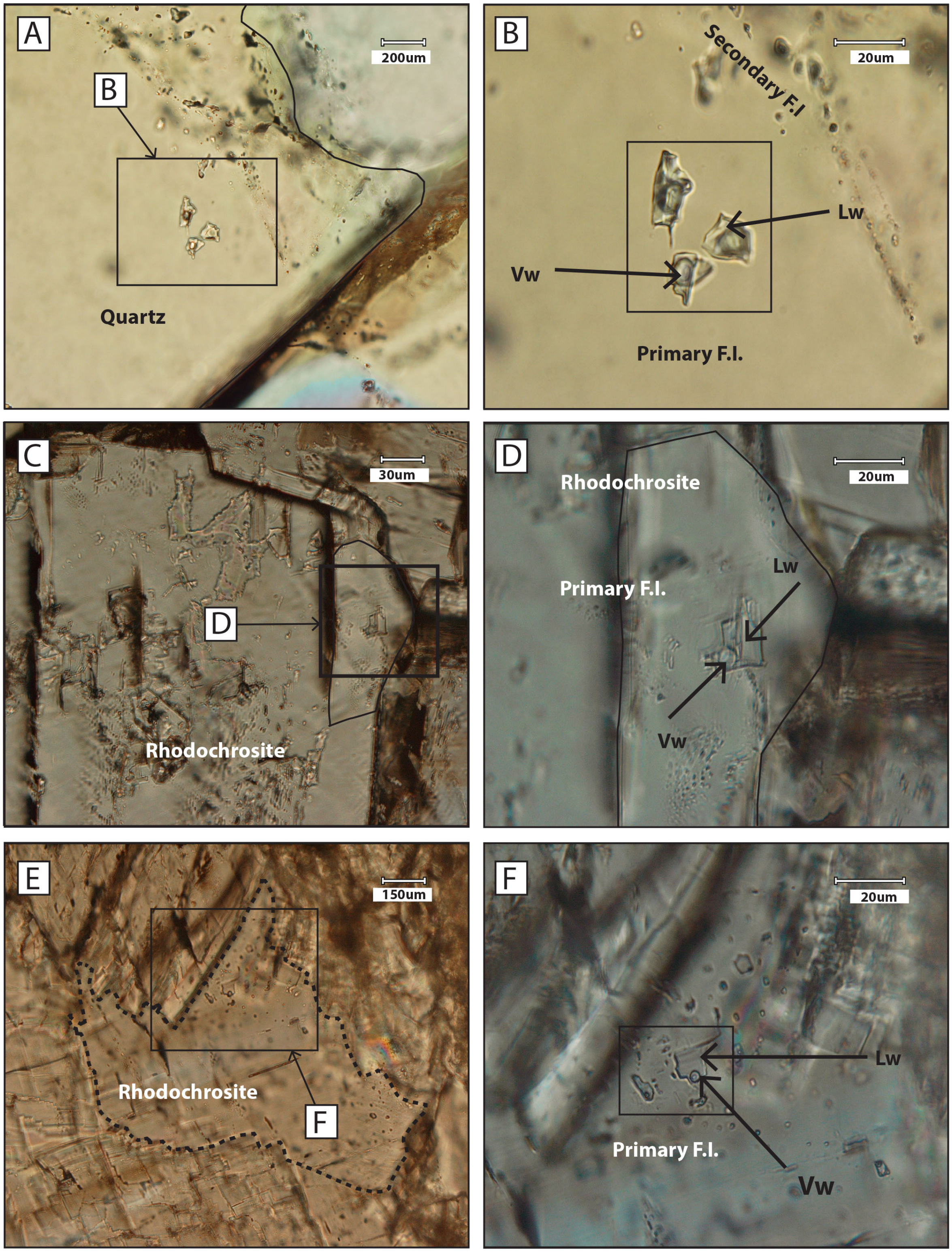

Figure 2.20 Plate of photomicrographs of fluid inclusion assemblages (FIAs). (A, B) cluster of primary, two-phase inclusions from the quartz veins. (FIA-10) (C, D) single primary two phase inclusion from the rhodochrosite veins (FIA-27) (E, F) primary two phase inclusions at the edge of a rhodochrosite crystal (FIA-32). All terms are defined in 2.6.8 Microthermometry

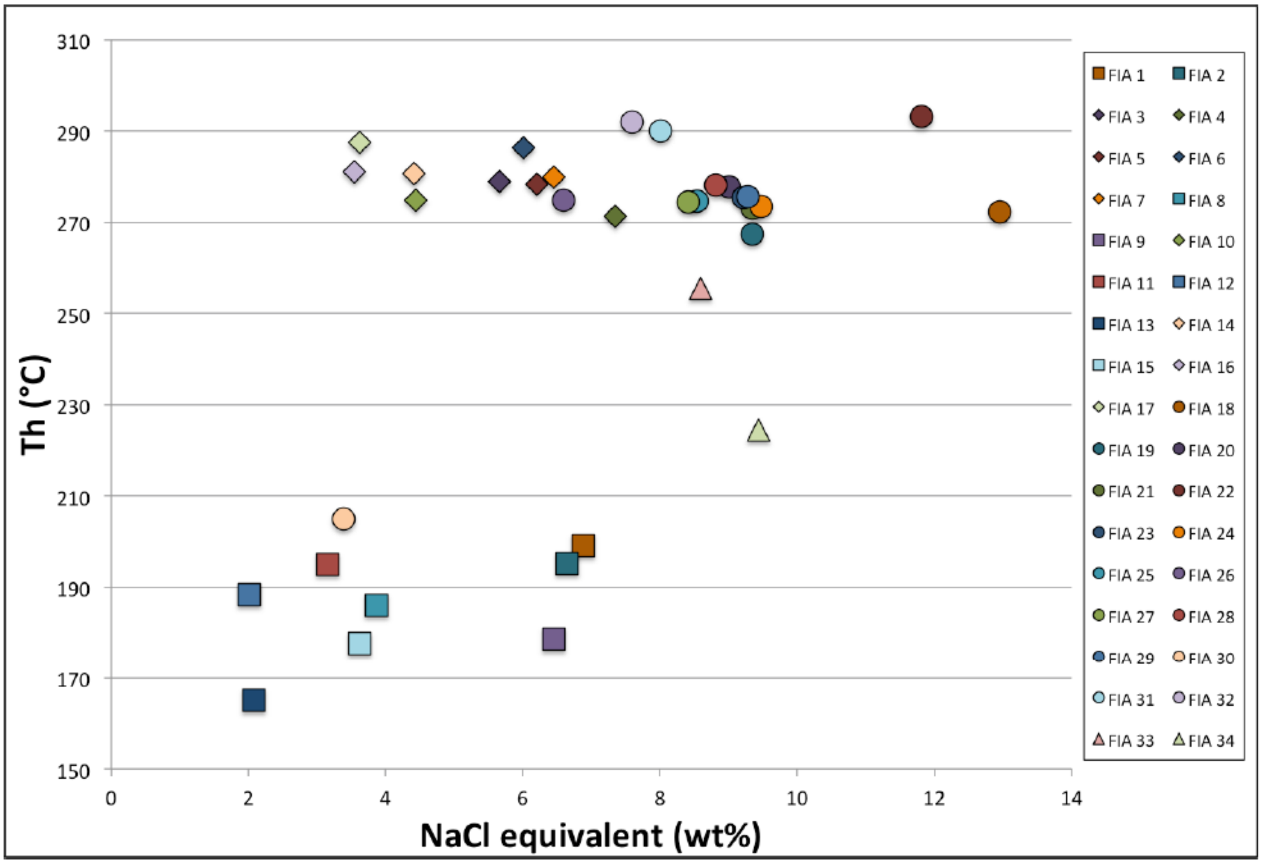

Figure 2.21 Plot of results from analysis of fluid inclusion assemblages from calcite (triangles), quartz (phase III) (diamonds), rhodochrosite (circles) and quartz (phase V) (squares). Each data point is the average data for a FIA; the color corresponds to the fluid inclusion assemblage, the shape to the paragenetic phase.

2.7.2.1.5 Isotopic Analyses

Calcite mineral separates from thirteen different samples were analyzed for oxygen, carbon, and strontium isotopes (Fig. 2.22 A, B; Fig. 2.23; Appendix 2). Analyses of the calcite samples returned $\delta^{18}O_{SMOW}$ values of -2.0‰ to 5.0‰, $\delta^{13}C_{PDB}$ values of -9.0‰ to 3.0‰, and $^{87}Sr/^{86}Sr$ between 0.735 and 0.740.

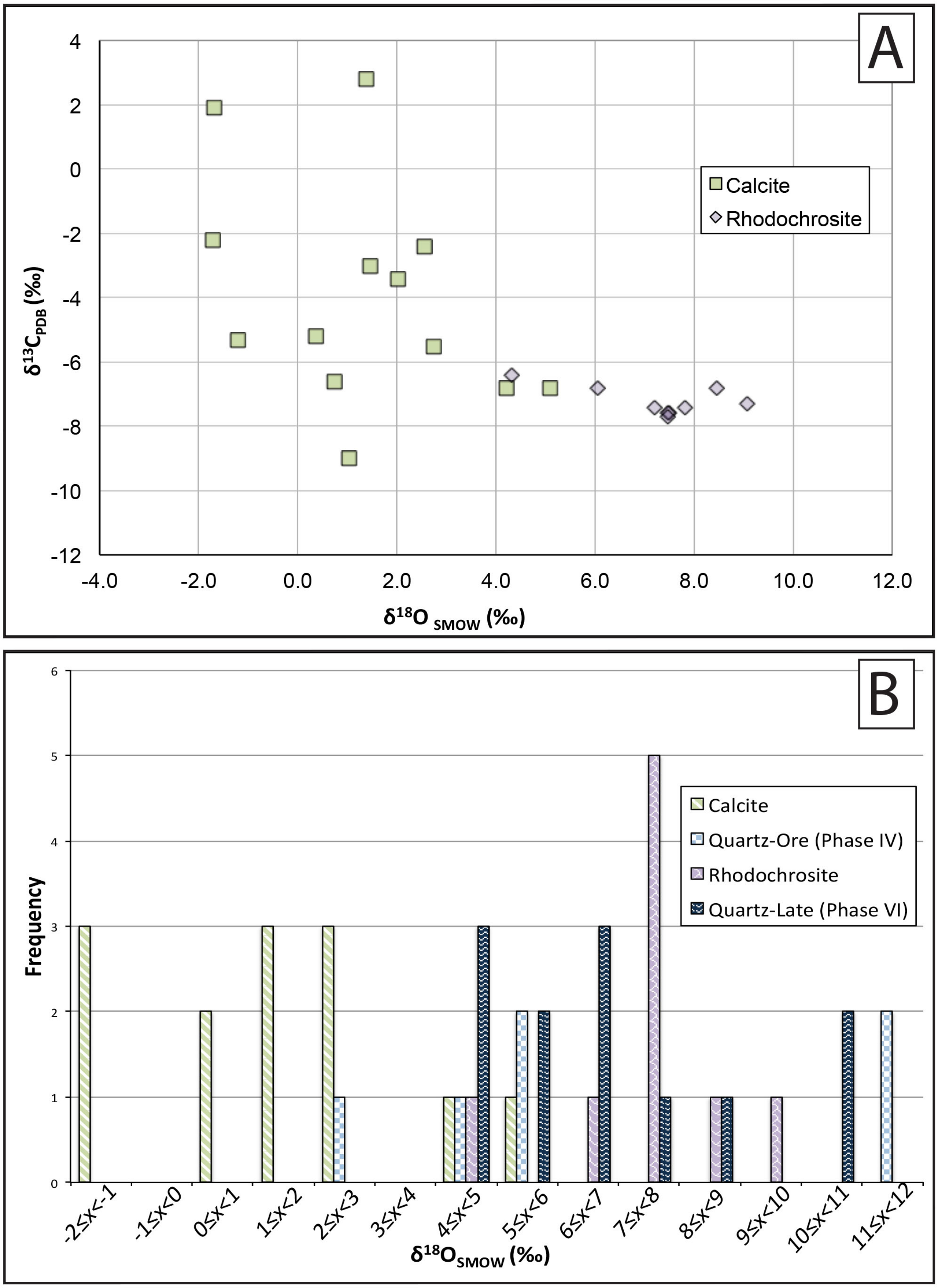
A
Calcite
Rhodochrosite
δ13CPDB (‰)
4
2
0
-2
-4
-6
-8
-10
-12
-4.0
-2.0
0.0
2.0
4.0
6.0
8.0
10.0
12.0
δ18O SMOW (‰)
B
Calcite
Quartz-Ore (Phase IV)
Rhodochrosite
Quartz-Late (Phase VI)
Frequency
6
5
4
3
2
1
0
-2≤x<-1
-1≤x<0
0≤x<1
1≤x<2
2≤x<3
3≤x<4
4≤x<5
5≤x<6
6≤x<7
7≤x<8
8≤x<9
9≤x<10
10≤x<11
11≤x<12
δ18OSMOW (‰)

Figure 2.22 Two plots of stable isotope data from powdered samples of calcite, quartz and rhodochrosite. (A) C vs O graph of data from rhodochrosite and calcite. (B) O histogram of data from calcite, quartz (phase III), rhodochrosite and late, quartz (phase V).

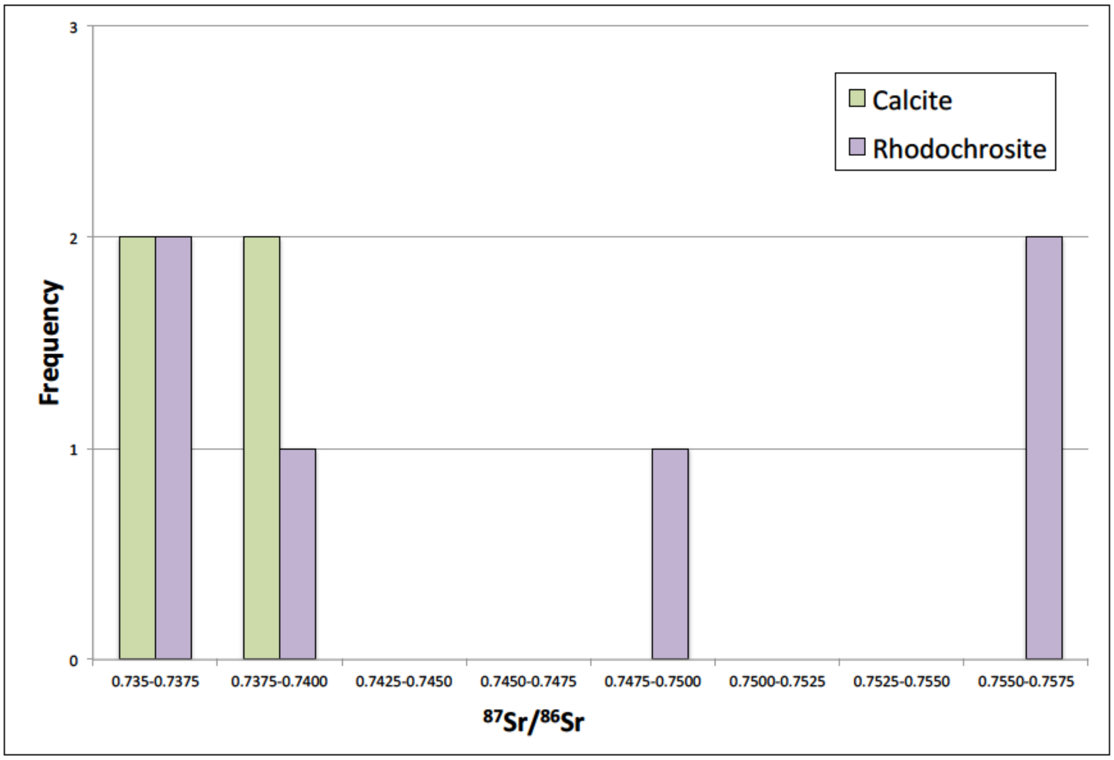

Figure 2.23 Histogram of strontium isotopic composition of rhodochrosite and calcite powdered samples.

2.7.2.2 Quartz Veins (Phase III)

2.7.2.2.1 Petrography and mineralogy (hand specimen, thin section, EPMA and XRD)

In this phase, fractures (1-3cm) are lined with quartz crystals, which grew parallel/subparallel to the direction of opening of the vein, σ_3. In hand specimen the quartz is commonly cloudy white (Fig. 2.24A) and has a number of crystal habits such as open space filling, drusy quartz and euhedral, interlocking quartz crystals (Fig. 2.24B, C). The euhedral quartz crystals and coeval sulfides overgrow the massive calcite crystals and sulfides of the earlier calcite veins (Fig. 2.9H, I; Fig. 2.24D). The sulfides in the quartz phase are primarily pyrite, chalcopyrite and arsenopyrite. As well as existing as overgrowths, phase III also contains individual, solitary grains of arsenopyrite (Fig. 2.24E) and infrequently pyrrhotite has rims of small grains of arsenopyrite alongside arsenic-rich pyrite (Fig. 2.24F). Overall there are fewer sulfides associated with this phase compared to the carbonate gangue mineral phases (Phase II and IV).

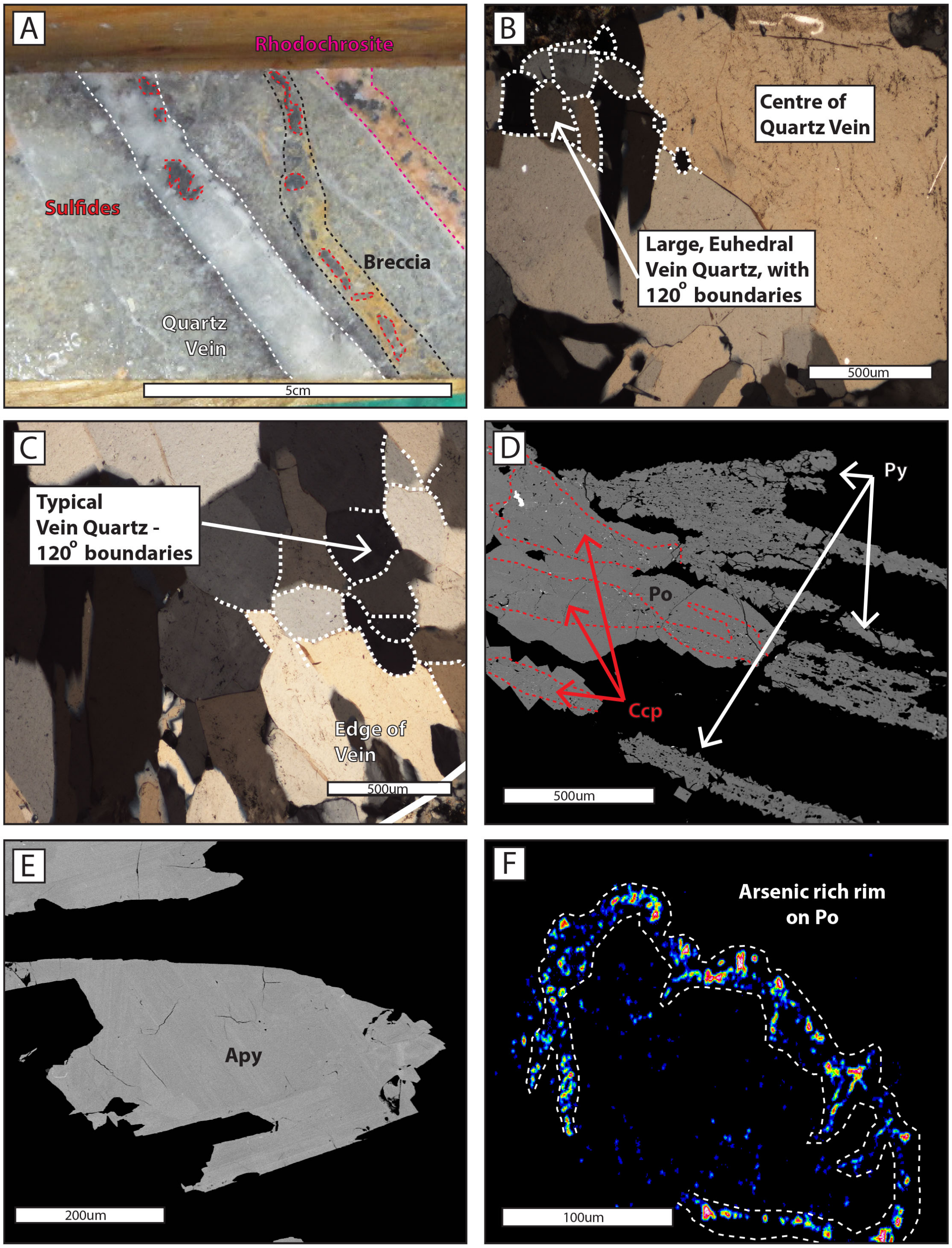

Figure 2.24 Plate showing a suite of typical features from quartz veins (phase III). (A) a typical quartz vein in core, alongside brecciation and rhodochrosite vein. (B, C) photomicrographs of typical quartz crystals displaying 120° degree crystal boundaries. (D) BSE imaging of sulfide

relationships between chalcopyrite and pyrrhotite. (E) an arsenopyrite grain. (F) elemental map of arsenic rich overgrowths (red grains are arsenopyrite) on pyrrhotite grains.

2.7.2.2.2 Microthermometry and Isotopic Analyses

Fluid inclusions were ubiquitous in the phase III quartz veins but no obvious growth zones were identified in thin section. Fluid inclusion assemblages were classified as primary, secondary and pseudosecondary using the rationale laid out in section 2.4 and 2.5.2.1.4. However only primary and pseudosecondary inclusions were studied for the purposes of this project.

Primary inclusions were the largest in size, up to 40μm in diameter, with pseudosecondary inclusions slightly smaller, 20-25μm. There were 17 FIA identified, several assemblages display very similar characteristics

All FIA in the phase III quartz veins contain two-phase fluid inclusions. The ratios of liquid water-to-water vapor vary from 95% to 50% Lw and 5% to 50% Vw (Fig. 2.19C-F; Fig 2.20A-B) with the majority of inclusions having ≥90% Lw. The homogenization temperatures of all FIA contained within the quartz ore stage vary between 268°C and 289°C with one outlier at 311°C. The final melting point of ice ranged between -5.2°C and -2.1°C which corresponds to salinity of 8.1 wt.% and 3.6 wt.% NaCl equiv (Bodnar, 1993)

Six phase III quartz mineral separates were analyzed for oxygen isotopes, returning $\delta^{18}O_{SMOW}$ values between 2.67‰ to 11.73‰ (Fig. 2.22B; Appendix 2).

2.7.2.3 Rhodochrosite Veins (Phase IV)

2.7.2.3.1 Petrography and mineralogy (hand specimen, thin section, EPMA and XRD)

Phase IV rhodochrosite veins are the second phase of carbonate gangue mineral veining and main ore mineralization stage. The rhodochrosite veins are 0.5-2cm wide, pink, fracture-filling veins. Rhodochrosite occurs in crustiform and drusy crystal forms, (Fig. 2.25A-C) suggesting the rhodochrosite grew into open space (Fig. 2.9C; Fig. 2.25D). Rhodochrosite forms high relief, euhedral crystals occasionally with composite zoning (Fig. 2.9C; Fig. 2.25D) and radial, anhedral, crustiform crystal forms (Fig. 2.25C, E).

The rhodochrosite veins contain up to 30% sulfides by volume (Fig. 2.24A, E). Galena and sphalerite are the most common sulfides present in the rhodochrosite veins, and form up to centimeter scale crystals (Fig. 2.25A). The sphalerite in this phase is very dark in color, almost black, and distinctively different to the ruby red sphalerite from phase II. Pyrite is a minor component in this paragenetic phase and commonly contains small inclusions of galena (Fig. 2.25F). Pyrite crystals from phase IV have subhedral crystal form, with some cockscomb terminations (Fig. 2.10E). Phase IV contains the major silver-bearing mineral in the Hammer Zone; freibergite. The freibergite is found within, or proximal to, sphalerite, as euhedral crystals or as exsolution lamellae (Fig. 2.25G, H). Chalcopyrite occurs in this phase of veining and replaces sphalerite (Fig. 2.25I; Fig. 2.26). Euhedral crystals of arsenopyrite are associated with sphalerite and galena (Fig. 2.25H).

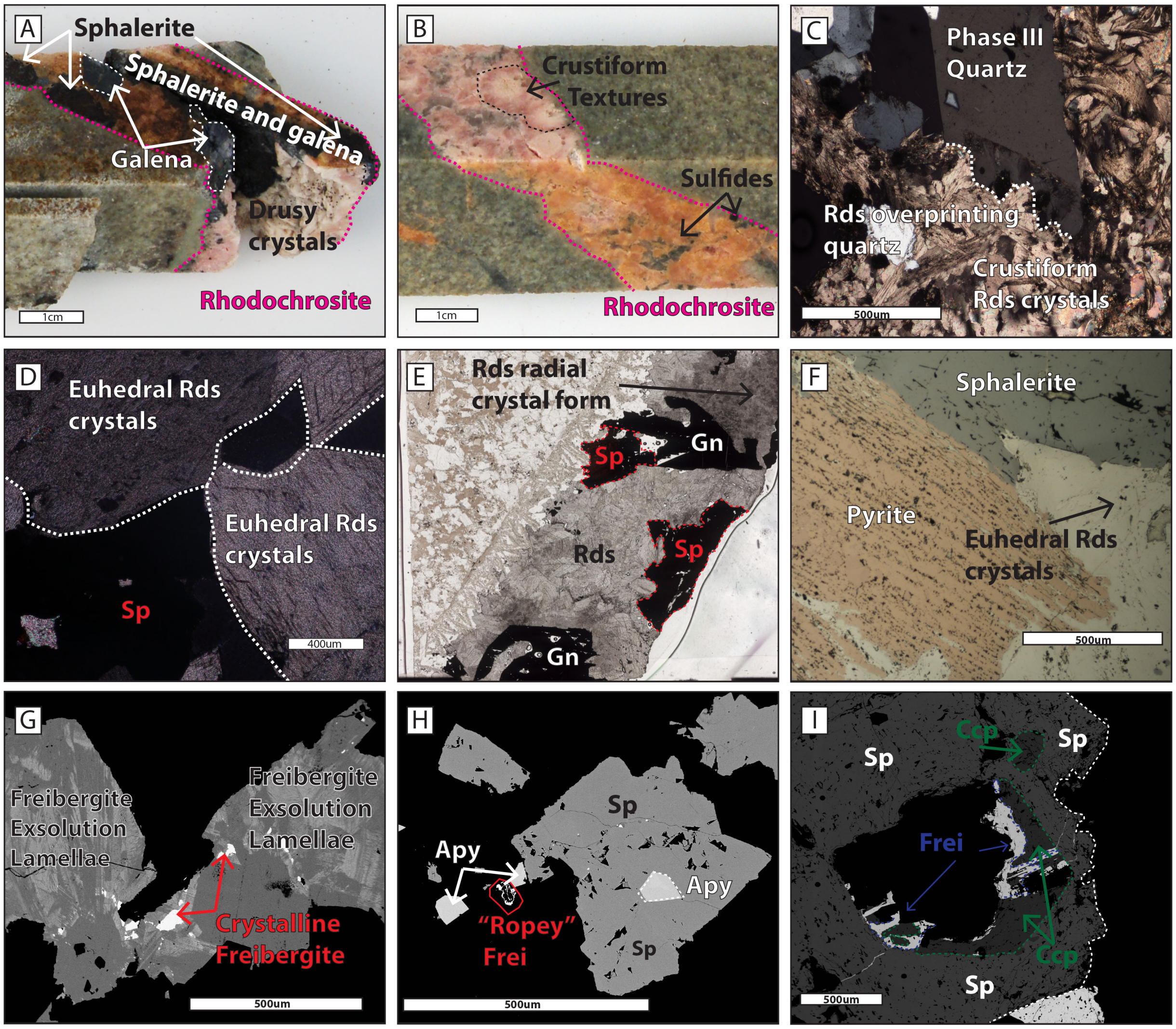

Figure 2.25 (A) Sulfide rich core sample displaying drusy crystal form. (B) Rhodochrosite vein in core displaying crustiform textures. (C) Photomicrograph of feathered rhodochrosite crystals typical of crustiform textures overprinting phase III quartz. (D) Photomicrograph in cross-polars of euhedral rhodochrosite displaying cleavage and high order interference colors. (E) Thin section scan displaying high proportion of sulfides in rhodochrosite veins and crustiform textures (top right). (F) Pyrite and sphalerite crystals showing limited mottling. (G) BSE image of sphalerite with crystalline freibergite inclusions alongside freibergite exsolution lamellae. (H) BSE image of large sphalerite crystals alongside smaller arsenopyrite crystals and "ropey" freibergite (bottom left). (I) BSE image of freibergite and chalcopyrite crystals hosted by sphalerite.

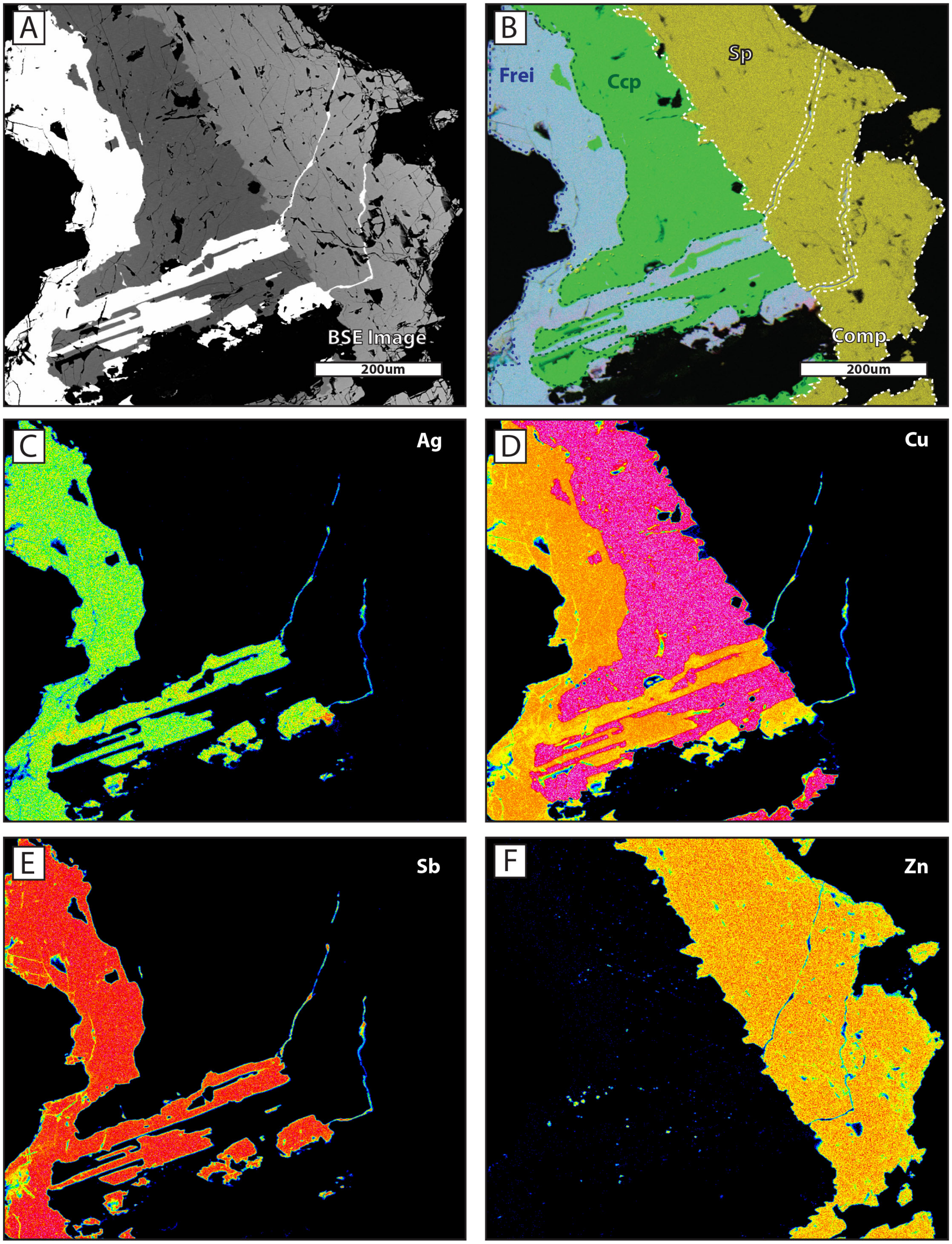

Figure 2.26 (A) BSE image of freibergite, chalcopyrite and sphalerite (L-R). (B) Composite map made up of the four elements mapped below; (C) Ag, (D) Cu, (E) Sb, and (F) Zn. The brighter the color, the higher the elemental abundance in each map.

2.7.2.3.2 EPMA Analysis (WDS and elemental mapping)

Sulfide

Point analyses were carried out using WDS on the five main sulfides from the rhodochrosite phase (Fig. 2.27A-F). The results returned from WDS analysis are plotted on X-Y plots (Fig. 2.13; Fig. 2.14) and summarized in table 2.2, which displays data from points of analysis of several transects. Zinc, manganese, iron and sulfur contents in sphalerite (Fig. 2.27A, D-F) varied between 49.0-56.3 wt.%, 0.5 to 1.5 wt.%, 9.5-16.0 wt.% and 33.7 to 35.5 wt.% respectively. Sphalerite hosted by rhodochrosite differs from that hosted by calcite in all four of the elements analyzed; the concentration of Zn and S was lower and that of Mn and Fe higher in nearly all samples analyzed.

Euhedral to subhedral galena (Fig. 2.26B) had Pb concentrations of 84.0 to 86.7 wt.%, sulfur values of 12.0 to 13.0 wt.%, antimony values that ranged from 0.23 to 1.22 wt.% and silver concentrations from below detection to 1.03 wt.%. Late, anhedral galena (Fig. 2.26F) had concentrations of 85.0 to 86.0 wt.% Pb, 13.5 to 13.7 wt.% S, 0.30 to 0.35wt.% Ag and 0.28 to 0.89 wt.% Bi. Both types of galena have elevated levels of Ag, Sb and Bi in contrast to the galena from phase II.

The freibergite analyzed from the rhodochrosite ore stage (Fig. 2.27A, D-E) returned values of 21.0 to 24.0 wt.% S, 4.0 to 6.0 wt.% Fe, 25.7 to 27.4 wt.% Sb, 0.5 to 2.0 wt.% Zn, 19.0 to 33.0 wt.% Ag, 13.0 to 23.0 wt.% Cu. Simple binary plots between these major elements show that as Cu decreases, Ag increases and as Sb increases Ag also increases (Fig. 2.13E, F).

The chalcopyrite analyzed returned values of 34.5 to 35.6 wt.% S, 9.3 to 31.0 wt.% Fe and 32.0 to 33.5 wt.% Cu. Chalcopyrite contains no minor elements.

Arsenopyrite had concentrations ranging from 43.0-44.0 wt.% As, 21.0-22.0 wt.% S and 35.0-39.6 wt.% Fe and up to 0.5wt.% Sb. Analysis of pyrite found the concentrations iron and sulfur, ranged between 52.0 to 54.0 wt.% and 45.0-46.0 wt.% respectively. Two samples of pyrite analyzed from one thin section had elevated levels of arsenic; 1.4 and 1.8 wt.% As, suggesting that some of the pyrite is arsenian pyrite (Deditius et al., 2008).

There is an interesting relationship between sphalerite and freibergite in some of the samples. In Fig. 2.28, crystalline freibergite can be observed, hosted by sphalerite. Proximal to this crystalline freibergite are laminar inclusions in sphalerite. These inclusions, outlined in Fig. 2.28B-E, are anomalously high in Ag, Cu and Sb and are thought to be freibergite exsolution lamellae (Appendix 1).

Carbonate

Two carbonate mineral end members were identified by WDS analysis in phase IV. The first end member identified was kutnahorite ($CaMn(CO_3)_2$) (Fig. 2.29A). Analysis of kutnahorite returned Ca and Mn values at almost 50:50 proportions (approx. 20 wt.% each). The other end member is true rhodochrosite ($MnCO_3$), containing over 30wt.% Mn and less than 10 wt.% Ca (Fig. 2.29B-D). Within many of the larger veins, transects of EPMA points returned values close to the kutnahorite end member. As far as can be seen via a microscope or BSE imaging, these changes in cation concentrations do not correlate to any change in color or crystal habit. Fe is the next most prominent cation in the rhodochrosite ore stage carbonates. Commonly, it occurs in concentrations varying between 5 and 20wt.%.

The 16-point transect presented in Fig 2.29D cuts through a crustiform rosette. The lack of change in chemistry, bar one point, shows that whilst the color of a crustiform rosette may change with zonation, the major element chemistry stays constant.

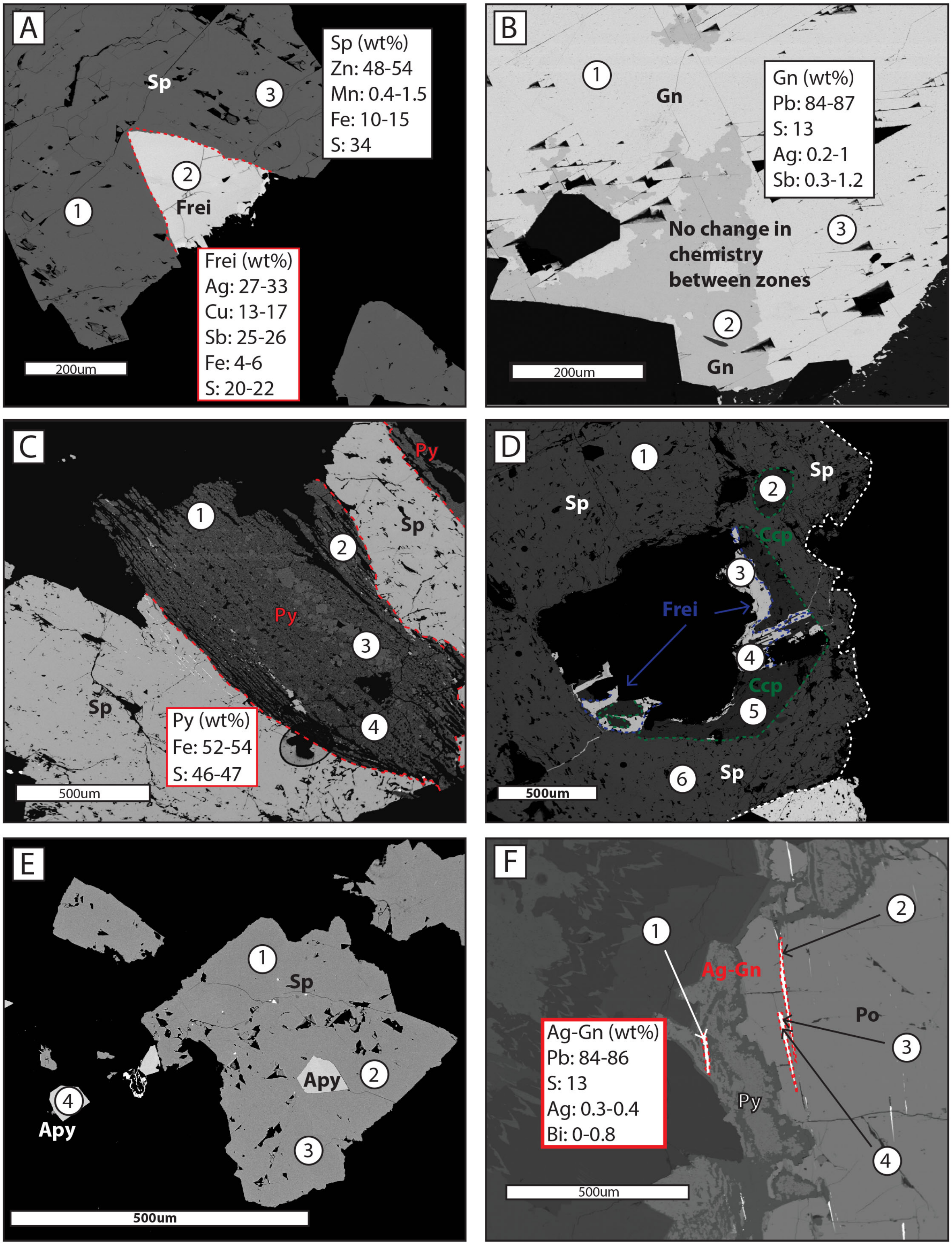

Figure 2.27 Boxes show range of values for each element above detection. (A) sphalerite and freibergite. (B) galena. (C) pyrite. (D) sphalerite, freibergite and chalcopyrite. (E) sphalerite and arsenopyrite. (F) galena. All data for labeled points found in Table 2.2

	Pb (wt.%)	**As (wt.%)**	**S (wt.%)**	**Bi (wt.%)**	**Fe (wt.%)**	**Sb (wt.%)**	**Zn (wt.%)**	**Ag (wt.%)**	**Cu (wt.%)**	**Mn (wt.%)**	**Total**
A											
1	~	~	34.81	~	13.48	~	51.16	~	~	1.05	100.90
2	~	~	21.92	~	4.91	26.33	1.40	29.92	16.10	~	100.73
3	~	~	34.35	~	13.46	~	51.05	~	~	1.32	100.53
B											
1	86.68	~	13.49	~	~	0.44	~	0.21	~	~	100.95
2	85.30	~	13.48	~	~	0.58	~	0.38	~	~	99.89
3	86.28	~	13.41	~	~	0.39	~	0.19	~	~	100.37
C											
1	~	~	53.49	~	46.72	~	~	~	0.04	~	100.40
2	~	~	52.91	~	45.74	~	~	~	0.07	~	98.83
3	~	~	53.11	~	46.78	~	~	~	0.04	~	100.16
4	~	~	53.56	~	46.76	~	~	~	0.04	~	100.45
D											
1	~	~	34.83	~	13.12	~	51.09	~	~	0.93	100.55
2	~	~	34.57	~	13.73	~	51.09	~	~	0.93	100.62
3	~	~	21.76	~	4.44	26.27	1.88	30.11	15.99	~	100.62
4	~	~	21.89	~	5.06	26.31	1.30	29.03	16.45	~	100.13
5	~	~	34.85	~	30.74	~	~	~	33.13	~	99.09
6	~	~	34.48	~	13.32	~	51,47	~		0.88	100.53
E											
1	~	~	33.70	~	10.95	~	54.63	~	~	0.43	99.88
2	~	~	34.03	~	9.57	~	56.36	~	~	0.35	100.46
3	~	~	34.03	~	9.75	~	56.18	~	~	0.38	100.59
4	~	43.97	21.25	~	35.56	~	~	~	~	~	101.49
F											
1	85.67	~	13.57	0.30	0.39	~	~		~	~	100.19
2	85.14	~	13.46	0.89	0.75	~	~	0.34	~	~	100.76
3	85.34	~	13.63	0.82	0.80	~	~	0.36	~	~	101.15
4	85.96	~	13.69	0.28	0.90	~	~		~	~	101.14

Table 2.3 shows data for Figure 2.27. Capital letters refer to image in plate, number in left column refers to analysis point. "~"symbol refers to data that is below the limits of detection, which can be found in Appendix 1.

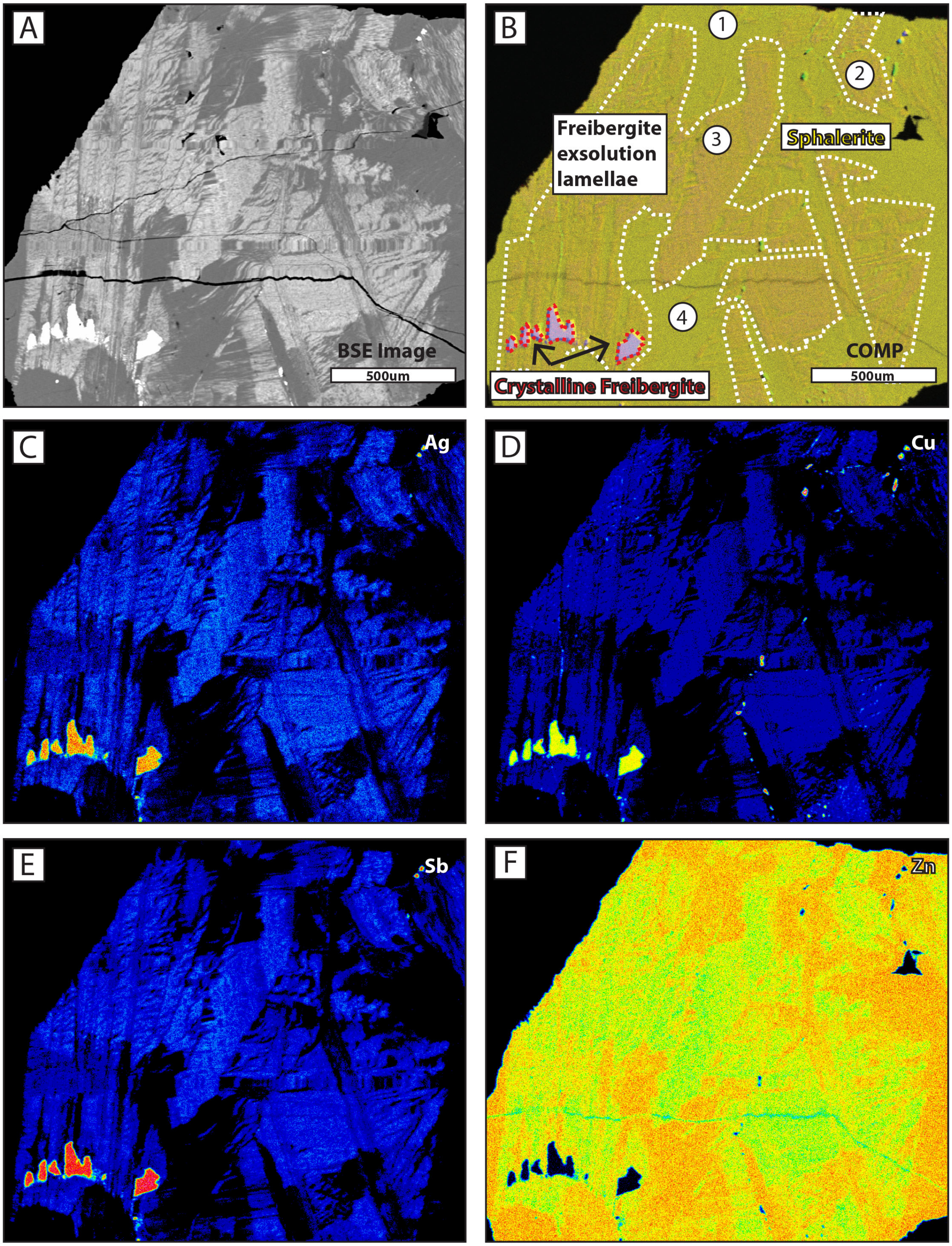

Figure 2.28 (A) BSE image of the area mapped. (B) Composite image of the four elemental maps analyzed; (C) Ag, (D) Cu, (E), Sb and (F) Zn. The outlined phases are crystalline freibergite in the bottom left (in red), and exsolution lamellae across the majority of the sample (in white). Sphalerite also contains small chalcopyrite inclusions.

Element	***Ag (wt.%)***	***Fe (wt.%)***	***Cu (wt.%)***	***S (wt.%)***	***Zn (wt.%)***	***Sb (wt.%)***	***Mn (wt.%)***	***Totals (wt.%)***
Points from Fig. 2.13C								
1 (sp)	0.82	11.16	0.21	33.03	53.40	0.33	0.34	99.42
2 (el)	9.43	10.34	2.36	30.35	40.61	5.40	0.28	98.83
3 (el)	28.91	6.16	16.86	21.68	1.45	25.84	~	100.99
4 (sp)	0.05	9.82	0.2	33.1	55.13	~	1.30	100.05
Other points								
5 (sp)	~	11.14	~	33.33	54.82	~	0.34	99.88
6 (sp)	~	11.18	~	33.40	54.6	~	0.3	99.78
7 (el)	6.81	10.53	1.83	31.22	44.72	3.68	0.31	99.19
8 (el)	8.48	10.64	2.2	30.77	41.84	4.79	0.33	99.19
9 (el)	5.35	11.15	1.33	31.82	46.71	2.86	0.33	99.64
10 (el)	3.147	11.25	3.34	32.52	47.24	1.58	0.31	99.46
11 (el)	9.30	7.28	2.57	30.32	44.13	5.61	0.52	99.82
12 (el)	4.34	10.35	1.10	32.09	49.69	2.27	0.22	100.14
13 (el)	~	10.89	~	33.32	55.16	~	0.31	99.86
14 (el)	6.20	9.88	3.11	31.40	46.18	3.62	0.24	100.71
15 (el)	~	10.92	~	33.39	55.19	~	0.25	100.03
16 (el)	6.85	6.87	2.02	31.28	48.48	3.91	0.21	99.69
17 (el)	4.83	8.70	2.49	31.77	48.39	2.59	0.63	99.46
18 (el)	17.47	7.36	4.78	27.85	32.83	9.57	~	100.05
19 (el)	10.76	8.73	3.13	29.97	41.04	5.88	~	99.69

Table 2.4 Data collected from WDS analysis of sulfides from the sample in Figure 2.27 (points 1-4) and other samples similar to this one (5-19). Dashed line indicates values below detection limits, which are found in Appendix 1. Labels (sp) and (el) correspond to analysis of crystalline sphalerite and exsolution lamellae, respectively.

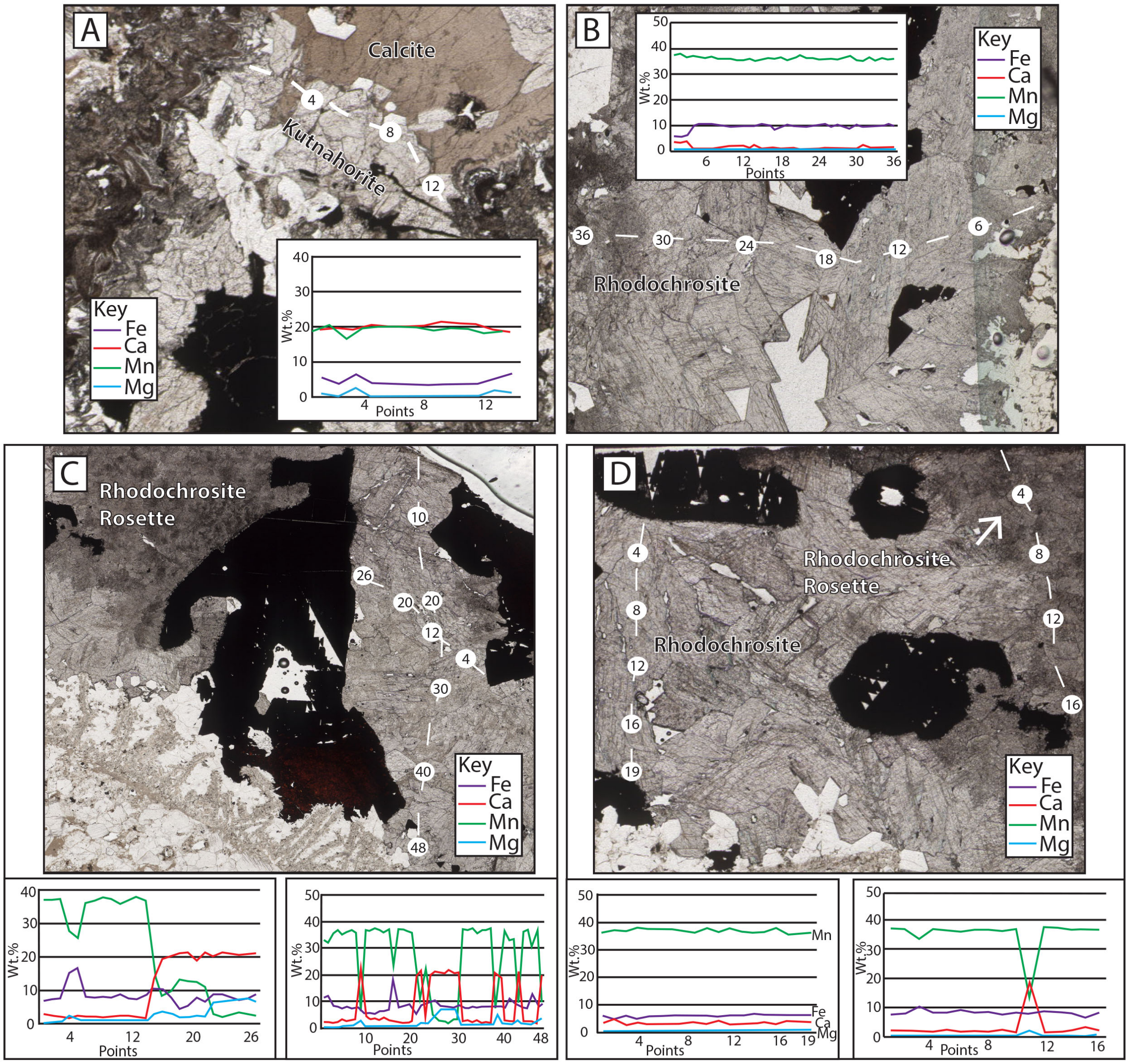

Figure 2.29 Concentrations of Fe, Ca, Mn and Mg in (A) kutnahorite crystals overprinting earlier calcite crystals. (B) rhodochrosite vein. (C) rhodochrosite vein. (D) a rhodochrosite vein, and across a rhodochrosite rosette texture.

2.7.2.3.3 LA-ICP-MS

LA-ICP-MS analyses were performed upon one thin section from the rhodochrosite phase, C23, from hole HAM 12-18 at a depth of 184.50m and upon mineral overgrowths in sample CP26 from the calcite veins. These samples were chosen for analysis as they contained the best example of sphalerite (C23), which is spatially related to the major silver bearing phase, freibergite and the best example of pyrite (CP26).

Sphalerite

Sphalerite was analyzed for trace and minor elements in thin section C23 (Fig. 2.30A). Analysis of sphalerite found concentrations of Cd, Co, Cu, Ga, Se, Ag and In (Appendix 4; Fig 2.30C, D) above the detection limits. Unlike the sulfides from phase II, the LA-ICP-MS analysis of sulfides from phase IV did not return any concentrations for REE above detection.

Pyrite

Five points from pyrite overgrowths on pyrrhotite were analyzed in thin section CP26 (Fig. 2.30B). The pyrite analyzed had elevated levels of Co, Ni Cu, Zn Ge, As, Se, Ag, Cd, Sb, Au, Tl and Bi (Appendix 4; Fig. 2.30E, F).

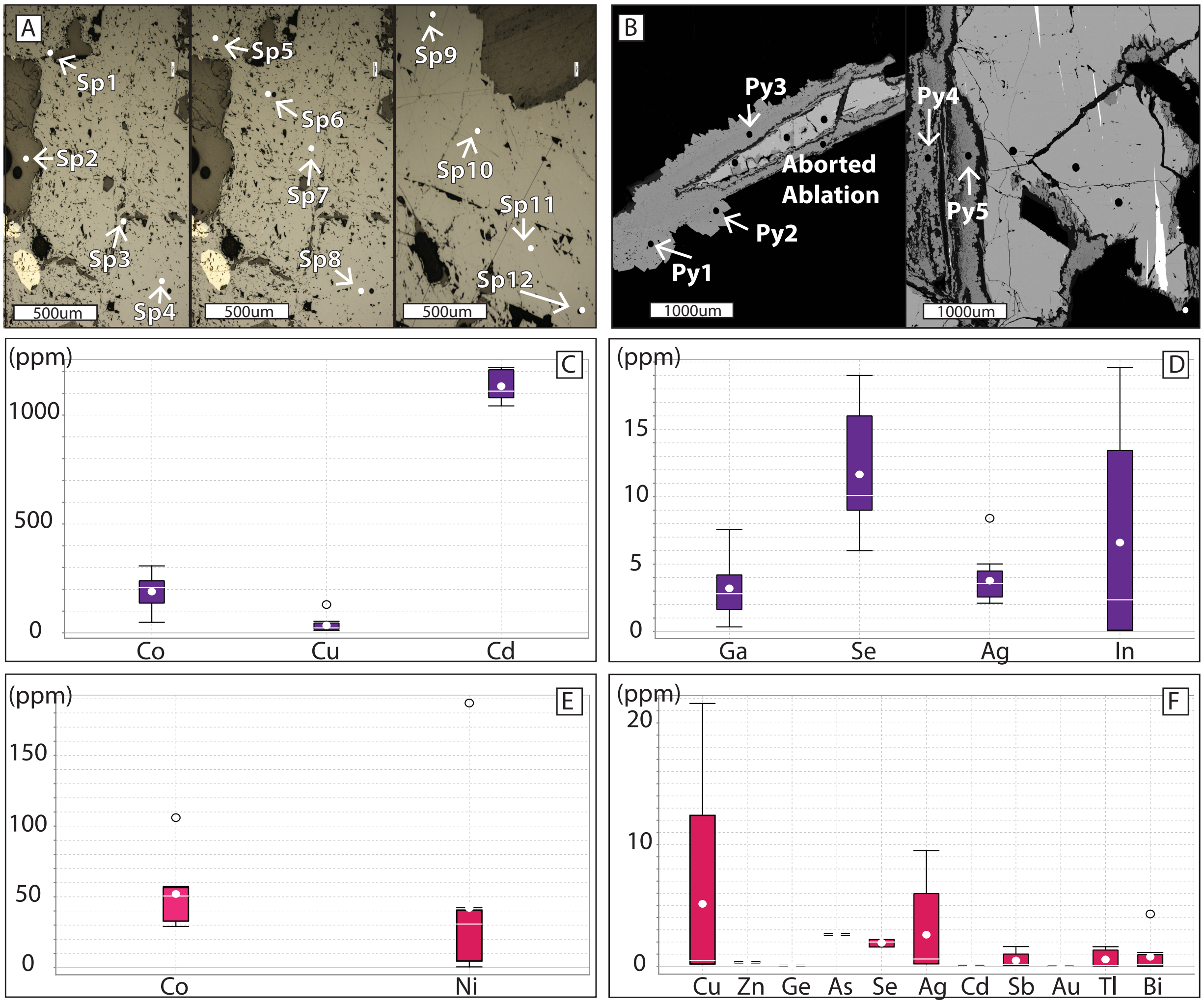

Figure 2.30 Plate showing results of analysis of sphalerite and pyrite by LA-ICP-MS (A) point analyzed in sphalerite. (B) points analyzed in pyrite. (C) results for analysis of Co, Cu and Cd in sphalerite. (D) Ga Se, Ag and In concentrations in sphalerite. (E) Co and Ni concentrations in pyrite. (F) Cu, Zn, Ge, As, Se, Ag, Cd, Sb, Au, Tl and Bi in pyrite. All values are in ppm.

2.7.2.3.4 Microthermometry

Rhodochrosite was the only mineral analyzed to contain growth zones; hence, primary fluid inclusions could be identified. Pseudosecondary inclusions were identified as planes of fluid inclusions terminating at the primary growth zones. The inclusions were heated first before being cooled to avoid stretching of the fluid inclusions.

Primary fluid inclusions had diameters up to 20μm. Pseudosecondary inclusions were smaller. Fourteen FIA were identified in the rhodochrosite veins. The majority of FIA have varying phase proportions, resulting in different homogenization temperatures.

The FIA from rhodochrosite gangue minerals contains two-phase inclusions with phase proportions that vary between 95 and 70% liquid water (Fig. 2.20E, F). The homogenization temperatures and melting temperature of ice range between 267.5°C and 290.0°C and -9.1°C and -4.1°C, respectively. The latter corresponds to a range in salinity from 6.6wt.% and 13.0 NaCl wt.% equiv. One secondary FIA (with a single fluid inclusion) had a lower T_h and T_{mi} of 205.0°C and -2.1°C (salinity of 3.4 NaCl equiv. wt.%) (Bodnar, 1993).

Fluid inclusions in rhodochrosite had similar T_h to the phase II calcite and phase III quartz however the overall salinity of the inclusions was higher in this stage (Fig. 2.21).

2.7.2.3.5 Isotopic Analyses

Oxygen, carbon and strontium isotopes were analyzed in rhodochrosite (Fig. 2.22; Fig. 2.23). The samples had $\delta^{18}O_{SMOW}$ values of -4.0‰ to 9.0‰, $\delta^{13}C_{PDB}$ values of -6.0‰ to -8.0‰, and $^{87}Sr/^{86}Sr$ values between 0.735 and 0.755.

In addition, galena and sulfur separates from a rhodochrosite vein were analyzed for $\delta^{34}S_{CDT}$ values (Table 2.4), yielding $\delta^{34}S_{CDT}$ values of between 10‰ and 11‰ for galena and 9‰ and 10‰ for sphalerite.

Sample	***δ $^{34}S_{CDT}$***
Galena	*10‰*
Galena	*11‰*
Sphalerite	*9‰*
Sphalerite	*10‰*
*Anvil Batholith Whole Rock**	*6-10‰*
*Early Cretaceous Selwyn Basin Intrusives Whole Rock**	*1-14‰*

Table 2.5 Sulfur isotopic compositions of two minerals from the rhodochrosite ore stage (galena and sphalerite) and two local reservoirs. Data for the Anvil Batholith whole rock and early Cretaceous Selwyn Basin intrusives whole rock found in Rasmussen (2013) are denoted by a star (*).

2.7.2.4 Brecciation

Following the rhodochrosite vein phase is the first phase of brecciation (Breccia I). The brecciation occurred in a 5-10cm wide zone and had a sharp contact with surrounding host rock. The breccia contains clasts of host rock, vein quartz, rhodochrosite and calcite and sulfides (Fig. 2.31A-D). The clast sizes vary from centimeter to micron scale and are poorly sorted. Host rock clasts are the biggest, with calcite and rhodochrosite vein material and sulfide clasts the smallest (Fig. 2.31C, D). Pyrite and sphalerite occur (Fig. 2.31E), with pyrite present in two forms. The first form of pyrite occurs as angular clasts (Fig. 2.31D). The second form of pyrite is as cement, occurring alongside the microcrystalline quartz. (Fig.2.31D, F).

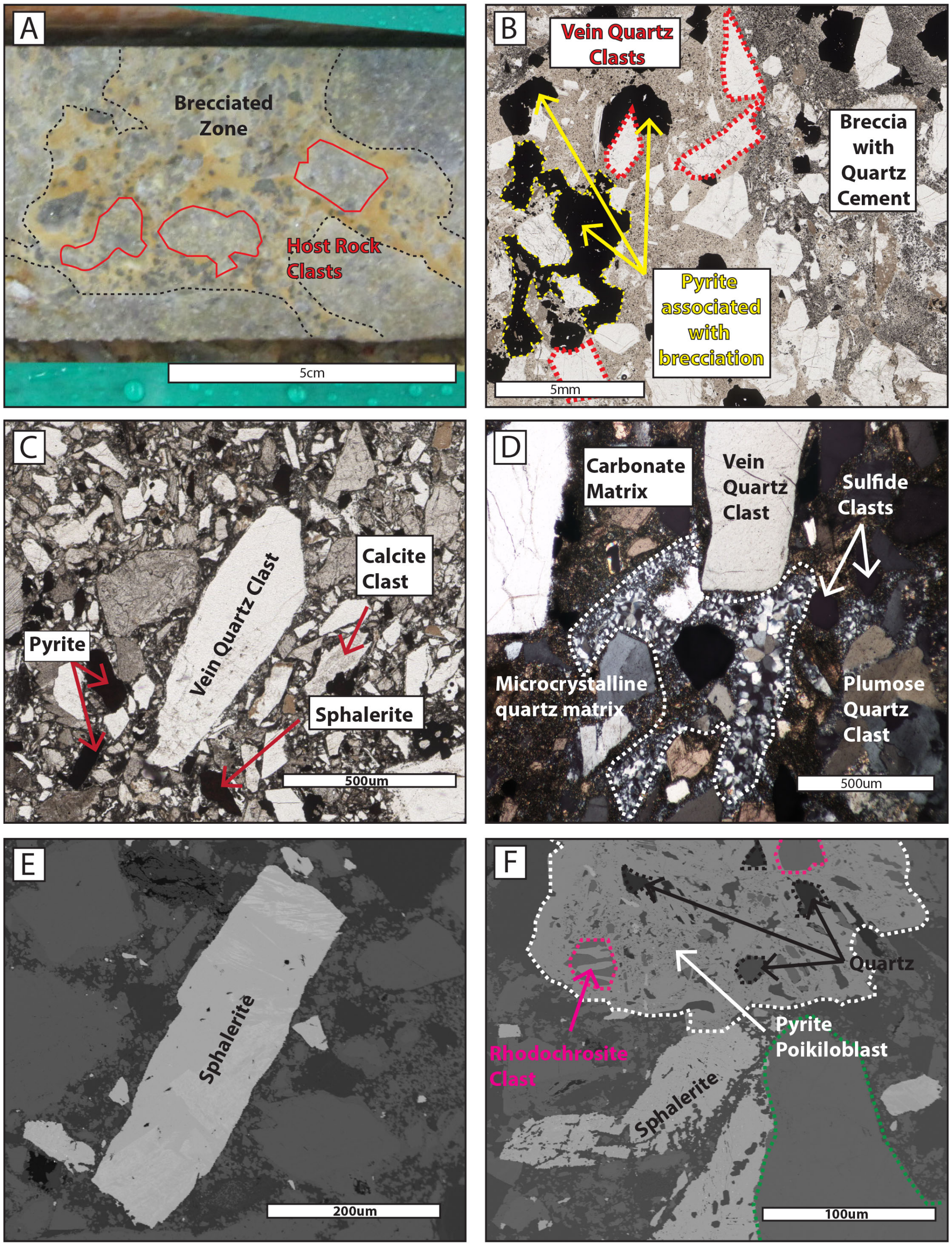

Figure 2.31 Plate showing various features associated with Breccia I. (A) typical texture of breccia I, quartz rich matrix, large host granite clasts and smaller sulfide clasts. (B) portion of a thin section scan showing pyrite crystals, growing around vein clasts and the quartz rich nature of the cement. (C) photomicrograph of various clasts, including vein quartz, sphalerite and calcite. Also labeled is pyrite found in the matrix of the breccia. (D) BSE image of sphalerite. (E) BSE image of pyrite poikiloblast containing inclusions of rhodochrosite and quartz alongside sphalerite clast. (F) photomicrograph showing carbonate, microcrystalline and cryptocrystalline quartz, which makes up the matrix of breccia I.

2.7.2.5 Alteration associated with Hammer Zone Mineralization (Phase V)

2.7.2.5.1 Petrography and mineralogy (hand specimen, thin section, EPMA and XRD)

Alteration in the Hammer Zone is restricted due to the quartz rich nature of the host rock. Argillic and propylitic alteration (Fig. 2.32A) are associated with mineralization (Phases II-IV). However due to the close spatial association of all the veins, it was not possible to confidently associate one phase of veining with a specific alteration assemblage and so they are discussed separately in this section.

Propylitic alteration was identified by an increase in the number of green minerals, predominantly chlorite, giving the rock a greenish hue in hand specimen. In thin section, propylitic alteration comprises chlorite and cryptocrystalline sericite and quartz (Fig. 2.32B, C). The chlorite has crystal forms similar to the biotite from the host rock (Fig. 2.32B). XRD analysis identified the chlorite to be clinochlore. Albite in the host rock has been altered to cryptocrystalline quartz and white mica (Fig. 2.32C). This alteration destroys the twinning textures in albite, unlike the potassic alteration associated with the Anvil Suite Granite. Sanidine remains in this phase, with large, twinned crystals still present (Fig. 2.32C).

The argillic alteration zone was yellow to cream colored, contained high proportions of clay minerals and was easily scratched with a steel-tipped scratcher. In thin section, the assemblage is characterized by large amounts of microcrystalline white mica with a corresponding decrease in the amount of clinochlore (Fig. 2.32D). The intensity of feldspar alteration is similar in the two alteration types, however, the intensity of alteration in the rock as a whole is different (Fig. 2.32E, F).

Whilst the alteration was hard to identify in the field, it was much easier in core. The boundary between unaltered and altered granite varies from gradual to sharp. The contacts between the alteration zones were also varied, with both sharp (Fig. 2.32A) and gradational boundaries present. Similarly to the boundary between the alteration and the granite, the controls on the sharp or gradational contacts of the alteration zones were not identifiable.

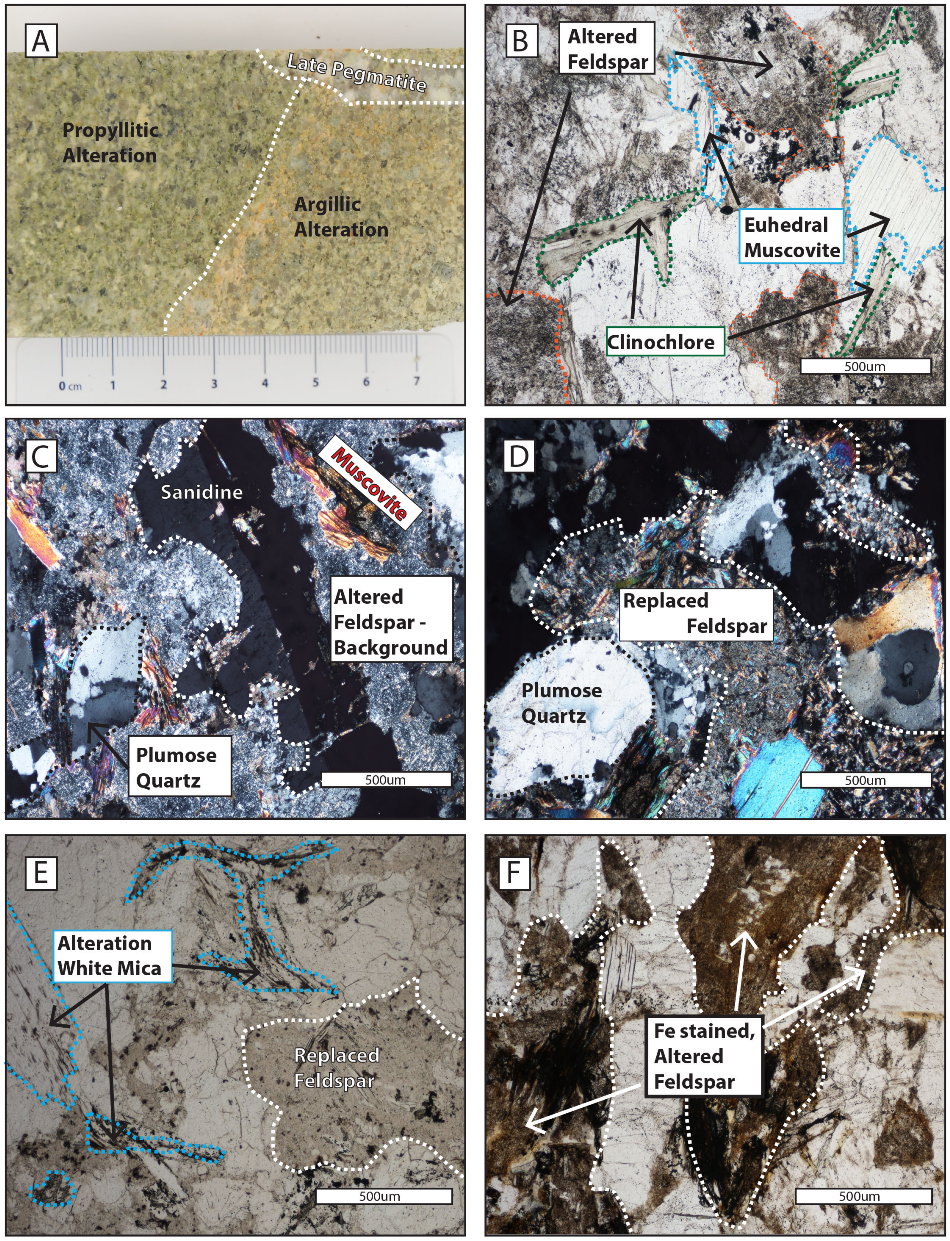

Figure 2.32 Plate showing various features associated with alteration related to the ore stage mineralization. (A) Photograph of core showing propylitic alteration in sharp contact with argillic, gradual contacts also exist. (B) Photomicrograph of typical propylitic alteration in PPL, note; biotite altered to clinochlore and heavily altered feldspars. (C) Photomicrograph of propylitic alteration in XP, note; feldspar alteration is quartz and mica rich, euhedral and anhedral mica present. (D) Photomicrograph of argillic alteration, feldspar replacement is mica rich, anhedral and euhedral mica present. (E) Photomicrograph of high proportion of white mica present in euhedral and anhedral crystal forms in argillic alteration. (F) Photomicrograph of Fe staining of feldspars from late stage iron oxide flooding of the Hammer Zone.

2.7.2.6 Post Ore Oxide Phase (Phase VI)

2.7.2.6.1 Petrography and mineralogy (hand specimen, thin section, EPMA and XRD)

The post ore oxide phase post-dates the vein mineralization in the Hammer Zone and is characterized in hand specimen by extensive chlorite and quartz veining associated with hematite (Fig. 2.33A). Rutile, ilmenite and pyrite are found within the chlorite veins (Fig. 2.33B-D). The pyrite forms anhedral crystals present in large opaque masses alongside calcium rich oxide minerals like parasite and xenotime with a rutile or ilmenite matrix (Fig. 2.33C). Minor amounts of zircon, monazite and xenotime were found associated with the chlorite veins. All these minerals had small crystal sizes up to 20μm and euhedral to subhedral crystal forms (Fig. 2.33E, F). Quartz occurs as large, cm to mm scale drusy crystals in cm scale veins. All quartz veins from phase VI are barren, with no sulfides present.

The post ore oxide phase is also present around the edges of many phase II calcite veins as 'feathered', high relief carbonate crystals. The post ore oxide phase is high in Fe, with EPMA values peaking at up to 40 wt.%. With iron values this high, analyses suggest this mineral is likely siderite.

2.7.2.6.2 Microthermometry and Isotopic Analyses

The post 0xide ore phase quartz veining contains both primary and pseudosecondary inclusions. 8 FIA with two-phase aqueous inclusions were analyzed. All the FIA contain. The Th vary between 220.7°C and 165.0°C and the Tmi varies between -1.1°C and -4.7°C corresponding to equivalent weight percent NaCl salinities between 1.9wt.% and 7.4wt.% NaCl equiv.

Twelve post ore stage quartz samples were analyzed for oxygen isotopes. The results for $\delta^{18}O_{SMOW}$ values varied between 4.05‰ and 10.94‰ (Fig. 2.22B; Appendix 2).

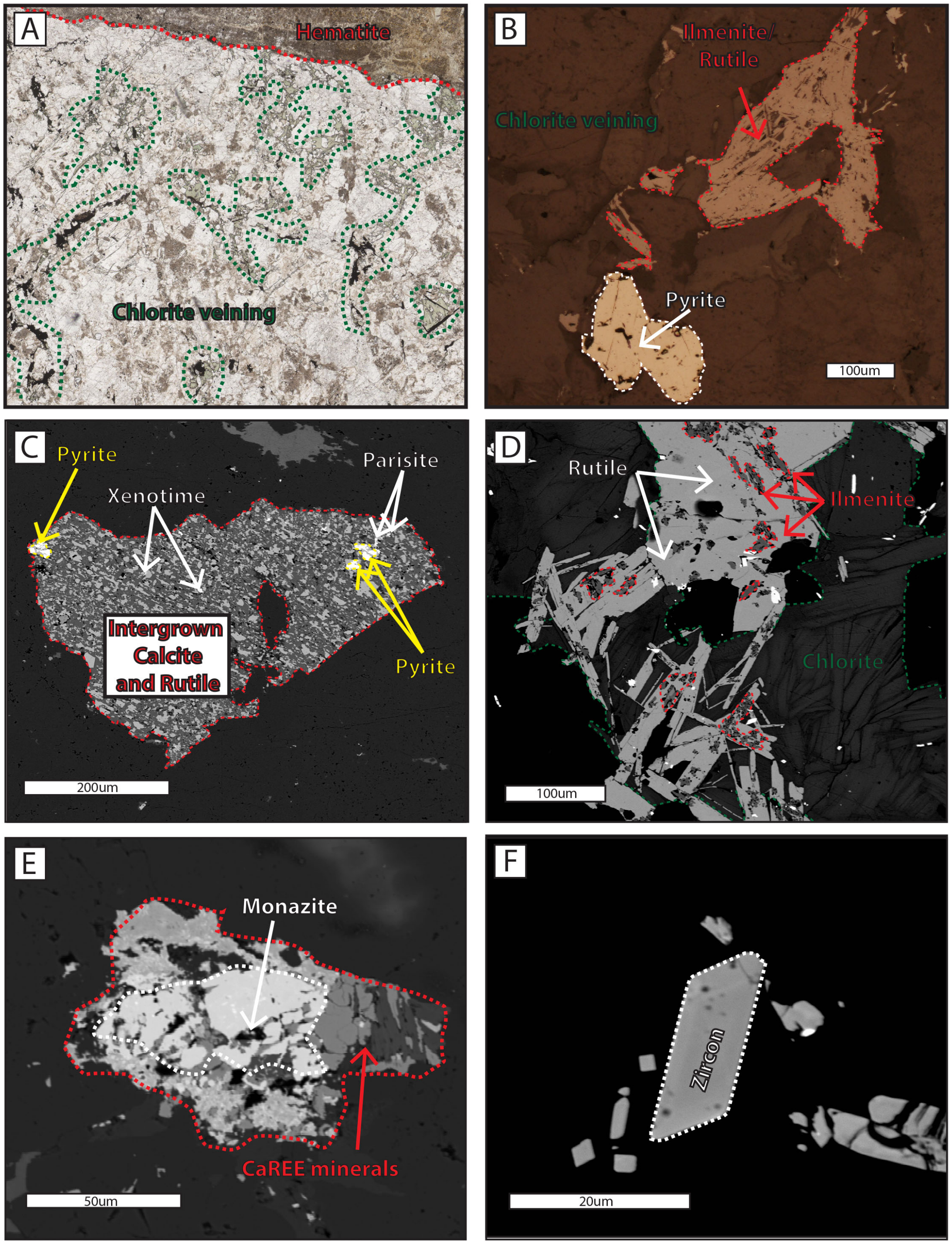

Figure 2.33 Plate showing various features associated with the post ore oxide stage. (A) Portion of a thin section scan showing the "dendritic" nature of the chlorite veining and close association with massive hematite veins. (B) Reflected light photomicrograph showing pyrite, ilmenite and rutile in a chlorite vein. (C) BSE image of an "agglomeration" of pyrite, xenotime, and parasite in a calcite and rutile matrix. (D) BSE image of acicular rutile and ilmenite in a chlorite vein. (E) BSE image of a monazite crystal surrounded by a variation in calcium and rare earth element bearing oxides. (F) BSE image of a zircon associated with chlorite veining.

2.8 Discussion

2.8.1 The Anvil Suite Granite

Monazite U-Pb ages for the Anvil Suite granite range between 109.3±1.2Ma and 103.9±1.5Ma (Pigage, 2004, Gordey, 2013). Zircons were highly discordant and did not yield useable age data. Monazite from the potassic alteration has been dated at 106.6±1.0Ma (Fig. 2.8) and as a minimum age for the Anvil Suite granite, this date fits with the ages published by Pigage et al. (2004) and Gordey (2013), for the Mid Cretaceous igneous suite (123-100Ma).

Geochemically, several plots have been used to classify the Anvil Suite granite (Fig. 2.6A, B; Fig. 2.7) as a reduced, ilmenite series, peraluminous, S-type, calc-alkaline intrusion. Therefore, the Anvil Suite granite is similar to the Mid- Cretaceous intrusions (115-100Ma) described by Mortensen et al., (2000) and Rasmussen, (2013).

The large quantities of biotite and K-feldspar (Fig. 2.5A) indicate the Anvil Batholith granite was potassically altered. However, there is no evidence from Figure 2.7 C, D that the most fluid mobile elements, Pb and Cs have been removed from the system. In contrast, a study on sericitic and potassic alteration of granitoids (Alderton et al., 1980) showed there was mobility of REE due to the breakdown of biotite. However as primary and secondary biotites are present in the Anvil Suite granite samples, alongside monazites, which are also rich in REE, it is possible that the REE mobility was limited and therefore, the major minor and trace element data from the Anvil Suite granite may still retain some information pertaining to petrogenesis of the intrusion.

Early studies of Australian granitoids (Flood and Shaw, 1975; Hine et al., 1978) suggested that many intrusions are reduced, and hypothesized that this is evidence of formation from a reduced sedimentary protolith. The geochemical data presented in Figure 2.6A and the large inherited cores in found in the zircons in this study support this. Analyses of ^{87}Sr/^{86}Sr on whole rock samples showed that the Anvil Suite granite has radiogenic ^{87}Sr/^{86}Sr values of 0.738 to 0.750 (Gordey, 2013). This is permissive of a sedimentary source rock; the higher ^{87}Sr/^{86}Sr values represent strontium that has gone through an earlier sedimentary cycle (Chappell and White, 1974; Kistler, 1974).

There are many similarities between the whole rock data of this study and the high K, calc-alkaline Anvil plutonic suite intrusions described in Rasmussen (2013). In particular, both studies document high Rb/Sr and low concentrations of Th, Nb, Ti, Yb and Y in these units. In her study, Rasmussen points out that these elements are at anomalously low levels when compared to other high-K, calc-alkaline suites in the Yukon. The high Rb/Sr ratios are due to the anomalously low levels of Sr in the Anvil Suite granite (below 250ppm) and indicate that the high levels of Rb result from potassic alteration. The low levels of all these trace elements are similar to those in low-Sr leucogranitic, low-temperature, minimum melt magmas (Kemp and Hawkesworth, 2003). Furthermore the low CaO/Na_2O and Fe_T+MgO+TiO_2 and high Al_2O_3/TiO_2, suggests the intrusion formed from a pelitic protolith (Rasmussen, 2013). A steeply dipping REE trend in a spider diagram is indicative of garnet in the protolith as garnet preferentially incorporates HREE, thus fluid derived from melting a source rock containing garnet, would be low in these elements (Fig. 2.7C, D).

2.8.2 Tectonic Setting of the Anvil Suite Granite

Four petrogenetic models for how the Cretaceous intrusions in the Selwyn Basin formed have been proposed on the basis of field observations, petrography and whole rock isotope geochemistry of many intrusive suites in the Selwyn Basin, including the Anvil Suite granite. The first model concentrates on the sub-parallel orientation of the intrusions to major strike slip faults. The transpressional structures forming along the fault could have caused thickening and following a change in plate movement, subsequent melting during decompression (Murphy et al., 1995; Gabrielse et al., 2006). However, whilst transpression and subsequent decompression may influence the intrusions close to the fault, it does not explain geochemically similar intrusions distal from the faults. Thus, Rasmussen, (2013) suggested that the transpressional regimes might have some control on the location of the Anvil Suite granite, rather than cause it. In the second model, Johnston, (2008) proposed a cryptic suture zone below the eastern margin of the Selwyn basin. This theory describes the Selwyn Basin as an accretionary prism between ribbon continent and North American platformal sediments from the Selwyn Basin and Kechika Trough (Rasmussen, 2013) formed during western dipping subduction. This leads to northeastern progradation of the subduction zone, explaining the production of younger plutonic suites to the east. However, some authors believe this theory does not fit with the stratigraphy of the Selwyn Basin (Rasmussen, 2013).

The third model revolves around the anatexis of over thickened crust. This requires the crust to be thickened to 50-70km about 30-40 million years prior to melting in order to have heat sufficient enough to allow for fluid absent melting of rock (Clemens, 2003; Bonin, 2004; Bea, 2012). In addition, the crust must be enriched in radiogenic heat producing elements, by about 50% compared to average crustal levels, in order to produce sufficient heat (Bea, 2012). Thus the most likely source for the granitic melt under these conditions would be a radiogenic, sedimentary or meta-sedimentary rock, most likely a shale or slate (Rasmussen, 2013). The less evolved, lower silica phases of the Early to mid-Cretaceous magmatism (Tay River suite) would have required the input of mantle-derived heat, which may have come later as manifested by lamprophyric dykes found locally near the Cassiar Batholith (Cooke and Goodwin, 1984; Ash et al., 2001; Rasmussen, 2013). The issue with this model is the fact there is very little evidence for the thickening of crust to 50km. The current depth to Moho is 30-35km (Clowes et al., 2005). Therefore, a simple model of anatexis of an overthickened crust may be too simplistic to form the extent and variety of igneous activity in the Western Selwyn Basin.

The final model invokes back arc collapse, exhumation and extension as the driving factors in formation of the Anvil Suite (Hart et al., 2004; 2005; Mair et al., 2006). This argument is based field observations that the Early to mid-Cretaceous intrusions were emplaced into greenschist to amphibolite facies, metamorphic basement (Murphy et al., 2001, 2006; Dusel-Bacon et al., 2006; Mair et al., 2006; Dilworth et al., 2007). The formation of the Early- to Mid- Cretaceous intrusions begins with metamorphism of the basement rocks during crustal thickening to about 60km in the Jurassic (Rasmussen, 2013). Following this, convective removal of the over-thickened lower lithosphere would have caused the extensive exhumation and magmatism (Mair et al., 2006). This environment would produce in situ, decompression related crustal melts from a metasedimentary source in the metamorphosed basement rocks (Hart et al., 2004). This theory derives from outcrops in the Yukon-Tanana Uplands plutonic suite, interpreted as being related to the Anvil Suite (Hart et al., 2004).

The models involving anatexis of overthickened crust, and back arc collapse, exhumation and extension have some similarities. In both models the protolith is a meta-sedimentary unit, with a relatively high concentration of radioactive elements. The REE data from this, and other studies, suggest that the source rock (Fig. 2.7C) resided below 60km in the Earths crust, before exhumation. Moving a sedimentary rock to these depths is possible through orogenic thickening of the crustal rocks, which in turn supplies heat for melting. Partial melting of a crustal source rock would give the igneous rock a crustal geochemical signature. This manifests itself as low concentrations of Ba, Ti, Nb and Ta with high concentrations of Pb (this study; Rasmussen, 2013). Finally, these models would suggest that the Anvil Suite granite formed in a post-collisional environment. The Anvil Suite granite plots in between the volcanic arc and syn-collisional fields of the tectonic discrimination plots (Pearce et al., 1984; Fig. 2.6A-D), which would appear to be at odds with the formational environment outlined above. However, it has been found that post-collisional, high K, calc-alkaline rocks can plot in this region and further into the volcanic arc field as a function of the composition of their source rocks (Robert and Clemens, 1993).

To conclude, the Anvil Suite granite has features of an ilmenite series, calc-alkaline, peraluminous, S-type granitoid, formed from low degrees of partial melt of a pelitic source rock most likely in a post-collisional setting. Initially the source rock of the Anvil Suite granite would formed garnet in a high pressure setting following crustal thickening, as indicated by the REE trends. With the Anvil Suite granite sharing characteristics with granites forming in post-collisional settings, it most likely formed from decompression melting associated after thickening. This theory fulfills the necessity of a deep crustal signature in the Anvil Suite granite (inherited from the source rock) alongside post-collisional characteristics (from the formational setting). The syn-collisional characteristic identified from the Pearce graphs (Fig. 2.6.2D-F) is inherited from the parental lithology. Following formation, the Anvil batholith has been potassically altered. This alteration occurred at 106.6±1.0 Ma and pre-dates the silver mineralization, which is the focus of this study.

2.8.3 Evolution of mineralization in the Hammer Zone

Calcite Veins (Phase II)

The calcite vein mineralization post-dates potassic alteration. Muscovite from argillic alteration associated with the Hammer Zone mineralization was dated to be 100.6±1.1Ma (Mortensen and Ballantyne, 1992). The sulfide assemblage found in the calcite veins includes major minerals sphalerite, pyrrhotite, galena, and arsenopyrite, and minor minerals, dyscrasite, pyragyrite, tetrahedrite, stephanite, acanthite and cobaltite. Many of the sulfides, in particular pyrrhotite, galena and sphalerite have a mottled texture, possibly due to dissolution. This may be due to the fact that later fluids, with different chemistries have utilized the same structures. The minor minerals, in particular dyscrasite (Ag_3Sb) and tetrahedrite ($(Cu,Fe)_{12}Sb_4S_{13}$) indicate low log fS_2 and log fO_2 (Lynch, 1989), suggesting the nature of sulfur species in the system to be H_2S or HS^- (Ohmoto and Rye, 1979). The occurrence of pyrrhotite also suggests a low oxygen fugacity (Fig. 2.34), the maximum log fO_2 being ~-42 (see below) (Mango et al., 2014).

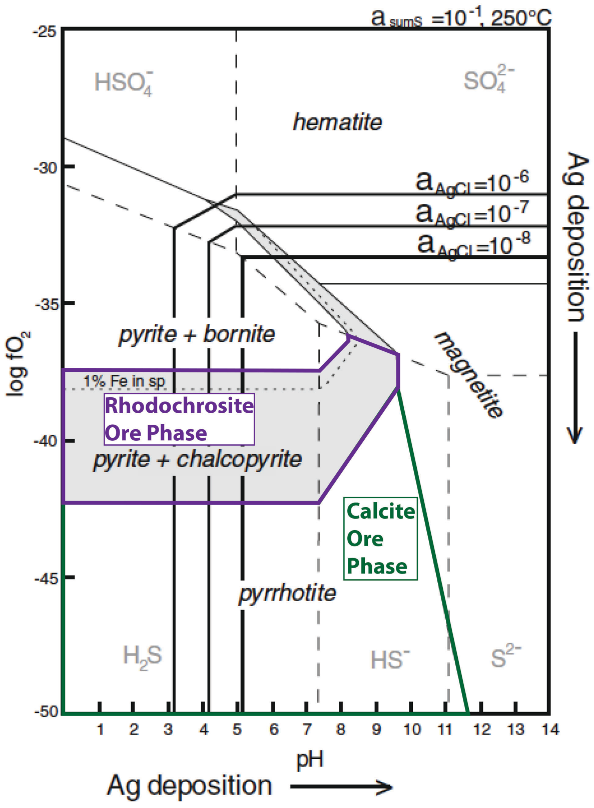

Figure 2.34. Graph showing log fO_2 versus pH; note the occurrence of pyrrhotite, pyrite and chalcopyrite. Labeled are the calcite and rhodochrosite paragenetic phases (adapted from Mango et al., 2014).

EPMA analyses found significant Fe and Mn concentrations in sphalerite. Laser ablation analysis detected lower amounts of trace elements. The chemistry of sphalerite is dependent on the crystallization temperature, metal source and the amount of sphalerite forming (Cook, 2009). Typically, epithermal sphalerite will have high levels of Mn and Fe (>1000ppm) and elevated levels of Ge, Ga and Sn (Cook, 2009). The LA-ICP-MS analyses show that this sphalerite has elevated concentrations of Ag, Cd, Co, Cu, Ga, In, Sb, and Se. Cd^{2+} and Co^{2+} can substitute directly for Zn^{2+} into the sphalerite lattice. This occurs due to the similarities between the trace elements and Zn in size and preferred tetrahedral coordination in the sphalerite crystal lattice (Rosso and Vaughan, 2006; Cook, 2009). The rest of the elements present, $Cu^{(+,\,2+)}$, Ga^{3+}, In^{3+} and Sb^{3+} substitute into sphalerite by coupled substitution. Here, two elements, usually Cu^{+} and another element, replace two Zn^{2+} ions or a Zn^{2+} and a Fe^{2+} ion (Johan, 1988; Cook, 2009). The concentration of Cu in sphalerite has been shown to increase with increasing temperature and decreasing sulfur fugacity at the time of sphalerite formation (Hutchison and Scott, 1981; Balabin and Sack, 2000; Hantelmann, 2013). The sphalerite from the calcite veins contains high Cu concentrations, thus the fugacity of sulfur during sphalerite deposition must have been low (Hutchison and Scott, 1981). Selenium in sphalerite replaces S due to similarities in charge. The occurrence of an elevated concentration of Se in sphalerite is more common in deposits formed at lower temperatures, and was found in a number of epithermal deposits (Neogene epithermal mineralization, SE Europe; Cook, 2009). A few studies show elevated silver in sphalerite up to 100ppm (e.g. Red Dog; Kelley at al., 2004; Cook, 2009) and in the Hammer Zone sphalerite, silver is present up to 500ppm. However, as Ag is rarely found in the crystal structure of sphalerite (Cook, 2009), this may suggest the sphalerite contains micro- or nano-inclusions of silver bearing minerals.

The presence of cobaltite in the Hammer Zone also suggests high concentrations of Co in the mineralizing fluids. The cobalt was introduced into this mineralizing system from two probable sources, a local mafic intrusion (Cook, 2009) or sedimentary rocks, in particular black shales. The Anvil Suite granite is intruded by intermediate-to-mafic ca. 99 Ma Tay River porphyry dykes. However geochemical analyses on samples from the Tay River suite (Gordey, 2013) found very low concentrations of Co and Ni in all Tay River samples and the field observations and age of these intrusions suggest they predate the Hammer Zone mineralization (100.6±1.1Ma; Mortensen and Ballantyne, 1992). However, Co and Ni, in particular Co, are found in large abundances in black shales (Large et al., 2011). The sedimentary package around the Anvil Batholith contains black shales, in the Earn Group, and some small Ni-Zn-PGE showings have been found on the contact of the Earn Group and the underlying Road River sedimentary sequence (Jefferson and Spirito, 2003; Wright et al., 2007). Therefore, the Hammer Zone mineralizing fluids could have elevated Co and Ni concentrations derived from the surrounding sedimentary country rock.

The LA-ICP-MS analyses of pyrrhotite returned different values for each of the two pyrrhotite samples studied. Pyrrhotite sample from thin section CP26 is from a vein that was used as a conduit by later Mn-rich fluids, interpreted to form the rhodochrosite phase (see below). The CP26 pyrrhotite sample displays overgrowths of late pyrite and fractures containing late galena, as has elevated levels of Ni, Co, Ag, Zn, Cu, Sb, Bi and Mo (listed in descending order of abundance; Fig 2.18), with higher concentrations of Co and Ni, in the 100s ppm range, and a low Co/Ni ratio. Pyrrhotite sample CP32 was from a pristine calcite vein, with no Mn-rich carbonate overgrowths or late galena or pyrite. Cobaltite was found in small inclusions in the pyrrhotite. The CP32 pyrrhotite sample had elevated levels of Sb, Cu, As, Co, Ni and Ag (listed in descending order of abundance Appendix 4). The low concentrations of Co and Ni in sphalerite in sample CP32 can be explained by these elements being preferentially partitioned into cobaltite.

The vein-forming calcite contains minor concentrations of Mn, Fe and Mg. The substitution of Mg, Fe and Mn into the calcite lattice is a function of temperature, rate of precipitation, salinity, Eh, f_{CO_2}, pH and concentrations of these elements in the formational fluids (Simmons et al., 2000), with temperature being the most important control. Overall, Mn is the most common minor element (Appendix 1). The calcite in this paragenetic stage has a chemical composition of $Ca_{0.63}Mn_{0.30}(Fe, Mg)_{0.07}$. The majority of work on elemental substitution in carbonates concentrates on high temperature (>400°C) or low temperature (<100°C) systems (Simmons et al., 2000). Nevertheless, using the phase equilibria that are available, the composition given above is indicative of formation at a low temperature, below the calcite-kutnahorite solvus (Peacor et al., 1987). Fluid inclusion assemblages from the calcite phase contained both two-phase (Lw+Vw) and single-phase (Vw) inclusions in the same FIA. All the two phase fluid inclusions studied had Th values between 215°C and 270°C, and equivalent NaCl salinities of 8.1wt.% and 9.9wt.%. The high salinities measured for fluid inclusions may suggest that metals were transported as chloride complexes to the site of mineralization (Seward, 1976; Wilkinson, 2013).

The occurrence of bladed textures in calcite suggests that boiling occurred during the formation of calcite veins (e.g. Simmons and Christenson, 1994). Boiling occurs in epithermal systems for one of two reasons: phase separation and gas exsolution of CO2, steam, CH_4 and/or H_2S or through heating of a solution close to calcite saturation resulting in phase separation (Simmons and Christenson, 1994; Simmons et al., 2000). The occurrence of two phase and single-phase fluid inclusions in a single FIA has been observed in one sample (Fig. 2.19), and demonstrates that boiling has occurred (Hedenquist and Henley, 1985).

The importance of boiling in the precipitation of silver minerals, and resultant effect on the isotopic composition on coeval carbonate minerals has been highlighted in the Keno Hill system, Yukon (Lynch, 1990). $\delta^{18}O$ values in quartz in the Keno Hill system have a wide range, which have been attributed to the fractionation between gaseous CO_2, and H_2O and liquid H_2O and CO_2. Fractionation of oxygen occurs primarily during boiling of H_2O and after boiling between the remaining liquid and CO_2 (Lynch, 1990). Escaping gaseous H_2O is enriched in ^{16}O whilst the remaining liquid H_2O is enriched in the heavier isotope (Craig et al., 1963; Truesdell et al., 1977). Whilst carbon dioxide is a volatile substance that partitions ^{18}O (Bottinga, 1968, Lynch, 1990), the isotopes of oxygen are not significantly fractionated between gaseous and aqueous CO_2 (Vogel et al., 1970; Lynch, 1990). CO_2 has a much greater influence on the isotopic composition of the fluid immediately after the boiling process ends. For boiling, the evolution of the system has been modeled (Lynch, 1990) from an end member of 100% fluid to almost 100% gas, and this model found that the oxygen isotopic composition of the remaining fluid after boiling could change by up to 14‰ (Truesdell, 1974; Lynch, 1990). The samples with lower $\delta^{18}O$ values formed as the system boiled to a larger degree thus depressing the $\delta^{18}O$ value of the remaining fluid. As the majority of CO_2 is lost at the onset of boiling (Lynch, 1990), the range (around 12‰) in $\delta^{18}O$ values could be a factor of samples forming throughout the boiling process.

Boiling may also explain some of the variation in the carbon isotope data observed in this study. The occurrence of pyrrhotite is proof of a low log fO_2. In a reducing environment, it is possible that methane was present, although it was not observed in the fluid inclusions. The fractionation of carbon isotopes between CO_2 and CH_4 can increase $\delta^{13}C$ values (Rye and Ohmoto, 1974; Lynch et al., 1990). However, small shifts in oxygen fugacity during the formation of calcite can shift the $\delta^{13}C$ values considerably. A shift in the fugacity of oxygen by 1‰ can affect the $\delta^{13}C$ values by up to 30‰ (Ohmoto, 1972). During a dynamic process, such as boiling, the fugacity of oxygen is affected by the loss of volatiles from the fluid such as H_2S (Drummond and Ohmoto, 1985).

Using various initial fluid compositions and calcite mineral isotopic compositions over a range of homogenization temperatures from the fluid inclusion studies, a possible initial fluid composition was estimated for the calcite (Fig. 2.35). This method found initial fluid compositions, before boiling, to be -6‰ and -7‰ for $\delta^{13}C_{fluid}$ and $\delta^{18}O_{fluid}$ values, respectively. The negative delta values calculated here indicate that the mineralizing fluids were derived from meteoric water. The oxygen and hydrogen isotopic composition of Cretaceous meteoric water is considered to be similar to today (δD =-170‰ and $\delta^{18}O$ =-21‰) (Bowman et al., 1985; Layne et al., 1991).

The initial $\delta^{13}C$ value of meteoric water is dependent on the composition of the dissolved CO_2. This dissolved CO_2 $\delta^{13}C$ value would have mirrored the atmospheric CO_2 value during the Cretaceous (Boutton, 1991). This value has been calculated to be between 0 and -5‰ (Ekart et al., 1999).

However, the isotopic composition of the meteoric water may have been altered by interaction with the sedimentary rocks hosting the Anvil Batholith, or the Batholith itself. Although there are no whole rock data for the sedimentary host rocks, some estimates can be made based on their lithologies. The Earn Group comprises black shales and the Tay Formation comprises organic carbon free limestones. Black shales are known to have very negative $\delta^{13}C$ values due to the high levels of organic carbon present, possibly as low as -30‰ (Faure, 1986) and $\delta^{18}O$ values that mirror the isotopic composition of sea water at that time (Veizer et al., 1999) i.e. values between 20‰ and 30‰ (Sharp, 2007). Some unpublished work on a few samples of the Mississippian Tay Formation (Pryer pers. comm.) found the $\delta^{13}C$ value to be between -0.5 and -2‰ and

$\delta^{18}O$ values to fall between 16‰ and 20‰, similar to values of other samples from the same time frame (Sharp, 2007). Interaction of the meteoric fluids with the host-rocks would shift their oxygen isotopic values to higher values and could also explain the negative $\delta^{13}C$ values. Host rock interaction is supported by the Co and Ni concentrations in sphalerite and pyrrhotite and may also explain the reducing fluid conditions indicated by the mineralogy. Interaction with the Anvil Batholith will also have altered the O isotopic composition of the fluids. The Anvil Suite granite has been found to have an oxygen isotopic composition around 14‰ (Rasmussen, 2013). There are no whole rock carbon isotopic data for the Anvil Suite granite (possibly due to the low levels of C bearing minerals present), suggesting that water rock interaction with the granite is unlikely to have altered the C isotopic composition.

Meteoric water tends to have low salinity (<1 wt.% NaCl in most cases). Studies carried out on the increase of salinity in meteoric water during boiling found that over 100°C, boiling was responsible for an increase in salinity of around 3wt.% NaCl (Canet et al., 2011). It is unlikely therefore, that boiling alone can produce the 10wt.% NaCl that formed the Hammer Zone. There is no record of halides in the host units.

Previous studies have noted an increase in salinity associated with Ag mineralization in epithermal veins and have suggested this is due to an influx of a magmatic fluid (Wilkinson, 2013). In this study we found no direct chemical or isotopic evidence of the input of a magmatic hydrothermal fluid. However, the strontium isotope values of 0.735 to 0.740 in the veins are similar to the $^{87}Sr/^{86}Sr$ values of 0.730-0.735 recorded for the Anvil Suite granite (Gordey, 2013) and suggest that Sr originated in the granite. Furthermore the isotopic composition of magmatic carbon varies depending on source. The most common figure for magmatic carbon isotopic composition is -5.5‰ and -3‰ (Taylor, 1987). However magmatic carbon isotopic values have been found to range between of +5‰ to -16‰ in various instances (Mattey et al., 1984; Sharp 2007). With such a large range in $\delta^{13}C$ values for magmatic carbon it is entirely possible this reservoir influenced the fluid responsible for forming the calcite ($\delta^{13}C$ value = -7‰)

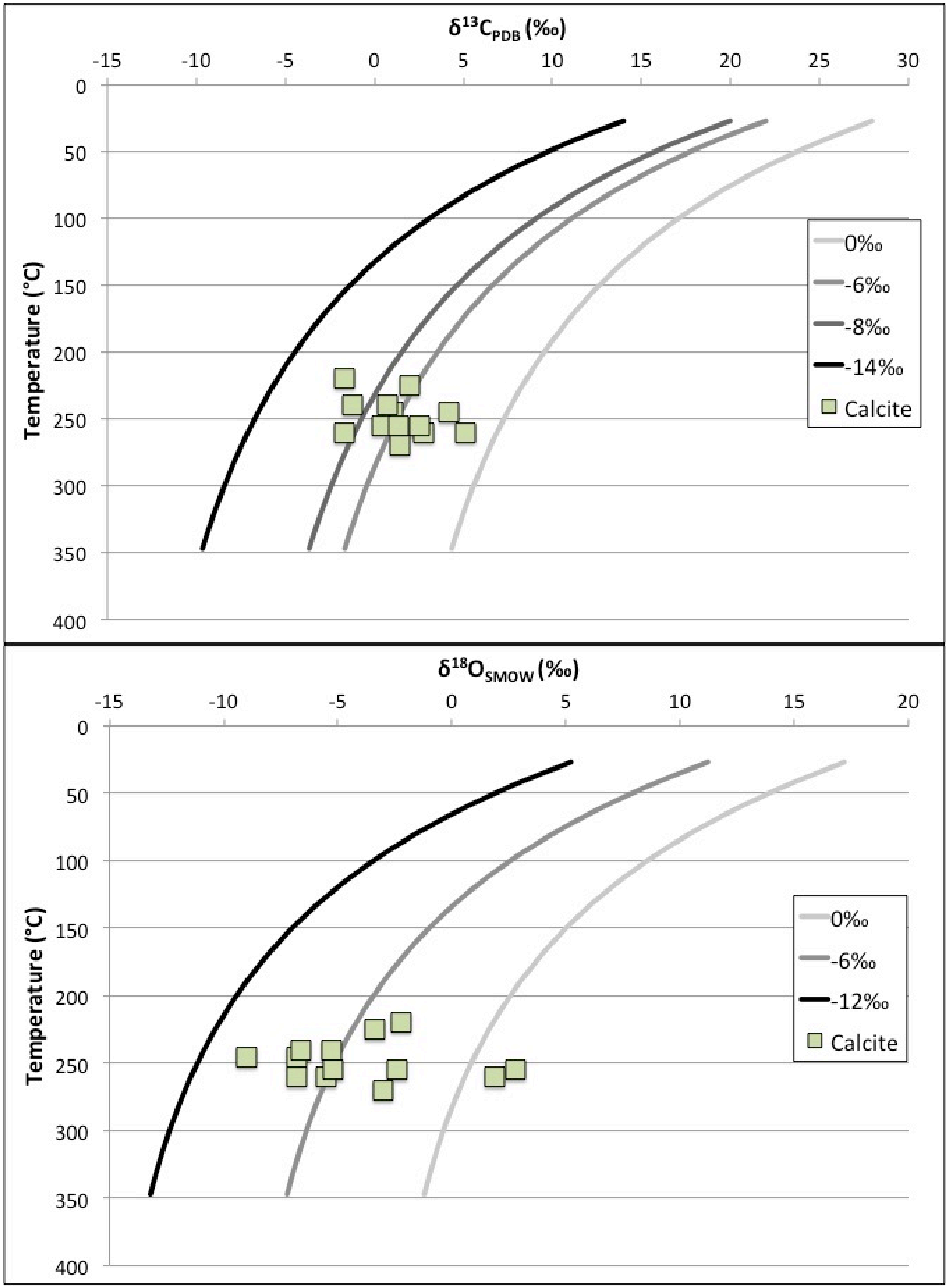

Figure 2.35. Graphs showing various initial fluid compositions for calcite and the spread of temperatures from fluid inclusion analysis alongside the measured carbon (A) and oxygen (B) isotopic compositions of calcite. These graphs found the initial δ^{13}*C and δ*^{18}*O values to be -7‰ and -6‰, respectively.*

Quartz Veins (Phase III)

This sulfide-poor phase was deposited between two sulfide-rich carbonate veining phases. There are minor sulphides present in the quartz phase: arsenic rich pyrite, arsenopyrite, chalcopyrite, pyrite and sphalerite. The sulfides from phase III do not display any mottling, unlike the calcite phase. The presence of pyrite, with the absence of pyrrhotite suggests an evolution in the system to more oxidizing fluids and a higher fugacity of sulfur (Lynch, 1989; Mango et al., 2014).

The homogenization temperatures for FIA in phase III quartz are similar to the upper values of the phase II calcite (270°C to 290°C), but the salinities in this stage drop to between 2wt.% and 8wt.%. There is no evidence to suggest that boiling occurred at this stage of the paragenesis and the lower fluid inclusion salinities suggest an increased influence of meteoric water. This is supported by the oxygen isotopic composition. The $\delta^{18}O$ values range from 2‰ to 10‰ and assuming a temperature of deposition at 275°C, the initial fluid forming quartz was found to have $\delta^{18}O$ values between -6.0‰ and -2.0‰, with two outliers at 2‰ and 4‰ (Fig 2.36, fractionation factor via Clayton et al., 1972). These data can be explained by interaction of the meteoric waters with the host sediments and/or the Anvil Suite granite.

Silver-rich rhodochrosite veins (Phase IV)

The second carbonate-veining phase, rhodochrosite, succeeds the phase III quartz veins. Analyses of the gangue mineral rhodochrosite, showed it has two distinct end member compositions: kutnahorite ($CaMn(CO_3)_2$ and rhodochrosite *sensu stricto* ($MnCO_3$). Although there is little other variation in the major element geochemistry, there are variations in the carbonate textures, which range from colloform to massive, euhedral, crystal growth forms. All textures suggest that the minerals formed in open space.

The rhodochrosite veins contain up to 30% by volume sulphides such as: sphalerite, galena, freibergite, arsenopyrite, chalcopyrite and pyrite. The sulfides from the rhodochrosite phase do not display mottled or disequilibrium textures. This sulfide assemblage, in particular the presence of pyrite and freibergite, suggest this stage of vein growth occurred in a more oxidizing environment than the calcite mineralization stage (Lynch, 1989; Mango et al., 2014). In a study by Lynch (1989) on Keno Hill, there was a spatial progression from a S-poor environment where tetrahedrite was precipitated, to a S-rich environment depositing freibergite (Lynch, 1990; Hantelmann, 2013). The Hammer Zone shows a similar progression through time.

Sphalerite in the rhodochrosite phase has higher Fe and Mn concentrations than those of the calcite mineralization phase. The high levels of Mn in sphalerite are indicative of precipitation from a higher temperature fluid (Cook, 2009). This is supported by the fluid inclusion data (discussed below). EPMA analysis of galena found Sb, Bi and Ag concentrations above the detection limits. As the wt.% of Ag in these galenas is below the wt.% of the sum of Bi and Sb, for any given analysis, it can be inferred that the silver exists within the lattice of galena, not as sub-micron scale inclusions of silver sulfosalts (George et al., 2015). The Ag concentrations in galena are high enough that Ag cannot substitute in the galena lattice via simple $2Ag^{+}$ for Pb^{2+} substitution. Instead it will substitute into a structurally unfavorable, interstitial position (George et al., 2015), which must occur via coupled substitution, $Ag^{+} + (Bi, Sb)^{3+} = 2Pb^{2+}$ (Chutas et al., 2008; Renock and Becker, 2011; George et al., 2015). In the absence of Bi and Sb, it has been hypothesized that other trivalent ions could aid the substitution in the same way (George et al., 2015). Galena from samples CP-26 and C23 have variable concentrations of Bi and Sb, respectively. This could be the result of galena having an incomplete, but substantial, solid solution between galena and the two end member Bi-bearing minerals, matildite ($AgBiS_2$) and miargyrite ($AgSbS_2$) below 420°C (Lueth et al., 2000; Ghosal and Sack, 1999; George et al., 2015). If so, this would suggest that this process could occur to much lower temperatures (a minimum range of 270°C to 290°C as suggested from the fluid inclusions).

LA-ICP-MS analyses were performed on sphalerite and pyrite from the rhodochrosite veins. In both paragenetic phases, the elements present were similar (Ag, Cd, Co, Cu, Ga, In, Ni and Se). However, the concentrations of each element varied between the phases. Cu and Sb concentrations were lower in sphalerite from the rhodochrosite veins, likely due to the presence of chalcopyrite, freibergite and arsenopyrite in the ore assemblage. Increased Cu content in epithermal systems is usually an indicator of a high temperature of formation (Hutchison and Scott, 1981). The pyrite from the rhodochrosite veins had low abundances of trace elements. The most abundant elements present were Co and Ni, but even these were only present at concentrations around 50ppm. This may suggest that either source of fluids or the fluid pathway has changed between the calcite ore stage and the rhodochrosite veins. The data indicate that the fluids associated with phase IV may have had less interaction with the black shales of the Earn Group, possibly resulting in a more oxidized fluid.

Fluid inclusions studied from rhodochrosite returned homogenization temperatures similar to the quartz ore stage, between 270°C and 290°C, with an average around 275°C. However the equivalent NaCl salinities are much higher, ranging from 6wt.% to 13wt.%. The fluid inclusions assemblages found in rhodochrosite contain two-phase inclusions and, as with the quartz ore stage, there is no textural or geochemical evidence to suggest that boiling occurred at this stage of the paragenesis. As in the calcite stage there appears to be a relationship between the presence of Ag bearing minerals and higher chlorinity fluids. The relationship between chlorine content of fluids and metal occurrence was established through LA-ICP-MS analysis of fluid inclusions with variable salinities (Wilkinson, 2013). Fluid inclusions with higher salinities contained a higher metal concentration. In this paragenetic stage, the much higher salinities found in fluid inclusions cannot be derived from meteoric water (0wt.% NaCl). They may be the result of a pulse of more saline fluids, most likely derived from a magmatic source or the sedimentary rock.

Stable isotope analyses have a range in $\delta^{18}O$ values from 4.0‰ to 9.0‰ but a narrow range in $\delta^{13}C$ values between -8.0‰ and -6.0‰, which correspond to $\delta^{13}C_{fluid}$ and $\delta^{18}O_{fluid}$ values between -2.0‰ and -0.0‰, and -5.0‰ and 0.0‰, respectively (at 275°C). The $\delta^{18}O_{fluid}$ values of -5.0 to 0.0‰ suggest the dominant hydrothermal fluid is derived from meteoric water (initial value around -21‰). This fluid has subsequently reacted with the Anvil Suite granite, or the host sedimentary rocks, both of which have positive $\delta^{18}O$ values. However, the low Co and Ni concentrations suggest that interaction with the Earn Group waned in this paragenetic stage and interaction with the Anvil Suite granite is more likely. The $\delta^{13}C$ values between 0.0 and -2.0‰ are similar to the Tay Formation limestones (Pryer, pers. Comm.) but are too high to be related to the black shale lithologies in the sedimentary package, which are more likely to have $\delta^{13}C$ values around -20‰ to -30‰. Magmatic carbon has an isotopic composition around -5‰ to -3‰ (Taylor, 1987), with some magmatic CO_2 values reaching +1‰ (Sharp, 2007). However, as with the calcite stage, the values of the reservoirs are too close to be able to distinguish with any real confidence and the lack of CO_2 in fluid inclusions makes it hard to say, definitively that the second source of carbon is magmatic. The $^{87}Sr/^{86}Sr$ values for the rhodochrosite are slightly higher than those found in the calcite and support a model whereby the rhodochrosite mineralizing fluids have interacted strongly with the Anvil Suite granite. The $\delta^{34}S$ values for galena and sphalerite from the rhodochrosite phase are c. 10‰, and fall within the range of the Anvil Batholith (6 to 10‰; Rasmussen, 2013) and evolved intrusive rocks in the Selwyn Basin (1 to 14‰; Rasmussen, 2013).

Post-ore oxide stage (Phase V)

The end of the silver rich mineralization is marked by another phase of quartz veining (phase V). These quartz veins are associated with a large amount of hematite staining alongside small but extensive chlorite ± monazite veins.

Fluid inclusion studies in quartz from this paragenetic stage record a drop in temperature with homogenization temperature between 170°C and 220°C and equivalent NaCl salinities ranging between 2wt.% and 6wt.%. These lower salinities suggest an increasing role for meteoric water, which is confirmed by the $\delta^{18}O_{fluid}$ values (between -9.0‰ and -2.0‰). However, salinity values above 3.5wt.% indicate there is still salt in the system, possibly from the ore stage.

Fluids such as this one are not uncommon in epithermal systems as late veins indicative of a collapse of the system, for instance, a late oxide rich episode is observed at Keno Hill (Lynch, 1990; Hantelmann, 2013).

2.8.4 Summary of the Genesis of the veins in the Hammer Zone

Age of Mineralization

$^{40}Ar/^{39}Ar$ dates from muscovites in alteration zones adjacent to the mineralization gave an average age of 100.6±1.1Ma (Mortensen and Ballantyne, 1992). This is ca. 3.8 million years younger than the 106.6±1.0Ma age of the potassic alteration of the Anvil Suite granite. The cooling rates of granites have been extensively studied (Hodges, 2005). Hodges suggests that medium to large igneous bodies take between 10^3 to 10^5 years to crystallize and cool. Therefore, the Anvil Batholith would have a cooling time less than 1000 years. Even when using the cooling time of a large batholith, the apparent >3.8 million year difference in the ages of the potassic alteration associated with Anvil Suite granite and the mineralization related to the Hammer Zone alteration suggest it is unlikely that the Anvil Suite granite is the heat source for the mineralization, and therefore, another causal heat source must be present. The ca. 99Ma Tay River Suite dykes are a potential heat source for the Hammer Zone mineralization. However, these have been observed to crosscut the Hammer Zone mineralization in the field. Therefore, the possibility exists that the Tay River Suite is the intermediate equivalent of a deeper, regional heat source or another, younger igneous body associated with the Anvil Batholith. Further work is needed to ascertain what heat source drives the mineralization of the Hammer Zone. Whether it is related to the Tay River Suite, a younger lithology in the Anvil Batholith, or an unknown regional intrusion is yet to be documented.

Evolution of the Hammer Zone

The Hammer Zone is a vein hosted Ag±Pb-Zn deposit. The initial stage of mineralization occurs as fracture filling calcite veins hosting various sulphides. These formed from evolved meteoric water, having previously interacted with the sedimentary rock package hosting the Anvil Suite granite. The resultant fluid had more positive $\delta^{18}O$ values, higher salinity and thus a higher metal content. It is not possible to identify the sedimentary rock or a magmatic fluid as the sole source of the total amount of salinity and metals, however some metals, including Co and Ni, were most likely obtained from the sedimentary rocks. The calcite veins were deposited via boiling, which resulted in a spread of data in a plot of $\delta^{18}O$ values against $\delta^{13}C$ values, and the coexistence of two phase and single-phase fluid inclusions. These veins were deposited from a reduced fluid, with log fO_2 values below -42 (Fig. 2.34). The majority of isotopic and chemical evidence points to interaction between Co and Ni rich, reducing, sedimentary rocks and meteoric water before depositing calcite and sulphides via a pH increase due to a release of acidic volatiles (CO_2) during boiling. In contrast, the source of the silver and salinity is more difficult to ascertain. With no halides present, and sea water having salinities of 3.5wt.%, there needs to be another source of salinity. The most likely source of this additional salinity, and associated metals, is a magmatic fluid. Very small amounts of highly saline fluid can supply metals for a whole deposit (Wilkinson, 2013), therefore the lower sulphide volume in the calcite vein phase can be explained by a small pulse of magmatic fluid.

The calcite phase shows characteristics of forming in conditions similar to low sulfidation epithermal deposits. These characteristics include a carbonate gangue mineral (Sillitoe and Hedenquist, 2003), reduced fluids resulting in the dominant sulfur species being H_2S, meteoric water as the initial source fluid (Corbett and Leach, 1998) and finally the mineralogy/mineral chemistry, with pyrrhotite and tetrahedrite present and Se common.

The subsequent quartz phase (III) represents a major change in fluid chemistry. The sulphide assemblage contains pyrite and chalcopyrite suggesting formation in a system with higher sulfur and oxygen fugacities, between log fo_2 values of -42 and -37 (Fig. 2.34). The quartz phase formed due to mixing between meteoric water and a more saline fluid, in a continuum with the fluids that subsequently gave rise to the rhodochrosite phase. The quartz and rhodochrosite veining phases have higher temperatures, higher salinities and are more metalliferous than those of the calcite phase. The rhodochrosite veins contain the majority of the silver in the Hammer Zone, in the form of freibergite. The rhodochrosite phase is formed from a fluid with an average temperature of 275°C and shares several characteristics with the quartz ore stage; the more oxidising conditions, the Cu and As rich mineralizing fluids, the higher temperature of initial fluids and decreased concentrations of Co and Ni. These factors, along with the lack of variation in the isotopic compositions and the different homogenization temperature vs salinity trends suggest different sources of fluids and depositional mechanisms between the calcite and, quartz and rhodochrosite phases. The quartz and rhodochrosite phases appear to be linked due to the continuation of fluid inclusion results between each of these phases (Fig. 2.36 below). In Figure 2.36 a mixing trend between two end members is outlined. The end members are: 1) meteoric water and 2) the source of salinity and metals. This mixing between meteoric water, and a higher salinity fluid most likely a magmatic fluid precipitated the Ag. The decreased concentrations of Co and Ni suggest the Earn Group sedimentary rocks had less interaction with the fluids forming the quartz and rhodochrosite phases. The rhodochrosite phase shows more characteristics of intermediate or high sulfidation, with a high fugacity of sulfur resulting in the deposition of pyrite and freibergite.

Other silver deposits in the Yukon and exploration strategy

The main historic silver production in the Yukon came from the Keno Hill hydrothermal vein system. The veins comprise quartz and feldspar gangue minerals alongside silver, lead and zinc hosted by galena, sphalerite and a host of silver bearing minerals, primarily silver bearing galena and tetrahedrite (Lynch, 1989; Hantelmann, 2013). Regionally, the Keno Hill District includes a suite of felsic to intermediate calc-alkaline and alkaline intrusions interpreted to be part of the Tombstone-Tungsten Belt (TTB). The TTB is split in three periods of igneous activity forming during the Late Cretaceous, between 97 and 90Ma. These three igneous suites range from metaluminous and oxidised (Tombstone intrusions, which are 92 to 90Ma in age) in the northwest to reduced and peraluminous in the southwest (Tungsten intrusions, which are 97 to 94Ma in age) with the Mayo Plutonic suite sandwiched between (95 to 92Ma in age) (Hart et al., 2004; Hantelmann, 2013). The most prominent intrusion in the Keno Hill district is the Mayo Lake Batholith, which is considered to be part of the Mayo Plutonic Suite of the TTB (Murphy and Bevier, 1997; Hart et al., 2004; Hantelmann, 2013). The primary lithology hosting the Keno Hill mineralization is the Mississippian Keno Hill quartzite, which is interbedded with phyllitic and graphitic schist and localized limestone (Hantelmann, 2013). The age of Keno Hill mineralization slightly postdates the igneous activity in this region at 87±3Ma (Sinclair et al., 1980). The Hammer Zone, at 100.6±1.1Ma, is older than the Keno Hill mineralization, however both sites have a ~3-5 million year delay between the spatially associated intrusions and the mineralization. Whilst the mineralogy of the Hammer Zone and Keno Hill vary somewhat, both systems change from more reducing to more oxidising fluids, (Lynch, 1989). In addition, both systems have evidence for early boiling followed by mineral precipitation caused by mixing. Stable isotope studies in both systems found meteoric water to be the dominant fluid, with a magmatic pulse supplying the metals (Hantelmann, 2013). Finally, in both systems, the end of mineralization is marked by an influx of meteoric water (Lynch, 1990)

The Keno Hill system and the Hammer Zone vary considerably in size. The Keno Hill system comprises many single veins over an area of about 80km^3 (Hantelmann, 2013), whereas the Hammer Zone comprises three veins over a smaller area of 5km^3 (Dumala, 2013). The majority of silver is hosted in galena and tetrahedrite end member at Keno Hill, whereas the silver in the Hammer Zone is hosted by freibergite. The igneous bodies that are spatially associated with the mineralization in the Hammer Zone and Keno Hill (Anvil Suite granite and Mayo Lake pluton, respectively) have different geochemistry. At the Hammer Zone the host rock is a peraluminous, reduced, S-type, biotite> hornblende, calc-alkaline granite. However, the Mayo plutonic suite, to which the Mayo Lake pluton belongs has been classified as a moderately reduced to weakly oxidized, hornblende > biotite, quartz monzonite or monzodiorite to biotite > hornblende, monzogranite to granodiorite (Rasmussen, 2013).

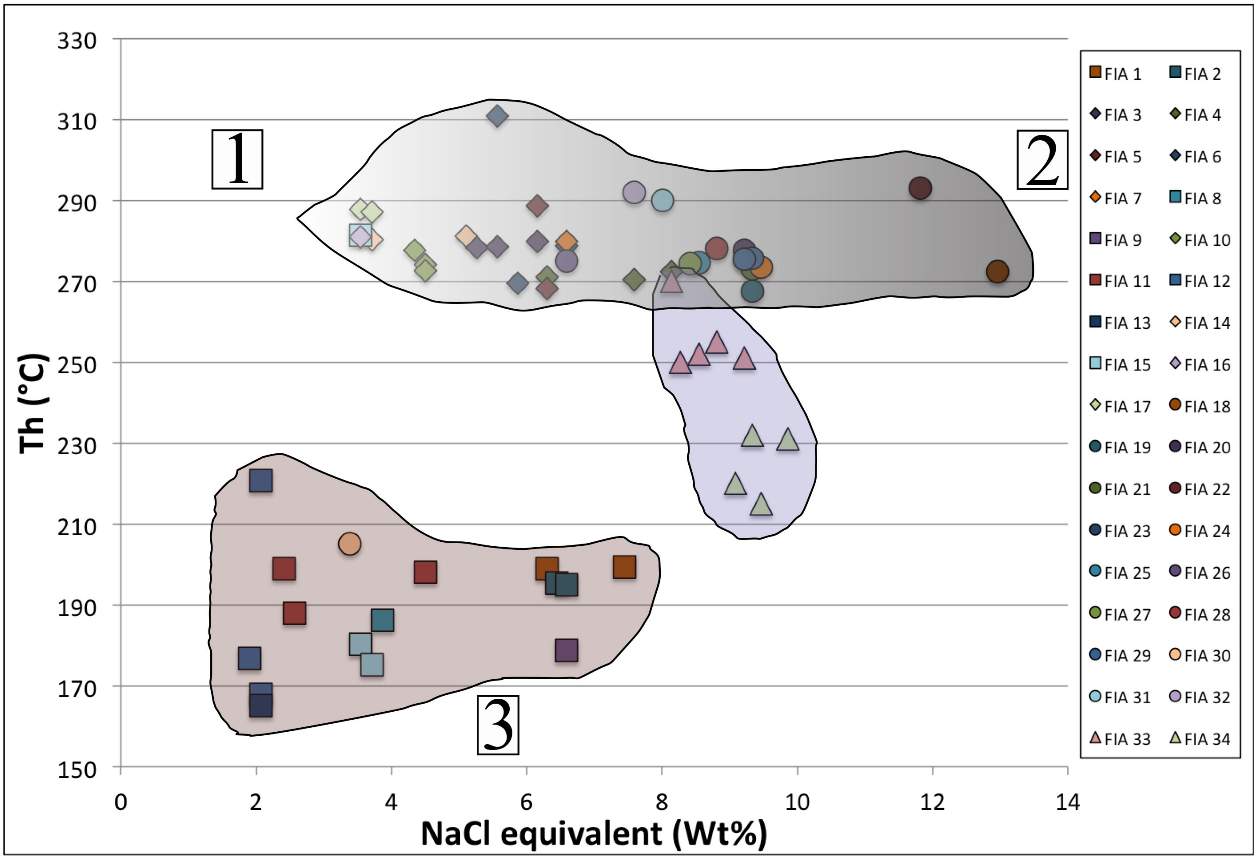

Figure 2.36 shows all fluid inclusion data split into groups based upon potential source. 1 is meteoric fluid responsible for quartz and rhodochrosite deposition, 2 is a saline fluid of unknown origin, potentially magmatic, 3 is the late stage meteoric fluid, which is indicative of the system collapsing.

2.8.5 Genetic Model

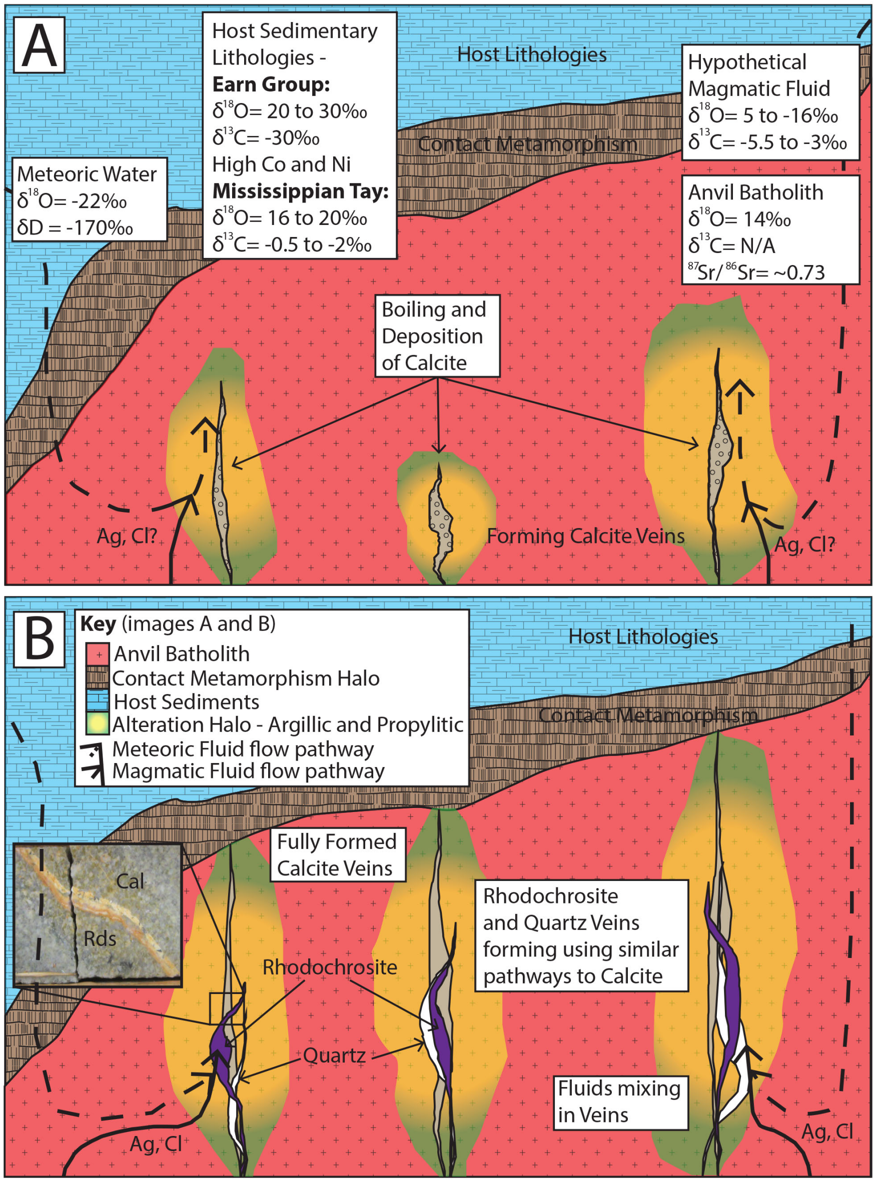

Figure 2.37 this genetic model shows the progression from calcite mineralization phase (A) through quartz and rhodochrosite phases (B). Figure 'A' shows the deposition of calcite veins due to boiling. The dashed arrows represent the meteoric fluids, in this instance, meteoric water flows through the sediments before deposition. Figure 'B' shows the deposition of quartz and rhodochrosite veins. In this figure there are two potential fluids, the uniform arrow depicting the pathway of the magmatic fluid and the dashed arrow the pathway of the meteoric water. The mixing of these two fluids in the veins may have caused deposition. The major change between figure A and B is the interaction between meteoric water and the sedimentary rock. In 'A' this interaction is far more prevalent than 'B'. Another difference is the method of deposition, from boiling in 'A' to mixing in 'B'. Around the vein assemblages in each image is an alteration halo. Listed in Figure 'A' are the potential isotopic sources and their compositions.

Chapter 3 - Conclusions and suggestions for future work.

Mineral chemistry, fluid inclusions and stable isotopes suggest the Hammer Zone mineralization formed during two separate fluid pulses, each with its own distinct chemistry, source and method of deposition. The first pulse of fluid was responsible for the calcite phase and was dominated by meteoric water, which subsequently interacted with the local sediments. This resulted in a reducing fluid based on sphalerite chemistry, fluid inclusions and C, O isotopes. The majority of sulphides present in the calcite phase were representative of low $\log fS_2$ (e.g. dyscrasite Ag_3Sb) or low $\log fO_2$ (e.g. pyrrhotite ($Fe_{(1-x)}S$) which supports the hypothesis of a reducing fluid. The silver in the calcite phase is hosted primarily in a suite of silver sulfosalts; dyscrasite, pyragyrite, stephanite and acanthite. The method of deposition was most likely boiling as indicated by single- and two-phase fluid inclusions occurring in the same fluid inclusion assemblage, as well as a spread in the C and O isotope data. Fluid inclusion data suggests the temperature of mineralization for this stage was between 215°C and 275°C, with an average around 250°C (Fig. 2.36).

The second pulse of fluid is responsible for the quartz and rhodochrosite phases. These formed due to mixing of meteoric water and a higher salinity, possibly magmatic fluid, based on fluid inclusion data and C, O, S and Sr isotopes. A decrease in the concentrations of Co and Ni suggest the ore forming fluids had less interaction with the Earn Group sediments. The minerals forming during these paragenetic stages are representative of higher $\log fS_2$ (e.g. pyrite) and higher $\log fO_2$ (e.g. chalcopyrite) supporting an oxidised fluid (Fig. 2.34). Whilst no silver bearing minerals were deposited during the quartz phase, the rhodochrosite phase contains the most silver of any paragenetic phase. The silver is found hosted primarily by freibergite, but also as minor amounts in galena. The fluid inclusion data shows quartz and rhodochrosite formed over a narrow temperature range, 270°C to 290°C, with an average of 275°C, and a range in salinities from 2wt.% to 12wt.%. This spread of data is interpreted as the two minerals forming due to mixing of a lower salinity fluid (meteoric water) with a higher salinity fluid (magmatic) (numbers 1 and 2, respectively, in Figure 2.36). This mixing is interpreted to be the cause of sulphide deposition in the quartz and rhodochrosite phases.

Whilst no unequivocal data point to a definite source of metals for these two stages, other information was used to try and constrain a source, namely isotopic data and sulphide chemistry. Isotopic data and sulphide chemistry showed there were three main influences on fluid chemistry, meteoric water, sedimentary rocks and a magmatic fluid. They also showed that the proportions of these different fluids and the pathway of these fluids changed. Despite this, the source of precious metals (e.g. Ag) and salinity remains the same in both ore stages, a pulse of magmatic fluid. However the source of salinity is decided based on power of deduction, therefore future work on chlorine isotopes could prove this conclusion.

Although no dating was performed on alteration minerals as part of this study, previous publications have dated the alteration assemblages around the Hammer Zone at 100.6±1.1Ma (Mortensen and Ballantyne, 1992). This age postdates the age of potassic alteration of the Anvil Suite granite by at least 3.8 million years, a gap too large to be able to claim the Anvil Suite granite as the heat source from the Hammer Zone mineralization. Likewise, Wilkinson (2013) proved that a small amount of magmatic fluid was sufficient to mineralize an entire deposit; meaning the Anvil Batholith is not required to be the source of metals. Therefore, there must be a cryptic heat source somewhere either regionally or locally. Further work should be performed to locate this heat source and classify it for future exploration.

There are several areas of this study where additional work would aid in further classifying the Hammer Zone mineralization and its relationship to the surrounding lithologies. As mentioned above, the Anvil Batholith requires further investigation, namely are there any portions of the batholith that relate chronologically with the Hammer Zone. This should be carried out in a number of ways; geochemical analysis of all the different textures and mineralogies found in the Anvil Batholith and exploration of further mid and Early Cretaceous Batholiths for epithermal deposits, including a potential parent igneous body for the Tay River Suite. Comprehensive dating of the phases of the Anvil Batholith and the Hammer Zone would give good insight into the relationship between these systems. However, unless zircons without inherited cores can be found or another method of dating is used, future studies will run into the same problems as this one vis-à-vis getting accurate age determinations.

Additional work on calcite fluid inclusions would be useful for a more complete determination of the geochemistry of the fluids forming this paragenetic stage. For the most part, the samples studied here were two opaque to find any fluid inclusions. This study managed to find two fluid inclusion assemblages in one calcite sample of five studied. Whilst these FIA helped define the deposition mechanics of the calcite phase, further exploration and measurements of fluid inclusions would add to the credence of opinions formed in this study. Similarly further sampling of sulfides for S isotopes should be carried out. Only two samples of galena and sphalerite were studied for sulfur isotopes, increasing the sample size would allow for better, more defensible conclusions to be drawn.

Chapter 4 - References

Alderton, D.H.M., Pearce, J.A. and Potts, P.J., 1980. Rare earth element mobility during granite alteration: evidence from southwest England. Earth and Planetary Science Letters, 49(1), pp.149-165.

Anderson, R.G., 1988. An overview of some Mesozoic and Tertiary plutonic suites and their associated mineralization in the northern Canadian Cordillera. Recent advances in the geology of granite-related mineral deposits, Can Inst Min Metall Spec Paper, 39, pp.96-113.

Armstrong, R.L., 1988. Mesozoic and early Cenozoic magmatic evolution of the Canadian Cordillera. Geological Society of America Special Papers, 218, pp.55-92.

Arribas Jr, A., 1995. Characteristics of high-sulfidation epithermal deposits, and their relation to magmatic fluid. Mineralogical Association of Canada Short Course, 23, pp.419-454.

Ash, C.H., MacDonald, R.W. and Reynolds, P.R., 2001. *Relationship between ophiolites and gold-quartz veins in the North American Cordillera*. British Columbia, Ministry of Energy and Mines.

Balabin, A.I. and Sack, R.O., 2000. Thermodynamics of (Zn, Fe) S sphalerite. A CVM approach with large basis clusters. *Mineralogical Magazine*, *64*(5), pp.923-943.

Bea, F., 2012. The sources of energy for crustal melting and the geochemistry of heat-producing elements. *Lithos*, *153*, pp.278-291.

Betz, J.E., 1977. Report on the maxmin II EM survey, Raz Grid; report for Welcome North Mines Ltd.; assessment report #090266.

Bodnar, R.J., 1992, Revised equation and table for freezing point depressions of H_2O-salt fluid inclusions. In Fourth Biennial Pan-American Conference on Research on Fluid Inclusions, Lake Arrowhead, CA, Program and Abstracts (Vol. 14, p. 15).

Bodnar, R.J., 1993. Revised equation and table for determining the freezing point depression of H 2 O-NaCl solutions. *Geochimica et Cosmochimica Acta*, *57*(3), pp.683-684.

Bond, G.C. and Kominz, M.A., 1984. Construction of tectonic subsidence curves for the early Paleozoic miogeocline, southern Canadian Rocky Mountains: Implications for subsidence mechanisms, age of breakup, and crustal thinning. Geological Society of America Bulletin, 95(2), pp.155-173.

Bonin, B., 2004. Do coeval mafic and felsic magmas in post-collisional to within-plate regimes necessarily imply two contrasting, mantle and crustal, sources? A review. *Lithos*, *78*(1), pp.1-24.

Borthwick, J. and Harmon, R.S., 1982. A note regarding CIF3 as an alternative to BrF5 for oxygen isotope analysis. Geochimica et Cosmochimica Acta, 46(9), pp.1665-1668.

Bottinga, Y., 1968. Calculation of fractionation factors for carbon and oxygen isotopic exchange in the system calcite-carbon dioxide-water. *The Journal of Physical Chemistry*, *72*(3), pp.800-808.

Boutton, T.W., 1991. Stable carbon isotope ratios of natural materials: II. Atmospheric, terrestrial, marine, and freshwater environments. *Carbon isotope techniques*, *1*, p.173.

Bowman, J.R., Covert, J.J., Clark, A.H. and Mathieson, G.A., 1985. The CanTung E Zone scheelite skarn orebody, Tungsten, Northwest Territories; oxygen, hydrogen, and carbon isotope studies. *Economic Geology*, *80*(7), pp.1872-1895.

Buzon, M.R., Simonetti, A. and Creaser, R.A., 2007. Migration in the Nile Valley during the New Kingdom period: a preliminary strontium isotope study. Journal of Archaeological Science, 34(9), pp.1391-1401.

Canet, C., Franco, S.I., Prol-Ledesma, R.M., González-Partida, E. and Villanueva-Estrada, R.E., 2011. A model of boiling for fluid inclusion studies: Application to the Bolaños Ag–Au–Pb–Zn epithermal deposit, Western Mexico. *Journal of Geochemical Exploration*, *110*(2), pp.118-125.

Cathro, R.J., 1967. Preliminary report on 1967 exploration program on the Caribou Lake property; report for Northern Empire Mines Ltd. by Archer, Cathro & Associates (1981) Limited; assessment report #019007.

Chacko, T. and Deines, P., 2008. Theoretical calculation of oxygen isotope fractionation factors in carbonate systems. Geochimica et Cosmochimica Acta, 72(15), pp.3642-3660.

Chappell, B. and White, A., 1974. Two contrasting granite types. *Pacific geology*, *8*(2), pp.173-174.

Chutas, N.I., Kress, V.C., Ghiorso, M.S. and Sack, R.O., 2008. A solution model for high-temperature PbS-AgSbS2-AgBiS2 galena. *American Mineralogist*, *93*(10), pp.1630-1640.

Clayton, R.N., O'Neil, J.R. and Mayeda, T.K., 1972. Oxygen isotope exchange between quartz and water. Journal of Geophysical Research, 77(17), pp.3057-3067.

Clemens, J.D., 2003. S-type granitic magmas—petrogenetic issues, models and evidence. *Earth-Science Reviews*, *61*(1), pp.1-18.

Clowes, R.M., Hammer, P.T., Fernández-Viejo, G. and Welford, J.K., 2005. Lithospheric structure in northwestern Canada from Lithoprobe seismic refraction and related studies: a synthesis. *Canadian Journal of Earth Sciences*, *42*(6), pp.1277-1293.

Colpron, M., Logan, J.M. and Mortensen, J.K., 2002. U-Pb zircon age constraint for late Neoproterozoic rifting and initiation of the lower Paleozoic passive margin of western Laurentia. Canadian Journal of Earth Sciences, 39(2), pp.133-143.

Colpron, M., Nelson, J.L. and Murphy, D.C., 2007. Northern Cordilleran terranes and their interactions through time. GSA TODAY, 17(4/5), p.4.

Colpron, M. and Nelson, J.L., 2011. A Palaeozoic NW Passage and the Timanian, Caledonian and Uralian connections of some exotic terranes in the North American Cordillera. Geological Society, London, Memoirs, 35(1), pp.463-484.

Coney, P.J., Jones, D.L. and Monger, J.W., 1980. Cordilleran suspect terranes. Nature, 288(5789), pp.329-333.

Cook, N.J., Ciobanu, C.L., Pring, A., Skinner, W., Shimizu, M., Danyushevsky, L., Saini-Eidukat, B. and Melcher, F., 2009. Trace and minor elements in sphalerite: A LA-ICPMS study. *Geochimica et Cosmochimica Acta*, *73*(16), pp.4761-4791.

Cooke, B.J. and Godwin, C.I., 1984. Geology, mineral equilibria, and isotopic studies of the McDame tungsten skarn prospect, north-central British Columbia. *Economic Geology*, *79*(5), pp.826-847.

Corbett, G., 2002. Epithermal gold for explorationists. AIG Journal, Paper 1.

Corbett, G.J. and Leach, T.M., 1998. Southwest Pacific Rim gold-copper systems: structure, alteration, and mineralization (p. 234). Society of Economic Geologists.

Craig, H., The isotopic geochemistry of water and carbon in geothermal areas, Nuclear Geology on Geothermal Areas—Spoleto, 1963 E.

Deditius, A.P., Utsunomiya, S., Renock, D., Ewing, R.C., Ramana, C.V., Becker, U. and Kesler, S.E., 2008. A proposed new type of arsenian pyrite: Composition, nanostructure and geological significance. Geochimica et Cosmochimica Acta, 72(12), pp.2919-2933.

Deer, W.A., Howie, R.A. and Zussman, J., 1963. Rock Forming minerals, vol 3: Sheet Silicates.

Deines, P., 2004. Carbon isotope effects in carbonate systems. Geochimica et Cosmochimica Acta, 68(12), pp.2659-2679.

Dilworth, K.M., Mortensen, J.K., Ebert, S., Tosdal, R.M., Smith, M.T. and Roberts, P., 2007. Cretaceous reduced granitoids in the Goodpaster Mining District, east central Alaska. *Canadian Journal of Earth Sciences*, *44*(9), pp.1347-1373.

Drummond, S.E. and Ohmoto, H., 1985. Chemical evolution and mineral deposition in boiling hydrothermal systems. *Economic geology*, *80*(1), pp.126-147.

Dumala, M.R., 2014. Assessment report describing geological mapping, prospecting, geochemical surveys and diamond drilling at the Keg Property by Archer, Cathro & Associates (1981) Limited.

Dusel-Bacon, C., Hopkins, M.J., Mortensen, J.K., Dashevsky, S.S., Bressler, J.R. and Day, W.C., 2006. Paleozoic tectonic and metallogenic evolution of the pericratonic rocks of east-central Alaska and adjacent Yukon. *Paleozoic evolution and metallogeny of pericratonic terranes at the ancient Pacific margin of North America, Canadian and Alaskan Cordillera: Geological Association of Canada Special Paper*, *45*, pp.25-74.

Ekart, D.D., Cerling, T.E., Montanez, I.P. and Tabor, N.J., 1999. A 400 million year carbon isotope record of pedogenic carbonate: implications for paleoatmospheric carbon dioxide. *American Journal of Science*, *299*(10), pp.805-827.

Falck, H., 2007. A Review of the Bedrock Geology of the Nahanni River Region and Its Context in the Northern Cordillera.

Faure, G., 1986. Principles of isotope geochemistry. *John Wiley and Sons. chapters*, *6*(7), p.8.

Flood, R.H. and Shaw, S.E., 1975. A cordierite-bearing granite suite from the New England Batholith, NSW, Australia. *Contributions to Mineralogy and Petrology*, *52*(3), pp.157-164.

Foster, F., 1976. Geological and geochemical report on the Raz 1-20 claim group; report for Welcome North Mines Ltd.; assessment report #090127.

Foster, F. and Holland, R. T., 1977. Geological and geochemical report on the Raz 1-182 claim group; report for Welcome North Mines Ltd.; assessment report #090267.

Gabrielse, H., Murphy, D.C. and Mortensen, J.K., 2006. Cretaceous and Cenozoic dextral orogen-parallel displacements, magmatism, and paleogeography, north-central Canadian Cordillera. *Paleogeography of the North American Cordillera: Evidence For and Against Large-Scale Displacements: Geological Association of Canada Special Paper*, *46*, pp.255-276.

George, L., Cook, N.J., Cristiana, L. and Wade, B.P., 2015. Trace and minor elements in galena: A reconnaissance LA-ICP-MS study. *American Mineralogist*, *100*(2-3), pp.548-569.

Ghosal, S. and Sack, R.O., 1999. Bi-Sb energetics in sulfosalts and sulfides. *Mineralogical Magazine*, *63*(5), pp.723-733.

Giggenbach, W.F., 1995. Variations in the chemical and isotopic composition of fluids discharged from the Taupo Volcanic Zone, New Zealand. Journal of Volcanology and Geothermal Research, 68(1), pp.89-116.

Giesemann, A., Jäger, H.J., Norman, A.L., Krouse, H.R. and Brand, W.A., 1994. Online sulfur-isotope determination using an elemental analyzer coupled to a mass spectrometer. Analytical Chemistry, 66(18), pp.2816-2819.

Goldstein, R.H. and Reynolds, T.J., 1994. Systematics of fluid inclusions in diagenetic minerals: SEPM Short Course 31. *Society for Sedimentary Geology*, *199*.

Goodfellow, W.D. and Jonasson, I.R., 1986. Environment of formation of the Howards Pass (XY) Zn-Pb deposit, Selwyn Basin, Yukon. Mineral Deposits of Northern Cordillera, pp.19-50.

Gordey, S.P., 2013. Evolution of the Selwyn Basin region, Sheldon Lake and Tay River map areas, central Yukon. Geological Survey of Canada, Bulletin 599

Gordey, S.P. and Anderson, R.G., 1993. Evolution of the northern Cordilleran miogeocline, Nahanni map area (1051), Yukon and Northwest territories.

Gordey, S.P. and Irwin, S.E.B., 1987. Geological Survey of Canada, Geology of Sheldon Lake and Tay River Map Areas, Yukon Territory. Geological Survey of Canada. Vancouver

Hantelmann, J.J., 2013. The paragenesis and geochemistry of the Bellekeno Ag-Pb-Zn vein, Keno Hill district, Yukon, Canada. Masters. University of Alberta

Hart, C.J., Goldfarb, R.J., Lewis, L.L. and Mair, J.L., 2004. The Northern Cordilleran Mid-Cretaceous Plutonic Province: Ilmenite/Magnetite-series Granitoids and Intrusion-related Mineralisation. *Resource Geology*, *54*(3), pp.253-280.

Hart, C.J., Mair, J.L., Goldfarb, R.J. and Groves, D.I., 2005. Source and redox controls on metallogenic variations in intrusion-related ore systems, Tombstone-Tungsten Belt, Yukon Territory, Canada. Transactions of the Royal Society of Edinburgh: Earth Sciences, 95(1-2), pp.339-356.

Heaman, L.M., Erdmer, P. and Owen, J.V., 2002. U-Pb geochronologic constraints on the crustal evolution of the Long Range Inlier, Newfoundland. Canadian Journal of Earth Sciences, 39(5), pp.845-865.

Hedenquist, J.W. and Henley, R.W., 1985. The importance of CO 2 on freezing point measurements of fluid inclusions; evidence from active geothermal systems and implications for epithermal ore deposition. *Economic geology*, *80*(5), pp.1379-1406.

Hine, R., Williams, I.S., Chappell, B.W. and White, A.J.R., 1978. Contrasts between I-and S-type granitoids of the Kosciusko Batholith. *Journal of the Geological Society of Australia*, *25*(3-4), pp.219-234.

Hodges, K.V., 2005. Thermochronology in Orogenic Systems. *The crust*, *3*, p.263.

Hoffman, E.L., 1992. Instrumental neutron activation in geoanalysis. Journal of Geochemical Exploration, 44(1), pp.297-319.

Hoffman, P.F., 1989. Speculations on Laurentia's first gigayear (2.0 to 1.0 Ga). Geology, 17(2), pp.135-138.

Hofmann, A.W., 1988. Chemical differentiation of the Earth: the relationship between mantle, continental crust, and oceanic crust. *Earth and Planetary Science Letters*, *90*(3), pp.297-314.

Hofmann, H.J. and Cecile, M.P., 1981. Occurrence of Oldhamia and other trace fossils in lower Cambrian (?) argillites, Niddery Lake map area, Selwyn Mountains, Yukon Territory. Current Research, Part A. Geological Survey of Canada, Paper, pp.281-290.

Holland, R. T., 1977. Report on diamond drilling program on the Raz 1-182 mineral claims; report for Welcome North Mines Ltd.; assessment report #091251.

Hutchison, M.N. and Scott, S.D., 1981. Sphalerite geobarometry in the Cu-Fe-Zn-S system. *Economic Geology*, *76*(1), pp.143-153.

Ishihara, S., Hashimoto, M. and Machida, M., 2000. Magnetite/Ilmenite–series Classification and Magnetic Susceptibility of the Mesozoic-Cenozoic Batholiths in Peru. *Resource Geology*, *50*(2), pp.123-129.

Jaffey, A.H., Flynn, K.F., Glendenin, L.E., Bentley, W.T. and Essling, A.M., 1971. Precision measurement of half-lives and specific activities of U 235 and U 238. Physical Review C, 4(5), p.1889.

Jefferson, C.W. and Spirito, W.A., 2003. Mineral and energy resource assessment of the Tlogotsho Plateau, Nahanni Karst, Ragged Ranges and adjacent areas under consideration for expansion of Nahanni National Park Reserve, Northwest Territories. *Geological Survey of Canada Open File*, *1686*(1).

Johan, Z., 1988. Indium and germanium in the structure of sphalerite: an example of coupled substitution with copper. *Mineralogy and Petrology*, *39*(3-4), pp.211-229.

John, D.A., 2001. Miocene and early Pliocene epithermal gold-silver deposits in the northern Great Basin, western United States: Characteristics, distribution, and relationship to magmatism. Economic Geology, 96(8), pp.1827-1853.

Kay, S.M. and Mpodozis, C., 2001. Central Andean ore deposits linked to evolving shallow subduction systems and thickening crust. GSA TODAY, 11(3), pp.4-9.

Kay, S.M., Mpodozis, C., Ramos, V.A., and Munizaga, F., 1991, Magma source variations for mid–late Tertiary magmatic rocks associated with a shallowing subduction zone and a thickening crust in the central Andes (28 to 33°S), *in* Harmon, R.S., and Rapela, C.W., eds., Andean magmatism and its tectonic setting: Boulder, Colorado, Geol. Soc. America Special Paper 265, p. 113–137.

Kelley, K.D., Leach, D.L., Johnson, C.A., Clark, J.L., Fayek, M., Slack, J.F., Anderson, V.M., Ayuso, R.A. and Ridley, W.I., 2004. Textural, compositional, and sulfur isotope variations of sulfide minerals in the Red Dog Zn-Pb-Ag deposits, Brooks Range, Alaska: implications for ore formation. *Economic Geology*, *99*(7), pp.1509-1532.

Kemp, A.I.S. and Hawkesworth, C.J., 2003. Granitic perspectives on the generation and secular evolution of the continental crust. Treatise on Geochemistry. *10*, pp.B0-08.

Kim, S-T., Kang, J.O., Yun, S-T., O'Neil J.R. and Mucci, A., 2009. Experimental studies of oxygen isotope fractionation between rhodochrosite ($MnCO_3$) and water at low temperatures. Geochimica et Cosmochimica Acta, 73, pp.4400-4408.

Kistler, R.W., 1974. Phanerozoic batholiths in western North America. *Annual Review of Earth and Planetary Sciences*, *2*, p.403.

Large, R.R., Bull, S.W. and Maslennikov, V.V., 2011. A carbonaceous sedimentary source-rock model for Carlin-type and orogenic gold deposits. *Economic Geology*, *106*(3), pp.331-358.

Layne, G.D., Longstaffe, F.J. and Spooner, E.T.C., 1991. The JC tin skarn deposit, southern Yukon Territory; II, A carbon, oxygen, hydrogen, and sulfur stable isotope study. *Economic Geology*, *86*(1), pp.48-65.

Lewis, L., 2009. Yukon mineral deposits summary 2009.

Ludwig, K.R., 1992. ISOPLOT: a plotting and regression program for radiogenic-isotope data, Version 2.57, US Geological Survey Open-File Report No. 91-445 US Geological Survey, USA.

Ludwig, K.R., 2003. Isoplot 3.00, a geochronological tool-kit for Excel: Berkely Geochronology Center Special Publication 4, pp.67.

Lueth, V.W., Megaw, P.K., Pingitore, N.E. and Goodell, P.C., 2000. Systematic variation in galena solid-solution compositions at Santa Eulalia, Chihuahua, Mexico. *Economic Geology*, *95*(8), pp.1673-1687.

Lynch, J.G., 1989. Large-scale hydrothermal zoning reflected in the tetrahedrite-freibergite solid solution, Keno Hill Ag-Pb-Zn District, Yukon. *Canadian Mineralogist*, *27*, pp.383-400.

Lynch, J.V.G., Longstaffe, F.J. and Nesbitt, B.E., 1990. Stable isotopic and fluid inclusion indications of large-scale hydrothermal paleoflow, boiling, and fluid mixing in the Keno Hill Ag-Pb-Zn district, Yukon Territory, Canada. *Geochimica et Cosmochimica Acta*, *54*(4), pp.1045-1059.

Mair, J.L., Hart, C.J. and Stephens, J.R., 2006. Deformation history of the northwestern Selwyn Basin, Yukon, Canada: Implications for orogen evolution and mid-Cretaceous magmatism. Geological Society of America Bulletin, 118(3-4), pp.304-323.

Mango, H., Arehart, G., Oreskes, N. and Zantop, H., 2014. Origin of epithermal Ag–Au–Cu–Pb–Zn mineralization in Guanajuato, Mexico. *Mineralium Deposita*, *49*(1), pp.119-143.

Mattey, D.P., Carr, R.H., Wright, I.P. and Pillinger, C.T., 1984. Carbon isotopes in submarine basalts. *Earth and Planetary Science Letters*, *70*(2), pp.196-206.

Monger, J.W.H., Price, R.A. and Tempelman-Kluit, D.J., 1982. Tectonic accretion and the origin of the two major metamorphic and plutonic welts in the Canadian Cordillera. Geology, 10(2), pp.70-75.

Mortensen, J.K., 2008. Middle Cretaceous calderas in eastern Alaska and associated ignimbrites and distal outflow tuffs in west-central Yukon: Whitehorse. In Yukon Geoscience Forum, November (pp. 23-25).

Mortensen, J.K. and Ballantyne, S.B., 1992. Age and Pb isotopic studies of Ag-Sn-base metal epigenetic mineralization in the Mount Mye area, east-central Yukon Territory. Geological Survey of Canada, pp.129-129.
Vancouver

Mortensen, J.K., Hart, C.J.R., 2010. Late and post-accretionary Mesozoic magmatism and metallogeny in the northern Cordillera, Yukon and east-central Alaska, in: Abstracts with Program. Geological Society of America, Tucson, p. 676.

Mortensen, J.K., Hart, C.J.R., Murphy, D.C. and Heffernan, S., 2000. Temporal evolution of Early and mid-Cretaceous magmatism in the Tintina Gold Belt. British Columbia and Yukon Chamber of Mines, pp.49-57.

Murphy, D.C. and Bevier, M.L., 1997. *Geology of the McQuesten River Region, Northern McQuesten and Mayo Map Area, Yukon Territory (115P/14, 15, 16; 105M/13, 14).* Indian and Northern Affairs Canada, Exploration Geological Services Division, Yukon Region.

Murphy, D.C., Mortensen, J.K. and Bevier, M.L., 1995. U-Pb and K-Ar geochronology of Cretaceous and Tertiary intrusions, western Selwyn Basin, and implications for the structural and metallogenic evolution of central Yukon. In *Geological Association of Canada, Program with Abstracts* (Vol. 20, p. A74).

Murphy, D.C., Colpron, M., Roots, C.F., Gordey, S.P. and Abbott, J.G., 2001. Finlayson Lake targeted geoscience initiative (southeastern Yukon), Part 1: Bedrock geology. *Yukon exploration and geology*, pp.189-207.

Murphy, D.C., Mortensen, J.K., Piercey, S.J., Orchard, M.J. and Gehrels, G.E., 2006. Mid-Paleozoic to early Mesozoic tectonostratigraphic evolution of Yukon-Tanana and Slide Mountain terranes and affiliated overlap assemblages, Finlayson Lake massive sulphide district, southeastern Yukon. *Paleozoic evolution and metallogeny of pericratonic terranes at the ancient Pacific margin of North America, Canadian and Alaskan Cordillera: Geological Association of Canada Special Paper*, *45*, pp.75-105.

Nelson, J. and Colpron, M., 2007. Tectonics and metallogeny of the British Columbia, Yukon and Alaskan Cordillera, 1.8 Ga to the present. Mineral deposits of Canada: a synthesis of major deposit-types, district metallogeny, the evolution of geological provinces, and exploration methods: Geological Association of Canada, Mineral Deposits Division, Special Publication, 5, pp.755-791.

O'Neil, J.R., Clayton, R.N. and Mayeda, T.K., 1969. Oxygen isotope fractionation in divalent metal carbonates. Univ. of Chicago.

Ohmoto, H., 1972. Systematics of sulfur and carbon isotopes in hydrothermal ore deposits. *Economic Geology*, *67*(5), pp.551-578.

Ohmoto, H. and Rye, R., (1979) Isotopes of sulfur and carbon. Geochemistry of Hydrothermal Ore Deposits (ed, pp.509-567.

Orchard, M.J., 1991. Upper Triassic conodont biochronology and new index species from the Canadian Cordillera. Geological Survey of Canada Bulletin, 417, pp.229-339.

Parrish, R.R., 1990. U-Pb dating of monazite and its application to geological problems. Canadian Journal of Earth Sciences, 27(11), pp.1431-1450.

Peacor, D.R., Essene, E.J. and Gaines, A.M., 1987. Petrologic and crystal-chemical implications of cation order-disorder in kutnahorite [CaMn (CO 3) 2]. *American Mineralogist*, *72*(3-4), pp.319-328.

Pearce, J.A., Harris, N.B. and Tindle, A.G., 1984. Trace element discrimination diagrams for the tectonic interpretation of granitic rocks. Journal of petrology, 25(4), pp.956-983.

Phillips, E.R., 1974. Myrmekite—one hundred years later. Lithos, 7(3), pp.181-194.

Pigage, L.C. and Anderson, R.G., 1985. The Anvil plutonic suite, Faro, Yukon Territory. Canadian Journal of Earth Sciences, 22(8), pp.1204-1216.

Pigage, L.C. and Cordey, F., 2004. Bedrock Geology Compilation of the Anvil District (parts of NTS 105K/2, 3, 5, 6, 7, and 11), Central Yukon. Yukon Energy, Mines and Resources.

Pigage, L.C. and Mortensen, J.K., 2004. Superimposed Neoproterozoic and early Tertiary alkaline magmatism in the La Biche River area, southeast Yukon Territory. Bulletin of Canadian Petroleum Geology, 52(4), pp.325-342.

Pigage, L.C., Crowley, J.L., Roots, C.F. and Abbot, J.G., 2014. Geochemistry and U–Pb zircon geochronology of mid-Cretaceous Tay River suite intrusions in southeast Yukon. Yukon Exploration and Geology, pp.169-194.

Polat, A. and Longstaffe, F.J., 2014. A juvenile oceanic island arc origin for the Archean (ca. 2.97 Ga) Fiskenæsset anorthosite complex, southwestern Greenland: evidence from oxygen isotopes. Earth and Planetary Science Letters, 396, pp.252-266.

Powell, C.M., Li, Z.X., McElhinny, M.W., Meert, J.G. and Park, J.K., 1993. Paleomagnetic constraints on timing of the Neoproterozoic breakup of Rodinia and the Cambrian formation of Gondwana. Geology, 21(10), pp.889-892.

Rainbird, R.H., Jefferson, C.W. and Young, G.M., 1996. The early Neoproterozoic sedimentary Succession B of northwestern Laurentia: Correlations and paleogeographic significance. Geological Society of America Bulletin, 108(4), pp.454-470.

Rasmussen, K.L., 2013. The timing, composition, and petrogenesis of syn-to post-accretionary magmatism in the northern Cordilleran miogeocline, eastern Yukon and southwestern Northwest Territories (Doctoral dissertation, University of British Columbia).

Ray, G.E., Webster, I.C.L., Ballantyne, S.B., Kilby, C.E. and Cornelius, S.B., 2000. The geochemistry of three tin-bearing skarns and their related plutonic rocks, Atlin, Northern British Columbia. Economic Geology, 95(6), pp.1349-1365.

Renock, D. and Becker, U., 2011. A first principles study of coupled substitution in galena. *Ore Geology Reviews*, *42*(1), pp.71-83.

Roberts, M.P. and Clemens, J.D., 1993. Origin of high-potassium, talc-alkaline, I-type granitoids. *Geology*, *21*(9), pp.825-828.

Robertson, R.C.R. and Wallis, J.E., 1989. Cody Ridge project summary report (1 of 2), 1988 exploration report for Doron Explorations Inc.; assessment report #092896.

Roedder, E., 1984. Fluid inclusions (Vol. 12, pp. 12-45). Washington, DC: Mineralogical Society of America.

Ross, G.M., 1991. Tectonic setting of the Windermere Supergroup revisited. Geology, 19(11), pp.1125-1128.

Rosso, K.M. and Vaughan, D.J., 2006. Sphalerite and wurtzite: Sulfide mineralogy and geochemistry. *Reviews in Mineralogy and Geochemistry*, *61*, p.599.

Rye, R.O. and Ohmoto, H., 1974. Sulfur and carbon isotopes and ore genesis: a review. *Economic Geology*, *69*(6), pp.826-842.

Schärer, U., 1984. The effect of initial230Th disequilibrium on young UPb ages: the Makalu case, Himalaya. Earth and Planetary Science Letters, 67(2), pp.191-204.

Seward, T.M., 1976. The stability of chloride complexes of silver in hydrothermal solutions up to 350 C. *Geochimica et Cosmochimica Acta*, *40*(11), pp.1329-1341.

Shand, S.J., 1943. Eruptive Rocks: Their genesis, composition, and classification, with a chapter on meteorites. J. Wiley & sons, Incorporated.

Sharp, Z., 2007. *Principles of stable isotope geochemistry* (p. 344). Upper Saddle River, NJ: Pearson Education.

Sillitoe, R.H., 1995, November. Exploration of porphyry copper lithocaps. In Proceedings of Pacific Rim Congress (Vol. 95, pp. 527-532).

Sillitoe, R.H., 1999. Styles of high-sulphidation gold, silver and cop per mineralization in the porphyry and epithermal environ ments. In PacRim'99 Congress Proceedings, Bali, Indonesia.

Sillitoe, R.H., 2002. Some metallogenic features of gold and copper deposits related to alkaline rocks and consequences for exploration. Mineralium Deposita, 37(1), pp.4-13.

Sillitoe, R.H. and Hedenquist, J.W., 2003. Linkages between volcanotectonic settings, ore-fluid compositions, and epithermal precious metal deposits. Special Publication-Society of Economic Geologists, 10, pp.315-343.

Simmons, S.F. and Christenson, B.W., 1994. Origins of calcite in a boiling geothermal system. *American Journal of Science*, *294*(3), pp.361-400.

Simmons, S.F., Arehart, G., Simpson, M.P. and Mauk, J.L., 2000. Origin of massive calcite veins in the Golden Cross low-sulfidation, epithermal Au-Ag deposit, New Zealand. *Economic Geology*, *95*(1), pp.99-112.

Simonetti, A., Heaman, L.M., Chacko, T. and Banerjee, N.R., 2006. In situ petrographic thin section U–Pb dating of zircon, monazite, and titanite using laser ablation–MC–ICP-MS. International Journal of Mass Spectrometry, 253(1), pp.87-97.

Sinclair, A.J., Tessari, O.J. and Harakal, J.E., 1980. Age of Ag-Pb-Zn mineralization, Keno Hill-Galena Hill area, Yukon Territory. *Canadian Journal of Earth Sciences*, *17*(8), pp.1100-1103.

Stoffregen, R.E., 1987. Genesis of acid-sulfate alteration and Au-Cu-Ag mineralization at Summitville, Colorado. Economic Geology, 82(6), pp.1575-1591.

Sun, S.S. and McDonough, W.S., 1989. Chemical and isotopic systematics of oceanic basalts: implications for mantle composition and processes. Geological Society, London, Special Publications, 42(1), pp.313-345.

Taylor, B.E., 1986. Magmatic volatiles; isotopic variation of C, H, and S. *Reviews in Mineralogy and Geochemistry*, *16*(1), pp.185-225.

Templeman-Kluit, D.J., 1979. Transported cataclasite, ophiolite and granodioride in Yukon: evidence of arc-continent collision Geol. Surv. of Canada Pap, pp.79-14.
Thorkelson, D.J., Abbott, J.G., Mortensen, J.K., Creaser, R.A., Villeneuve, M.E., McNicoll, V.J. and Layer, P.W., 2005. Early and middle Proterozoic evolution of Yukon, Canada. Canadian Journal of Earth Sciences, 42(6), pp.1045-1071.

Thomson, D., Schröder-Adams, C.J., Hadlari, T., Dix, G. and Davis, W.J., 2011. Albian to Turonian stratigraphy and palaeoenvironmental history of the northern Western Interior Sea in the Peel Plateau region, Northwest Territories, Canada. Palaeogeography, Palaeoclimatology, Palaeoecology, 302(3), pp.270-300.

Truesdell, A.H., 1974. Oxygen isotope activities and concentrations in aqueous salt solutions at elevated temperatures: Consequences for isotope geochemistry. *Earth and Planetary Science Letters*, *23*(3), pp.387-396.

Truesdell, A.H., Nathenson, M. and Rye, R.O., 1977. The effects of subsurface boiling and dilution on the isotopic compositions of Yellowstone thermal waters. *Journal of Geophysical Research*, *82*(26), pp.3694-3704.

Veizer, J., Ala, D., Azmy, K., Bruckschen, P., Buhl, D., Bruhn, F., Carden, G.A., Diener, A., Ebneth, S., Godderis, Y. and Jasper, T., 1999. 87Sr/86Sr, δ13C and δ18O evolution of Phanerozoic seawater. *Chemical geology*, *161*(1), pp.59-88.

Vogel, J.C., Grootes, P.M. and Mook, W.G., 1970. Isotopic fractionation between gaseous and dissolved carbon dioxide. *Zeitschrift für Physik*, *230*(3), pp.225-238.

Werdon, M.B., Newberry, R.J., Athey, J.R. and Szumigala, D.J., 2004. Bedrock geologic map of the Salcha River–Pogo area, Big Delta quadrangle, Alaska. Report of Investigations, p.1b.

White, N.C. and Hedenquist, J.W., 1990. Epithermal environments and styles of mineralization: variations and their causes, and guidelines for exploration. Journal of Geochemical Exploration, 36(1), pp.445-474.

White, N.C. and Hedenquist, J.W., 1995. Epithermal gold deposits: styles, characteristics and exploration. SEG newsletter, 23(1), pp.9-13.

Wilkinson, J.J., Simmons, S.F. and Stoffell, B., 2013. How metalliferous brines line Mexican epithermal veins with silver. *Nature scientific reports*, *3*. pp.1-7.

Wright, D.F., Lemkow, D. and Harris, J.R., 2007. Mineral and energy resource assessment of the Greater Nahanni Ecosystem under consideration for the expansion of the Nahanni National Park Reserve, Northwest Territories: Geological Survey of Canada, Open File 5344, 557 p. *Geological Survey of Canada*.

Chapter 5 - Appendices

Appendix 1 - Samples

	Thin Section	EPMA EDS	EPMA WDS	LA-ICP-MS	Description
HAM12-16					
11571	x	x			Late stage chlorite veins and associated sulfides
19173	x	x			Late stage chlorite veins and associated sulfides
25876	x	x			Vein showing three generations of mineral growth, calcite, quartz and post ore mineralization
26000	x	x			Brecciated quartz vein with ubiquitous sulfides
26400	x	x			Quartz vein with several sulfide occurrences
HAM12-17					
8120	x	x			Single thin section displaying quartz vein with sulfides and zone of brecciation
8228	x	x			Breccia with varying cement types and sulfides
8269	x	x			Single thin section with several different quartz veins
11098	x	x	x		Contact between rhodochrosite and quartz, showing rhodochrosite overgrowing quartz
13792	x	x	x	x	Vein showing 4 generations of mineral growth, including calcite and rhodochrosite. Also present are at least two generations of sulfide growth
19042	x	x			Quartz and calcite veining with associated sulfides, mostly pyrite.
27306	x	x	x	x	Side-by-side rhodochrosite and calcite veins. Numerous sulfides present in calcite veins. Rhodochrosite veins shown to crosscut calcite veins.
HAM12-18					
18005	x	x			Quartz vein overgrowing carbonate (calcite) with sulfides present associated with the quartz phase
18054	x	x	x		Thin section showing rhodochrosite and quartz veining. Rhodochrosite vein contains sulfides. Several breccias also present.
18450	x	x	x	x	Large rhodochrosite vein containing ubiquitous sulfides. Best example of style of mineralization associated with rhodochrosite mineralization
HAM12-19					
17261	x	x			Large quartz vein with minor sulfides
HAM12-20					
1922	x	x	x		Bladed calcite thin section
19800	x	x			Rhodochrosite vein with some minor sulfides present.

Appendix 1.1 samples chosen from thin sections for EPMA and LA-ICP-MS analysis

	C,O Isotopes	O Isotopes	S Isotopes	Sr Isotopes	Mineral assemblage	Description
HAM12-16						
1354			x		Rds	Rhodochrosite vein containing minor sulfides-sphalerite
1407			x		Rds	Coexisting calcite and rhodochrosite veins. The rhodochrosite vein contains minor amounts of sphalerite
1407	x				Cal	
6053	x				Cal	Barren calcite vein
7043		x			Qtz2	Large barren quartz vein
7439	x				Cal	Minor sulfide bearing calcite vein
17587	x				Cal	Large bladed calcite vein
18540	x				Cal	Several small barren calcite veins from the same paragenetic stage
25082				x	Rds	Coexisting calcite and rhodochrosite veins, one crosscutting the other, both relatively barren
25082	x				Cal	
25876		x			Qtz2	Samples shows two generations of quartz veining, the first is overgrowing
25876		x			Qtz1	
26000		x			Qtz1	Brecciated quartz vein
27488		x			Qtz2	Large, late quartz vein
HAM12-17						
5819	x				Cal	Small barren calcite vein
8269A		x			Qtz2	Sample cut by many quartz veins. Most barren, few with very minor sulfide occurences
8269B		x			Qtz2	
8269C		x			Qtz2	
8269D		x			Qtz2	
8269F		x			Qtz2	
8269G		x			Qtz2	
11098	x				Rds	Large rhodochrosite vein in contact with quartz
13792	x			x	Cal	Vein showing many stages of paragenesis overgrwoing each other, dominated by calcite
18300				x	Rds	Sample with calcite vein being crosscut by rhodochrosite vein on mm scale
18300	x				Cal	
19204		x			Qtz1	Massive quartz sample with small pockets of calcite, late rhodochrosite vein crosscuts everything
19204				x	Cal	
19204a	x				Rds	
19204b	x				Rds	
27129a	x				Cal	Side-by-side calcite and rhodochrosite veins minor sulfide occurrences
27129b	x				Rds	
27306				x	Cal	Side-by-side moderately sized calcite and rhodochrosite veins minor sulfide occurrences in calcite, no sulfide occurrences in rhodochrosite.
27306	x				Rds	

Appendix 1.2 Samples picked for various types of isotopic analysis

HAM12-18						
18035a	x			x	Rds	Large, sulfide-bearing rhodochrosite vein displaying crustiform textures
18035b	x				Rds	
18054	x			x	Rds	Side-by-side quartz and rhodochrosite bearing veins, both of which contain large amounts of sulfides
18054		x			Qtz1	
18450			x	x	Rds	Large, rhodochrosite vein, containing ubiquitous sulfides alongisde much smaller quartz vein, no relationship in this sample
18450		x			Qtz1	
HAM12-19						
12155				x	Rds	Very small rhodochrosite vein beside much larger calcite vein. Also small overgrwoths of rhodochrosite in calcite vein
12155	x				Cal	
17261		x			Qtz1	Large quartz vein containing minor sulfides
19886	x			x	Cal	Calcite vein, partially brecciated at one end
22717	x				Cal	Small barren calcite vein
HAM12-20						
16757		x			Qtz2	Very large quartz vein with small rhodochrosite overgrowths
19800	x				Rds	Large rhodochrosite vein
21162		x			Qtz2	Large barren quartz vein

	Whole Rock Geochemistry	**Description**
HAM12-20		
8322	x	Potassically altered Anvil Suite granite
9440	x	Potassically altered Anvil Suite granite
8886	x	Potassically altered Anvil Suite granite
7763	x	Potassically altered Anvil Suite granite
10029	x	Potassically altered Anvil Suite granite
1326	x	Potassically altered Anvil Suite granite
8630	x	Potassically altered Anvil Suite granite
1752	x	Potassically altered Anvil Suite granite
20101	x	Potassically altered Anvil Suite granite
	Fluid Inclusion Waifer	
HAM12-17		
17587	x	Large bladed calacite vein
8269	x	Several large, coeval, fluid inclusion rich quartz veins
HAM12-18		
13223	x	Large barren quartz vein
18005	x	Ore stage quartz vein, fluid inclusions ubiquitous
18035	**x**	Rhodochrosite vein
18054	x	Large rhodochrosite vein
18450	x	Largest rhodochrosite vein
	Geochronology	
HAM12-20		
8630	Monazites	Potassically altered Anvil Suite granite
14794	Zircons	Potassically altered Anvil Suite granite

Appendix 1.2 Continued (above)
Appendix 1.3 (left) samples used for whole rock geochemistry analysis, samples chosen for fluid inclusion waifers and samples chosen for geochronology

Appendix 2 – EPMA Data

Calcite

Pb	As	S	Bi	Fe	Sb	Zn	Ag	Cd	Cu	Te	Se	Sn	In	Mn	Total	Sample Number
Galena																
86.17	~	13.06	~	~	0.16	~	~	~	~	~	~	~	~	~	99.63	**12-17-27306**
85.15	~	13.20	~	~	0.16	~	~	~	~	~	~	~	~	~	98.70	**12-17-27306**
85.45	~	13.21	~	~	0.18	~	~	~	~	~	~	~	~	~	99.13	**12-17-27306**
85.59	~	13.24	~	~	0.18	~	~	~	~	~	~	~	~	~	99.19	**12-17-27306**
85.10	~	13.19	~	~	0.13	~	~	~	~	~	~	~	~	~	98.71	**12-17-27306**
85.62	~	13.25	~	0.43	0.14	~	~	~	~	~	~	~	~	~	99.65	**12-17-27306**
85.74	~	13.31	~	1.91	0.20	~	~	~	~	~	~	~	~	~	101.41	**12-17-27306**
85.55	~	13.25	~	1.29	0.14	~	~	~	~	~	~	~	~	~	100.40	**12-17-27306**
84.98	~	13.10	~	1.95	0.14	~	~	~	~	~	~	~	~	~	100.37	**12-17-27306**
86.10	~	13.27	~	~	0.07	~	~	~	~	~	~	~	~	~	99.70	**12-17-27306**
86.27	~	13.28	~	~	0.17	~	~	~	~	~	~	~	~	~	99.88	**12-17-27306**
86.40	~	13.41	~	~	0.16	~	~	~	~	~	~	~	~	~	100.10	**12-17-27306**
86.21	~	13.33	~	~	0.14	~	~	~	~	~	~	~	~	~	99.85	**12-17-27306**
85.91	~	13.02	~	~	0.17	~	~	~	~	~	~	~	~	~	99.25	**12-17-27306**
86.30	~	13.31	~	~	0.18	~	~	~	~	~	~	~	~	~	100.07	**12-17-27306**
86.62	~	13.60	~	~	0.19	~	~	~	~	~	~	~	~	~	100.61	**12-17-27306**
84.38	~	13.17	~	~	0.24	~	~	~	~	~	~	~	~	~	98.22	**12-17-27306**
86.53	~	13.38	~	~	0.19	~	~	~	~	~	~	~	~	~	100.27	**12-17-27306**

Rhodochrosite

Pb	As	S	Bi	Fe	Sb	Zn	Ag	Cd	Cu	Te	Se	Sn	In	Mn	Total	Sample Number
Galena																
85.36	~	13.51	~	~	0.37	~	~	~	~	~	~	~	~	~	99.50	**12-18-184.50**
84.82	~	13.60	~	~	0.43	~	~	~	~	~	~	~	~	~	99.18	**12-18-184.50**
85.05	~	13.48	~	~	0.36	~	~	~	~	~	~	~	~	~	99.13	**12-18-184.50**
85.32	~	13.58	~	~	0.38	~	0.19	~	~	~	~	~	~	~	99.62	**12-18-184.50**
84.84	~	13.37	~	~	0.35	~	~	~	~	~	~	~	~	~	98.86	**12-18-184.50**
83.99	~	13.41	~	~	0.59	~	0.34	~	~	~	~	~	~	~	98.43	**12-18-184.50**
85.43	~	13.54	~	~	0.41	~	~	~	~	~	~	~	~	~	99.60	**12-18-184.50**
83.96	~	13.60	~	~	1.22	~	1.03	~	~	~	~	~	~	~	99.88	**12-18-184.50**
86.22	~	13.55	~	~	0.40	~	~	~	~	~	~	~	~	~	100.44	**12-18-184.50**
86.68	~	13.49	~	~	0.44	~	0.21	~	~	~	~	~	~	~	100.95	**12-18-184.50**
85.30	~	13.48	~	~	0.58	~	0.38	~	~	~	~	~	~	~	99.89	**12-18-184.50**
86.28	~	13.41	~	~	0.39	~	0.19	~	~	~	~	~	~	~	100.37	**12-18-184.50**
85.61	~	13.67	~	~	0.34	~	~	~	~	~	~	~	~	~	99.92	**12-18-184.50**
85.76	~	13.35	~	~	0.38	~	~	~	~	~	~	~	~	~	99.70	**12-18-184.50**
85.19	~	13.61	~	~	0.81	~	0.65	~	~	~	~	~	~	~	100.35	**12-18-184.50**
86.18	~	13.68	~	~	0.32	~	~	~	~	~	~	~	~	~	100.39	**12-18-184.50**
86.37	~	13.55	~	~	0.34	~	~	~	~	~	~	~	~	~	100.57	**12-18-184.50**
85.72	~	13.58	~	~	0.67	~	0.44	~	~	~	~	~	~	~	100.51	**12-18-184.50**
86.25	~	13.42	~	~	0.39	~	~	~	~	~	~	~	~	~	100.40	**12-18-184.50**
86.22	~	13.45	~	~	0.35	~	~	~	~	~	~	~	~	~	100.17	**12-18-184.50**
86.16	~	13.58	~	~	0.38	~	0.20	~	~	~	~	~	~	~	100.51	**12-18-184.50**
86.04	~	13.51	~	~	0.59	~	0.42	~	~	~	~	~	~	~	100.65	**12-18-184.50**
85.81	~	13.39	~	~	0.41	~	0.21	~	~	~	~	~	~	~	99.97	**12-18-184.50**
86.24	~	13.47	~	~	0.31	~	0.24	~	~	~	~	~	~	~	100.35	**12-18-184.50**
85.55	~	13.61	~	~	0.77	~	0.41	~	~	~	~	~	~	~	100.45	**12-18-184.50**
85.66	~	13.38	~	~	0.41	~	0.23	~	~	~	~	~	~	~	99.74	**12-18-184.50**
86.74	~	13.36	~	~	0.31	~	~	~	~	~	~	~	~	~	100.69	**12-18-184.50**
86.73	~	13.44	~	~	0.34	~	0.22	~	~	~	~	~	~	~	100.82	**12-18-184.50**
86.37	~	13.37	~	~	0.38	~	~	~	~	~	~	~	~	~	100.41	**12-18-184.50**
86.62	~	13.52	~	~	0.43	~	0.27	~	~	~	~	~	~	~	100.93	**12-18-184.50**
86.55	~	13.62	~	~	0.35	~	~	~	~	~	~	~	~	~	100.77	**12-18-184.50**
85.60	~	13.58	~	~	0.41	~	0.23	~	~	~	~	~	~	~	99.86	**12-18-184.50**
86.20	~	13.52	~	~	0.33	~	0.20	~	~	~	~	~	~	~	100.42	**12-18-184.50**
85.86	~	13.57	~	~	0.36	~	0.27	~	~	~	~	~	~	~	100.14	**12-18-184.50**
86.41	~	13.45	~	~	0.42	~	0.25	~	~	~	~	~	~	~	100.64	**12-18-184.50**
84.08	~	13.60	~	~	0.98	~	0.72	~	~	~	~	~	~	~	99.49	**12-18-184.50**
86.01	~	13.51	~	~	0.42	~	~	~	~	~	~	~	~	~	100.28	**12-18-184.50**
84.93	~	13.35	~	~	0.33	~	~	~	~	~	~	~	~	~	98.90	**12-18-184.50**
85.68	~	13.44	~	~	0.32	~	~	~	~	~	~	~	~	~	99.74	**12-18-184.50**
85.26	~	13.38	~	~	0.37	~	~	~	~	~	~	~	~	~	99.26	**12-18-184.50**
84.60	~	13.21	~	~	0.23	~	~	~	~	~	~	~	~	~	98.31	**12-18-184.50**
84.27	~	13.19	~	~	0.29	~	~	~	~	~	~	~	~	~	98.03	**12-18-184.50**
84.73	~	13.38	~	~	0.40	~	~	~	~	~	~	~	~	~	98.83	**12-18-184.50**
84.48	~	13.38	~	~	0.36	~	~	~	~	~	~	~	~	~	98.52	**12-18-184.50**
84.57	~	13.38	~	~	0.35	~	0.23	~	~	~	~	~	~	~	98.63	**12-18-184.50**
84.88	~	13.51	~	~	0.37	~	~	~	~	~	~	~	~	~	99.11	**12-18-184.50**
85.33	~	13.45	~	~	0.38	~	0.27	~	~	~	~	~	~	~	99.64	**12-18-184.50**
85.69	~	13.52	~	~	0.40	~	0.26	~	~	~	~	~	~	~	99.92	**12-18-184.50**
84.43	~	13.37	~	~	0.39	~	0.23	~	~	~	~	~	~	~	98.50	**12-18-184.50**
84.41	~	13.67	~	~	1.11	~	0.80	~	~	~	~	~	~	~	100.05	**12-18-184.50**
85.02	~	13.48	~	~	0.43	~	0.21	~	~	~	~	~	~	~	99.32	**12-18-184.50**
85.17	~	13.51	~	~	0.32	~	0.21	~	~	~	~	~	~	~	99.34	**12-18-184.50**
84.54	~	13.45	~	~	0.43	~	0.21	~	~	~	~	~	~	~	98.74	**12-18-184.50**
84.37	~	13.42	~	~	0.34	~	0.20	~	~	~	~	~	~	~	98.46	**12-18-184.50**
85.52	~	13.47	~	~	0.45	~	0.33	~	~	~	~	~	~	~	99.99	**12-18-184.50**
85.00	~	13.63	~	~	0.54	~	0.37	~	~	~	~	~	~	~	99.65	**12-18-184.50**
85.33	~	13.44	~	~	0.33	~	0.21	~	~	~	~	~	~	~	99.40	**12-18-184.50**
84.99	~	13.39	~	~	0.39	~	0.23	~	~	~	~	~	~	~	99.10	**12-18-184.50**
84.92	~	13.32	~	~	0.38	~	~	~	~	~	~	~	~	~	98.90	**12-18-184.50**
85.09	~	13.55	~	~	0.38	~	0.22	~	~	~	~	~	~	~	99.31	**12-18-184.50**
85.38	~	13.55	~	~	0.57	~	0.31	~	~	~	~	~	~	~	99.97	**12-18-184.50**
84.84	~	13.46	~	~	0.36	~	~	~	~	~	~	~	~	~	98.94	**12-18-184.50**

Appendix 2.1 shows galena data for both calcite and rhodochrosite ore stages. All data in wt.% unless otherwise stated. “~” symbol representative of data below detection

	85.43	~	13.51	~	~	0.31	~	~	~	~	~	~	~	~	~	99.45	**12-18-184.50**
	85.56	~	13.42	~	~	0.39	~	~	~	~	~	~	~	~	~	99.67	**12-18-184.50**
	84.55	~	13.36	~	~	0.34	~	0.22	~	~	~	~	~	~	~	98.51	**12-18-184.50**
	84.66	~	13.41	~	~	0.37	~	0.22	~	~	~	~	~	~	~	98.81	**12-18-184.50**
	84.60	~	13.36	~	~	0.39	~	~	~	~	~	~	~	~	~	98.60	**12-18-184.50**
	85.01	~	13.49	~	~	0.38	~	~	~	~	~	~	~	~	~	99.13	**12-18-184.50**
	85.99	~	13.37	~	~	0.30	~	~	~	~	~	~	~	~	~	99.85	**12-18-184.50**
	85.74	~	13.56	~	~	0.42	~	0.21	~	~	~	~	~	~	~	100.15	**12-18-184.50**
	85.83	~	13.58	~	~	0.38	~	0.20	~	~	~	~	~	~	~	100.09	**12-18-184.50**
	85.67	~	13.57	0.30	0.39	~	~	~	~	~	~	~	~	~	~	100.19	**12-17-13792**
	85.14	~	13.46	0.89	0.75	~	~	0.34	~	~	~	~	~	~	~	100.76	**12-17-13792**
	85.34	~	13.65	0.82	0.80	~	~	0.36	~	~	~	~	~	~	~	101.15	**12-17-13792**
	85.96	~	13.69	0.28	0.90	~	~	~	~	~	~	~	~	~	~	101.14	**12-17-13792**
Detection Limits																	
	Pb	**As**	**S**	**Bi**	**Fe**	**Sb**	**Zn**	**Ag**	**Cd**	**Cu**	**Te**	**Se**	**Sn**	**In**	**Mn**		
	0.29	0.08	0.09	0.17	0.07	0.11	0.07	0.19	0.22	0.11	~	~	~	~	~		
Calcite																	
	Pb	**As**	**S**	**Bi**	**Fe**	**Sb**	**Zn**	**Ag**	**Cd**	**Cu**	**Te**	**Se**	**Sn**	**In**	**Mn**	**Total**	**Sample Number**
Pyrrhotite																	
	~	~	39.78	~	60.21	~	~	~	~	~	~	~	~	~	~	100.21	**12-17-13792**
	~	~	40.24	~	60.03	~	~	~	~	~	~	~	~	~	~	100.51	**12-17-13792**
	~	~	40.53	~	60.16	~	~	~	~	~	~	~	~	~	~	100.91	**12-17-13792**
	~	~	39.93	~	60.11	~	~	~	~	~	~	~	~	~	~	100.41	**12-17-13792**
	~	~	40.15	~	60.15	~	~	~	~	~	~	~	~	~	~	100.59	**12-17-13792**
	~	~	39.54	~	60.33	~	~	~	~	~	~	~	~	~	~	100.08	**12-17-13792**
	~	~	40.06	~	60.11	~	~	~	~	~	~	~	~	~	~	100.24	**12-17-13792**
	~	~	39.16	~	60.58	~	~	~	~	~	~	~	~	~	~	99.92	**12-17-13792**
	~	~	39.06	~	60.74	~	~	~	~	~	~	~	~	~	~	100.06	**12-17-13792**
	~	~	38.37	~	60.16	~	~	~	~	~	~	~	~	~	~	98.78	**12-17-27306**
	~	~	38.52	~	60.15	~	~	~	~	~	~	~	~	~	~	98.86	**12-17-27306**
Sphalerite																	
	~	~	33.45	~	10.30	~	54.50	~	~	0.16	~	~	~	~	0.26	98.87	**12-17-27306**
	~	~	33.50	~	9.64	~	55.23	~	~	~	~	~	~	~	0.31	98.96	**12-17-27306**
	~	~	32.92	~	8.24	~	57.36	~	~	~	~	~	~	~	0.16	98.93	**12-17-27306**
	~	~	33.12	~	9.30	~	56.07	~	~	~	~	~	~	~	0.27	99.00	**12-17-27306**
	~	~	33.56	~	11.33	~	54.19	~	~	~	~	~	~	~	0.34	99.66	**12-17-27306**
	~	~	33.89	~	11.23	~	56.55	~	~	0.22	~	~	~	~	0.31	102.32	**12-17-27306**
	~	~	33.64	~	11.02	~	55.05	~	~	~	~	~	~	~	0.30	100.23	**12-17-27306**
	~	~	33.41	~	9.84	~	55.68	~	~	~	~	~	~	~	0.27	99.39	**12-17-27306**
	~	~	33.79	~	10.74	~	54.12	~	~	~	~	~	~	~	0.43	99.33	**12-17-27306**
	~	~	33.46	~	10.76	~	54.56	~	~	0.12	~	~	~	~	0.29	99.27	**12-17-27306**
Rhodochrosite																	
	Pb	**As**	**S**	**Bi**	**Fe**	**Sb**	**Zn**	**Ag**	**Cd**	**Cu**	**Te**	**Se**	**Sn**	**In**	**Mn**	**Total**	**Sample Number**
Pyrite																	
	~	~	52.73	~	45.62	~	~	~	~	0.08	~	~	~	~	~	98.53	**12-17-13792**
	~	~	52.71	~	45.52	~	~	~	~	0.05	~	~	~	~	~	98.40	**12-17-13792**
	~	~	52.93	~	45.29	~	~	~	~	0.07	~	~	~	~	~	98.51	**12-17-13792**
	~	~	52.75	~	45.67	~	~	~	~	0.09	~	~	~	~	~	98.64	**12-17-13792**
	~	~	52.82	~	45.72	~	~	~	~	0.11	~	~	~	~	~	98.76	**12-17-13792**
	~	~	52.85	~	45.64	~	~	~	~	0.08	~	~	~	~	~	98.70	**12-17-13792**
	~	~	52.84	~	45.66	~	~	~	~	0.07	~	~	~	~	~	98.68	**12-17-13792**
	~	~	52.40	~	46.56	~	~	~	~	0.02	~	~	~	~	~	99.36	**12-17-13792**
	~	~	53.46	~	46.65	~	~	~	~	0.05	~	~	~	~	~	100.39	**12-17-13792**
	~	~	53.05	~	46.60	~	~	~	~	0.05	~	~	~	~	~	100.02	**12-17-13792**
	~	~	53.60	~	46.76	~	~	~	~	0.05	~	~	~	~	~	100.59	**12-17-13792**
	~	~	53.49	~	46.72	~	~	~	~	0.04	~	~	~	~	~	100.40	**12-17-13792**
	~	~	52.91	~	45.74	~	~	~	~	0.07	~	~	~	~	~	98.83	**12-17-13792**
	~	~	53.11	~	46.78	~	~	~	~	0.04	~	~	~	~	~	100.16	**12-17-13792**
	~	~	53.56	~	46.76	~	~	~	~	0.04	~	~	~	~	~	100.45	**12-17-13792**
Chalcopyrite																	
	~	~	34.85	~	30.74	~	~	~	~	33.13	~	~	~	~	~	99.09	**12-18-184.50**
	~	~	35.30	~	30.83	~	~	~	~	33.23	~	~	~	~	~	99.70	**12-18-184.50**
	~	~	35.65	~	30.60	~	~	~	~	33.30	~	~	~	~	~	100.01	**12-18-184.50**
	~	~	34.82	~	30.32	~	~	~	~	33.47	~	~	~	~	~	98.88	**12-18-184.50**
	~	~	35.01	~	29.32	~	2.61	~	~	32.19	~	~	~	~	~	99.39	**12-18-184.50**
Sphalerite																	
	~	~	34.81	~	13.48	~	51.16	~	~	~	~	~	~	~	1.05	100.90	**12-18-184.50**
	~	~	34.35	~	13.46	~	51.05	~	~	~	~	~	~	~	1.32	100.53	**12-18-184.50**
	~	~	34.83	~	13.12	~	51.41	~	~	~	~	~	~	~	0.93	100.55	**12-18-184.50**
	~	~	34.57	~	13.73	~	51.09	~	~	~	~	~	~	~	0.93	100.62	**12-18-184.50**
	~	~	34.48	~	13.32	~	51.47	~	~	~	~	~	~	~	0.88	100.53	**12-18-184.50**
	~	~	34.52	~	14.16	~	50.24	~	~	~	~	~	~	~	1.06	100.30	**12-18-184.50**
	~	~	34.52	~	13.67	~	50.78	~	~	~	~	~	~	~	1.01	100.38	**12-18-184.50**
	~	~	34.60	~	13.65	~	50.86	~	~	~	~	~	~	~	1.06	100.52	**12-18-184.50**
	~	~	34.70	~	15.45	~	49.01	~	~	~	~	~	~	~	1.21	100.67	**12-18-184.50**
	~	~	34.57	~	14.06	~	50.15	~	~	~	~	~	~	~	1.24	100.26	**12-18-184.50**
	~	~	34.61	~	13.77	~	50.55	~	~	~	~	~	~	~	1.16	100.48	**12-18-184.50**
	~	~	34.58	~	13.94	~	50.03	~	~	~	~	~	~	~	1.48	100.33	**12-18-184.50**
	~	~	34.23	~	13.50	~	50.66	~	~	~	~	~	~	~	1.43	100.14	**12-18-184.50**
	~	~	34.59	~	14.06	~	49.94	~	~	~	~	~	~	~	1.36	100.30	**12-18-184.50**
	~	~	34.69	~	14.21	~	50.17	~	~	~	~	~	~	~	1.34	100.79	**12-18-184.50**
	~	~	34.16	~	11.43	~	53.98	~	~	~	~	~	~	~	0.47	100.31	**12-18-184.50**
	~	~	34.06	~	12.20	~	53.37	~	~	~	~	~	~	~	0.48	100.37	**12-18-184.50**

Appendix 2.1 cont, Appendix 1.2 shows all data for sulfides other than galena. All data in wt.% unless otherwise stated. “~” symbol representative of data below limits of detection

~	~	34.13	~	11.40	~	54.12	~	~	~	~	~	~	~	0.46	100.42	**12-18-184.50**
~	~	34.47	~	11.97	~	53.29	~	~	~	~	~	~	~	0.48	100.46	**12-18-184.50**
~	~	34.12	~	9.05	~	56.71	~	~	~	~	~	~	~	0.36	100.57	**12-18-184.50**
~	~	33.94	~	8.93	~	56.65	~	~	~	~	~	~	~	0.33	100.23	**12-18-184.50**
~	~	34.23	~	10.85	~	55.16	~	~	~	~	~	~	~	0.35	100.85	**12-18-184.50**
~	~	34.10	~	10.78	~	55.33	~	~	~	~	~	~	~	0.29	100.74	**12-18-184.50**
~	~	34.05	~	13.98	~	51.01	~	~	~	~	~	~	~	1.17	100.44	**12-18-184.50**
~	~	34.77	~	15.40	~	48.76	~	~	~	~	~	~	~	1.32	100.55	**12-18-184.50**
~	~	34.05	~	13.89	~	50.94	~	~	~	~	~	~	~	1.07	100.22	**12-18-184.50**
~	~	34.49	~	13.96	~	50.73	~	~	~	~	~	~	~	1.08	100.53	**12-18-184.50**
~	~	34.43	~	13.84	~	50.94	~	~	~	~	~	~	~	1.07	100.60	**12-18-184.50**
~	~	34.50	~	13.94	~	50.77	~	~	~	~	~	~	~	1.08	100.45	**12-18-184.50**
~	~	34.49	~	13.88	~	50.62	~	~	~	~	~	~	~	1.07	100.24	**12-18-184.50**
~	~	33.79	~	13.69	~	51.09	~	~	~	~	~	~	~	1.01	99.86	**12-18-184.50**
~	~	34.02	~	12.72	~	52.13	~	~	~	~	~	~	~	0.77	99.96	**12-18-184.50**
~	~	33.97	~	12.60	~	52.52	~	~	~	~	~	~	~	0.76	100.25	**12-18-184.50**
~	~	34.25	~	12.70	~	51.94	~	~	~	~	~	~	~	0.79	100.03	**12-18-184.50**
~	~	34.02	~	13.65	~	51.19	~	~	~	~	~	~	~	1.01	100.19	**12-18-184.50**
~	~	34.62	~	11.41	~	54.38	~	~	~	~	~	~	~	0.33	101.11	**12-18-184.50**
~	~	34.37	~	13.32	~	51.44	~	~	~	~	~	~	~	0.92	100.22	**12-18-184.50**
~	~	34.37	~	11.84	~	53.65	~	~	~	~	~	~	~	0.51	100.72	**12-18-184.50**
~	~	34.17	~	13.05	~	52.15	~	~	~	~	~	~	~	0.87	100.60	**12-18-184.50**
~	~	34.66	~	11.32	~	54.14	~	~	~	~	~	~	~	0.34	100.63	**12-18-184.50**
~	~	34.33	~	12.13	~	52.86	~	~	~	~	~	~	~	0.62	100.24	**12-18-184.50**
~	~	34.48	~	12.18	~	52.88	~	~	~	~	~	~	~	0.71	100.57	**12-18-184.50**
~	~	34.14	~	12.05	~	52.92	~	~	~	~	~	~	~	0.77	100.11	**12-18-184.50**
~	~	34.58	~	11.65	~	52.66	~	~	~	~	~	~	~	0.69	99.83	**12-18-184.50**
~	~	34.14	~	13.37	~	51.03	~	~	~	~	~	~	~	1.12	99.89	**12-18-184.50**
~	~	34.63	~	13.89	~	49.98	~	~	~	~	~	~	~	1.46	100.18	**12-18-184.50**
~	~	34.20	~	13.36	~	51.70	~	~	~	~	~	~	~	0.93	100.55	**12-18-184.50**
~	~	34.56	~	13.36	~	50.70	~	~	~	~	~	~	~	1.43	100.34	**12-18-184.50**
~	~	34.38	~	11.83	~	53.74	~	~	~	~	~	~	~	0.46	100.68	**12-18-184.50**
~	~	34.15	~	10.81	~	54.58	~	~	~	~	~	~	~	0.42	100.20	**12-18-184.50**
~	~	34.26	~	10.69	~	54.81	~	~	~	~	~	~	~	0.42	100.45	**12-18-184.50**
~	~	34.57	~	10.80	~	54.03	~	~	~	~	~	~	~	0.40	100.03	**12-18-184.50**
~	~	34.23	~	9.99	~	55.79	~	~	~	~	~	~	~	0.37	100.84	**12-18-184.50**
~	~	34.60	~	9.60	~	56.23	~	~	~	~	~	~	~	0.36	101.04	**12-18-184.50**
~	~	34.02	~	10.69	~	54.58	~	~	~	~	~	~	~	0.41	99.99	**12-18-184.50**
~	~	34.24	~	9.95	~	55.93	~	~	~	~	~	~	~	0.34	100.68	**12-18-184.50**
~	~	34.45	~	10.48	~	54.98	~	~	~	~	~	~	~	0.42	100.66	**12-18-184.50**
~	~	34.74	~	10.17	~	55.32	~	~	~	~	~	~	~	0.40	100.84	**12-18-184.50**
~	~	34.32	~	10.08	~	55.20	~	~	~	~	~	~	~	0.38	100.24	**12-18-184.50**
~	~	34.29	~	11.33	~	53.98	~	~	~	~	~	~	~	0.44	100.26	**12-18-184.50**
~	~	34.48	~	11.80	~	53.53	~	~	~	~	~	~	~	0.48	100.56	**12-18-184.50**
~	~	34.76	~	12.41	~	52.80	~	~	~	~	~	~	~	0.40	100.67	**12-18-184.50**
~	~	34.42	~	10.97	~	54.34	~	~	~	~	~	~	~	0.34	100.35	**12-18-184.50**
~	~	33.70	~	10.95	~	54.63	~	~	~	~	~	~	~	0.43	99.88	**12-18-184.50**
~	~	34.03	~	9.57	~	56.36	~	~	~	~	~	~	~	0.35	100.46	**12-18-184.50**
~	~	34.03	~	9.75	~	56.18	~	~	~	~	~	~	~	0.38	100.59	**12-18-184.50**
Freibergite																
~	~	21.92	~	4.91	26.33	1.40	29.92	~	16.10	~	~	~	~	~	100.73	**12-18-184.50**
~	~	21.76	~	4.44	26.27	1.88	30.11	~	15.99	~	~	~	~	~	100.62	**12-18-184.50**
~	~	21.89	~	5.06	26.31	1.30	29.03	~	16.45	~	~	~	~	~	100.13	**12-18-184.50**
~	~	21.87	~	5.50	26.38	0.80	28.20	~	17.11	~	~	~	~	~	100.00	**12-18-184.50**
~	~	22.23	~	5.50	26.47	0.89	27.28	~	17.54	~	~	~	~	~	100.02	**12-18-184.50**
~	~	23.87	~	5.44	27.38	1.25	19.00	~	23.58	~	~	~	~	~	100.62	**12-18-184.50**
~	~	23.63	~	5.49	27.12	1.22	19.44	~	23.37	~	~	~	~	~	100.33	**12-18-184.50**
~	~	22.04	~	5.60	26.09	0.57	29.96	~	15.35	~	~	~	~	~	99.66	**12-18-184.50**
~	~	22.37	~	5.60	26.38	0.66	28.10	~	16.83	~	~	~	~	~	100.09	**12-18-184.50**
~	~	21.62	~	5.29	26.21	1.00	29.98	~	16.15	~	~	~	~	~	100.39	**12-18-184.50**
~	~	20.98	~	4.74	26.14	1.46	33.03	~	13.87	~	~	~	~	~	100.26	**12-18-184.50**
~	~	21.77	~	5.21	26.28	1.18	29.82	~	16.18	~	~	~	~	~	100.62	**12-18-184.50**
~	~	21.36	~	5.31	26.36	0.93	30.52	~	15.62	~	~	~	~	~	100.22	**12-18-184.50**
~	~	22.04	~	5.81	25.71	0.51	32.28	~	13.21	~	~	~	~	0.10	99.71	**12-18-184.50**
Arsenopyrite																
~	43.97	21.25	~	35.56	~	~	~	~	~	~	~	~	~	~	101.49	**12-18-184.50**
Solid Solution Sample																
~	~	33.04	~	11.16	0.33	53.40	0.82	~	0.21	~	~	~	~	0.35	99.42	**12-18-18054b**
~	~	33.33	~	11.14	~	54.83	~	~	~	~	~	~	~	0.35	99.88	**12-18-18054b**
~	~	33.40	~	11.18	~	54.65	~	~	~	~	~	~	~	0.33	99.78	**12-18-18054b**
~	~	31.23	~	10.53	3.68	44.73	6.82	~	1.84	~	~	~	~	0.31	99.19	**12-18-18054b**
~	~	30.77	~	10.64	4.79	41.85	8.49	~	2.28	~	~	~	~	0.33	99.19	**12-18-18054b**
~	~	30.35	~	10.35	5.40	40.62	9.44	~	2.36	~	~	~	~	0.28	98.83	**12-18-18054b**
~	~	31.82	~	11.16	2.86	46.71	5.36	~	1.33	~	~	~	~	0.34	99.64	**12-18-18054b**
~	~	32.53	~	11.26	1.58	47.25	3.15	~	3.35	~	~	~	~	0.31	99.46	**12-18-18054b**
~	~	30.32	~	7.29	5.62	44.13	9.31	~	2.58	~	~	~	~	0.52	99.82	**12-18-18054b**
~	~	32.10	~	10.36	2.28	49.70	4.34	~	1.11	~	~	~	~	0.23	100.14	**12-18-18054b**
~	~	33.33	~	10.89	~	55.17	~	~	~	~	~	~	~	0.31	99.86	**12-18-18054b**
~	~	31.41	~	9.88	3.62	46.19	6.20	~	3.12	~	~	~	~	0.25	100.71	**12-18-18054b**
~	~	33.40	~	10.93	~	55.19	0.03	~	~	~	~	~	~	0.26	100.04	**12-18-18054b**
~	~	31.28	~	6.88	3.92	48.48	6.86	~	2.03	~	~	~	~	0.22	99.69	**12-18-18054b**
~	~	31.77	~	8.71	2.60	48.39	4.83	~	2.49	~	~	~	~	0.64	99.46	**12-18-18054b**

Appendix 2.2 cont.

~	~	33.13	~	9.83	~	55.14	~	~	~	~	~	~	~	1.31	99.82	**12-18-18054b**
~	~	21.68	~	6.17	25.84	1.45	28.91	~	16.87	~	~	~	~	0.06	100.99	**12-18-18054b**
~	~	27.85	~	7.36	9.58	32.84	17.47	~	4.79	~	~	~	~	0.11	100.05	**12-18-18054b**
~	~	29.98	~	8.73	5.89	41.04	10.77	~	3.14	~	~	~	~	0.12	99.69	**12-18-18054b**

Detection Limits

Pb	As	S	Bi	Fe	Sb	Zn	Ag	Cd	Cu	Te	Se	Sn	In	Mn
~	0.09	0.03	0.2	0.06	0.09	0.11	0.09	0.22	0.11	~	~	~	~	0.05

Appendix 2.2 cont. shows detection limits for all sulfides excepting galena

Appendix 3 – Isotopic Data

Alteration facies	$\delta^{13}C_{PDB}$ (‰)	$\delta^{18}O_{SMOW}$ (‰)	Sample #	Temperature from FIA (°C)	$\delta^{13}C_{Fluid}$ (‰)	$\delta^{18}O_{Fluid}$ (‰)
Calcite	-5.50	2.75	**16-6053**	240.0	-9.51	-4.92
Calcite	-9.00	1.04	**16-7439**	240.0	-13.01	-6.63
Calcite	-6.60	0.73	**16-17587**	240.0	-10.61	-6.94
Calcite	2.80	1.39	**16-18540**	240.0	-1.21	-6.28
Calcite	-5.20	0.38	**17-5819**	240.0	-9.21	-7.29
Calcite	-6.80	5.10	**17-13792**	240.0	-10.81	-2.57
Calcite	-3.00	1.46	**17-18300**	240.0	-7.01	-6.21
Calcite	-3.40	2.01	**17-27129**	240.0	-7.41	-5.66
Calcite	1.90	-1.70	**19-12155**	240.0	-2.11	-9.37
Calcite	-6.80	4.20	**19-22717**	240.0	-10.81	-3.47
Calcite	-2.40	2.57	**16-1407**	240.0	-6.41	-5.10
Calcite	-2.20	-1.71	**16-25082**	240.0	-6.21	-9.38
Calcite	-5.30	-1.20	**19-19886**	240.0	-9.31	-8.87
Quartz I	~	11.63	**12-18-18450**	270.0	~	3.07
Quartz I	~	10.94	**12-16-25876**	282.0	~	2.94
Quartz I	~	5.19	**12-19-17261**	282.0	~	-2.89
Quartz I	~	5.01	**12-17-19204**	282.0	~	-3.06
Quartz I	~	4.96	**12-16-26000**	282.0	~	-3.12
Quartz I	~	2.67	**12-18-18054**	270.0	~	-5.89
Quartz II	~	10.94	**12-16-25876**	200.0	~	-1.27
Quartz II	~	10.08	**12-16-7043**	200.0	~	-2.13
Quartz II	~	8.59	**12-17-8269G**	200.0	~	-4.98
Quartz II	~	7.35	**12-17-8269B**	180.0	~	-6.22
Quartz II	~	6.90	**12-17-8269C**	180.0	~	-6.67
Quartz II	~	6.70	**12-20-21162**	200.0	~	-5.50
Quartz II	~	6.32	**12-17-8269F**	180.0	~	-7.25
Quartz II	~	5.52	**12-20-16757**	200.0	~	-6.69
Quartz II	~	5.47	**12-17-8269D**	180.0	~	-8.10
Quartz II	~	4.37	**12-17-8269A**	180.0	~	-8.99
Quartz II	~	4.05	**12-16-27488**	200.0	~	-8.16
Rhodochrosite	-7.40	7.82	**12-17-11098**	275.0	-1.93	2.31
Rhodochrosite	-7.60	7.50	**12-17-19204**	275.0	-2.13	1.99
Rhodochrosite	-7.40	7.21	**12-17-19204a**	275.0	-1.93	1.70
Rhodochrosite	-6.80	8.46	**12-17-27129a**	275.0	-1.33	2.95
Rhodochrosite	-6.40	4.32	**12-17-27306**	275.0	-0.93	-1.19
Rhodochrosite	-7.60	7.47	**12-18-18035**	275.0	-2.13	1.96
Rhodochrosite	-7.70	7.48	**12-18-18035a**	275.0	-2.23	1.97
Rhodochrosite	-7.30	9.08	**12-18-18054**	275.0	-1.83	3.57
Rhodochrosite	-6.80	6.06	**12-20-19800**	275.0	-1.33	0.55

Appendix 3.1 showing data for C and O isotopes in both carbonate phases and O isotopic data for quartz. Also present is the temperature corrected isotopic composition of fluid from which the minerals formed. Quartz I is ore stage quartz, quartz II is oxide stage quartz

Sr Isotopes

Sample Number	**Mineral**	**$^{87}Sr/^{86}Sr$**	**Errors**
12-16-25082	*Rhodochrosite*	**0.747601**	0.000023
12-17-13792	*Calcite*	**0.736799**	0.000043
12-17-18300	*Rhodochrosite*	**0.738381**	0.000021
12-19-12155	*Rhodochrosite*	**0.737988**	0.000027
12-19-19886	*Calcite*	**0.735840**	0.000028
12-17-19204	*Calcite*	**0.736323**	0.000089
12-17-27306	*Calcite*	**0.738989**	0.000029
12-18-18035	*Rhodochrosite*	**0.755782**	0.000074
12-18-18054	*Rhodochrosite*	**0.755759**	0.000070
12-18-18450	*Rhodochrosite*	**0.737116**	0.000071

S isotopes

Sample Number	**Sample**	**$\delta^{34}S$(‰)**
12-18-18450	Galena	9.1
12-18-18450	Galena	10.2
12-18-18450	Sphalerite	11.2
12-16-1470	Sphalerite	10.1
12-16-1354	Sphalerite	10.1

Appendix 3.2 Sr isotopic data for calcite, rhodochrosite samples and S isotopic data for galena and sphalerite. Sulfur isotopic data is displayed in ‰.

Appendix 4 – Whole Rock Geochemistry Data

SiO2	Al2O3	Fe2O3(T)	MnO	MgO	CaO	Na2O	K2O	TiO2	P2O5	LOI	Total	Au	Ag	As	Ba	Be	Bi	Br	Cd	Co	Cr	Element/Molecule
%	%	%	%	%	%	%	%	%	%	%	%	ppb	ppm	ppm	ppm	ppm	ppm	ppm	ppm	ppm	ppm	Unit Symbol
67.5	15.2	2.18	0.03	1.08	2.93	3.09	4.73	0.37	0.15	2.08	99.3	< 1	< 0.5	< 1	550	5	0.2	< 0.5	< 0.5	3.1	16.1	HAM12-20 83.22
70.3	15	2.21	0.04	0.95	2.48	3.26	4.56	0.37	0.14	1.67	101	< 1	< 0.5	< 1	633	5	0.5	< 0.5	< 0.5	3.4	28.6	HAM12-20 94.40
70.1	15	2.23	0.04	0.83	2.21	3.2	4.44	0.4	0.15	1.27	99.9	< 1	< 0.5	< 1	590	6	0.4	< 0.5	< 0.5	4	25.7	HAM12-20 88.86
68.2	15.3	2.18	0.04	0.86	2.27	3.24	4.74	0.39	0.16	0.97	98.3	< 1	< 0.5	< 1	631	6	0.9	< 0.5	< 0.5	3.4	23.7	HAM12-20 77.63
68.2	15.2	2.38	0.04	0.9	2.23	3.14	4.77	0.41	0.16	1.04	98.5	< 1	< 0.5	< 1	612	5	0.2	< 0.5	< 0.5	4.9	25.3	HAM12-20 100.29
69.1	14.8	2.2	0.04	0.84	2.14	3.25	4.65	0.37	0.13	1.29	98.8	< 1	< 0.5	< 1	657	5	0.4	< 0.5	< 0.5	2.9	24.5	HAM12-20 13.26
70.3	15.4	2.18	0.05	0.79	2.04	3.19	4.71	0.37	0.13	1.37	101	< 1	< 0.5	< 1	702	5	0.5	< 0.5	< 0.5	4	24.4	HAM12-20 86.30
69.6	15	2.32	0.04	0.79	2.03	3.23	4.38	0.37	0.12	1.6	99.5	< 1	< 0.5	< 1	632	6	0.3	< 0.5	< 0.5	3.6	31.1	HAM12-20 17.52
75.3	14	0.74	0.09	0.16	0.76	3.15	4.44	0.03	0.26	1.23	100	< 1	< 0.5	< 1	79	20	0.9	< 0.5	< 0.5	1.2	22.1	HAM12-20 201.01
0.01	**0.01**	**0.01**	**0**	**0.01**	**0.01**	**0.01**	**0.01**	**0**	**0.01**		**0.01**	**1**	**0.5**	**1**	**1**	**1**	**0.1**	**0.5**	**0.5**	**0.1**	**0.5**	**Detection Limit**

Cs	Cu	Ga	Ge	Hf	Hg	In	Ir	Mo	Nb	Ni	Pb	Rb	S	Sb	Sc	Se	Sn	Sr	Ta	Th	U	Element
ppm	ppm	ppm	ppm	ppm	ppm	ppm	ppb	ppm	ppm	ppm	ppm	ppm	%	ppm	ppm	ppm	ppm	ppm	ppm	ppm	ppm	Unit Symbol
7.5	2	23	1.3	3.3	< 1	< 0.1	< 1	< 2	9.2	3	43	229	0.01	0.4	5.06	< 0.5	6	228	1.67	26.9	5.81	HAM12-20 83.22
4.6	1	25	1.4	4.1	< 1	< 0.1	< 1	< 2	10.9	4	42	204	0.01	0.7	4.78	< 0.5	6	224	0.98	25.4	4.19	HAM12-20 94.40
6.9	2	25	1.3	3.8	< 1	< 0.1	< 1	< 2	10.4	4	44	216	0.01	0.6	4.99	< 0.5	6	228	1.26	27.3	6.72	HAM12-20 88.86
12.5	1	24	1.4	3.3	< 1	< 0.1	< 1	< 2	9.9	4	42	246	0.01	0.8	4.86	< 0.5	7	229	1.32	24.2	7.65	HAM12-20 77.63
7.1	2	25	1.3	3.7	< 1	< 0.1	< 1	< 2	10.3	4	42	245	0	0.1	5.53	< 0.5	6	230	1.57	30.3	5.89	HAM12-20 100.29
7	2	25	1.5	3.9	< 1	< 0.1	< 1	< 2	9.1	4	44	211	0	< 0.1	5.06	< 0.5	6	228	0.83	24.4	3.75	HAM12-20 13.26
7	5	24	1.4	3.8	< 1	< 0.1	< 1	< 2	10.8	4	46	222	0.01	0.6	5.02	< 0.5	6	246	1.16	23.4	9	HAM12-20 86.30
5.1	5	24	1.4	3.7	< 1	< 0.1	< 1	< 2	7.3	6	47	180	0	0.8	5.13	< 0.5	5	239	0.57	22.5	3.65	HAM12-20 17.52
17.4	6	22	3.2	0.9	< 1	< 0.1	< 1	< 2	12.1	< 1	15	394	0.02	0.7	1.1	< 0.5	25	31	6.56	1.11	11.4	HAM12-20 201.01
0.1	**1**	**1**	**0.5**	**0.1**	**1**	**0.1**	**1**	**2**	**0.2**	**1**	**5**	**1**	**0**	**0.1**	**0.01**	**0.5**	**1**	**2**	**0.01**	**0.05**	**0.01**	**Detection Limit**

V	W	Y	Zn	Zr	La	Ce	Pr	Nd	Sm	Eu	Gd	Tb	Dy	Ho	Er	Tl	Tm	Yb	Lu	Mass	Element
ppm	ppm	ppm	ppm	ppm	ppm	ppm	ppm	ppm	ppm	ppm	ppm	ppm	ppm	ppm	ppm	ppm	ppm	ppm	ppm	g	Unit Symbol
31	< 1	10	97	141	50	106	12	40.8	6.58	0.87	3.26	0.38	1.95	0.34	0.98	1.33	0.15	0.88	0.14	1.65	HAM12-20 83.22
31	< 1	9	54	151	51.1	108	12.1	41.2	6.54	0.9	3.73	0.4	1.95	0.33	0.93	0.99	0.14	0.9	0.15	1.71	HAM12-20 94.40
34	< 1	10	36	167	52.5	110	12.4	42.8	6.56	0.89	3.25	0.35	1.89	0.35	1	1.36	0.15	0.84	0.13	1.68	HAM12-20 88.86
33	< 1	11	105	150	48	99.4	11	37.3	5.91	0.85	2.8	0.35	1.89	0.37	1.07	1.61	0.15	0.91	0.12	1.82	HAM12-20 77.63
37	< 1	12	76	161	58.3	122	13.7	46.6	7.19	0.92	3.42	0.4	2.25	0.41	1.19	1.49	0.16	0.83	0.12	1.59	HAM12-20 100.29
32	< 1	10	92	150	49.7	104	11.5	39.5	6.16	0.95	3.65	0.41	2.08	0.39	1.15	1.11	0.17	1.07	0.16	1.87	HAM12-20 13.26
33	< 1	9	67	154	46.5	97.2	10.9	37.5	6.31	0.97	3.21	0.31	1.67	0.31	0.92	1.52	0.13	0.78	0.12	1.85	HAM12-20 86.30
34	< 1	9	91	152	45.8	94.2	10.5	36.6	6.14	0.94	3.11	0.32	1.59	0.3	0.91	1.17	0.13	0.81	0.11	1.79	HAM12-20 17.52
5	< 1	3	77	22	2.85	6.05	0.66	2.32	0.58	0.1	0.31	0.05	0.32	0.06	0.18	2.16	0.04	0.28	0.04	1.84	HAM12-20 201.01
5	**1**	**1**	**1**	**1**	**0.05**	**0.05**	**0.01**	**0.05**	**0.01**	**0.01**	**0.01**	**0.01**	**0.01**	**0.01**	**0.01**	**0.05**	**0.01**	**0.01**	**0**		**Detection Limit**

Appendix 4.1 Whole rock data for the Anvil Suite Granite, data below detection limits is shown by <1. Element name and unit of measurement is given at the top of each column

Element	Y	La	Ce	Pr	Nd	Sm	Eu	Gd	Tb	Dy	Ho	Er	Tm	Yb	Lu
HAM12-20 83.22	6.37	210.97	172.92	129.31	89.28	44.46	15.38	16.38	10.53	7.93	6.23	6.13	5.87	5.47	5.57
HAM12-20 94.40	5.73	215.61	176.18	130.39	90.15	44.19	15.95	18.74	11.08	7.93	6.04	5.81	5.55	5.59	6.06
HAM12-20 88.86	6.37	221.52	179.45	133.62	93.65	44.32	15.83	16.33	9.70	7.68	6.41	6.25	5.87	5.22	5.16
HAM12-20 77.63	7.01	202.53	162.15	118.53	81.62	39.93	15.03	14.07	9.70	7.68	6.78	6.69	6.03	5.65	5.00
HAM12-20 100.29	7.64	245.99	199.02	147.63	101.97	48.58	16.38	17.19	11.08	9.15	7.51	7.44	6.28	5.16	4.76
HAM12-20 13.26	6.37	209.70	169.66	123.92	86.43	41.62	16.86	18.34	11.36	8.46	7.14	7.19	6.72	6.65	6.63
HAM12-20 86.30	5.73	196.20	158.56	117.46	82.06	42.64	17.23	16.13	8.59	6.79	5.68	5.75	5.34	4.84	4.67
HAM12-20 17.52	5.73	193.25	153.67	113.15	80.09	41.49	16.70	15.63	8.86	6.46	5.49	5.69	5.22	5.03	4.59
HAM12-20 201.01	1.91	12.03	9.87	7.11	5.08	3.92	1.79	1.56	1.39	1.30	1.10	1.13	1.50	1.74	1.71

Element	Cs	Rb	Ba	Th	U	Nb	Ta	K	La	Ce	Pb	Pr	Sr	P	Nd	Sm	Zr	Eu	Ti	Gd	Dy	Y	Er	Yb	Lu
HAM12-20 83.22	234.38	360.63	78.70	316.47	276.67	12.90	40.73	189.20	72.78	59.72	232.43	43.48	10.81	15.79	30.13	14.82	12.59	5.15	1.69	5.47	2.65	2.20	2.04	1.78	1.85
HAM12-20 94.40	143.75	321.26	90.57	298.82	199.52	15.29	23.90	182.40	74.38	60.85	227.03	43.84	10.62	14.74	30.43	14.73	13.48	5.35	1.68	6.26	2.65	1.98	1.94	1.83	2.01
HAM12-20 88.86	215.63	340.16	84.42	321.18	320.00	14.59	30.73	177.60	76.42	61.97	237.84	44.93	10.81	15.79	31.61	14.77	14.91	5.30	1.84	5.45	2.56	2.20	2.08	1.70	1.72
HAM12-20 77.63	390.63	387.40	90.28	284.71	364.29	13.88	32.20	189.60	69.87	56.00	227.03	39.86	10.85	16.84	27.55	13.31	13.39	5.04	1.78	4.70	2.56	2.42	2.23	1.85	1.66
HAM12-20 100.29	221.88	385.83	87.57	356.47	280.48	14.45	38.29	190.80	84.86	68.73	227.03	49.64	10.90	16.84	34.42	16.19	14.38	5.49	1.89	5.74	3.05	2.64	2.48	1.68	1.58
HAM12-20 13.26	218.75	332.28	94.00	287.06	178.57	12.76	20.24	186.00	72.34	58.59	237.84	41.67	10.81	13.68	29.17	13.87	13.39	5.65	1.69	6.12	2.82	2.20	2.40	2.17	2.20
HAM12-20 86.30	218.75	349.61	100.44	275.29	428.57	15.15	28.29	188.40	67.69	54.76	248.65	39.49	11.66	13.68	27.70	14.21	13.75	5.77	1.70	5.39	2.27	1.98	1.92	1.58	1.55
HAM12-20 17.52	159.38	283.46	90.43	264.71	173.81	10.24	13.90	175.20	66.67	53.07	254.05	38.04	11.33	12.63	27.03	13.83	13.57	5.60	1.68	5.22	2.16	1.98	1.90	1.64	1.53
HAM12-20 201.01	543.75	620.47	11.30	13.06	542.86	16.97	160.00	177.60	4.15	3.41	81.08	2.39	1.47	27.37	1.71	1.31	1.96	0.60	0.16	0.52	0.43	0.66	0.38	0.57	0.57

Element	FeO
HAM12-20 83.22	1.61
HAM12-20 94.40	1.63
HAM12-20 88.86	1.65
HAM12-20 77.63	1.61
HAM12-20 100.29	1.76
HAM12-20 13.26	1.62
HAM12-20 86.30	1.61
HAM12-20 17.52	1.71
HAM12-20 201.01	0.54

Appendix 4.2 Normalized whole rock data, top row shows data normalized to chondrite (McDonough and Sun, 1995). Second row contains element data normalized to primitive mantle (Hofmann, 1988). The final row is the value of total iron oxide for the tholeiitic vs Calc-alkaline ternary plot

Appendix 5 – LA-ICP-MS Data

Sample Number	Mineral	Paragenetic Phase	Sr	Y	Zr	La	Ce	Pr	Nd	Sm	Eu	Tb	Dy	Ho	Er	Tm	Yb	Lu	Hf	Th	U
NIST612-2.FIN2	**Standard**	~	240.00	75.00	87.00	100.00	160.00	220.00	95.00	87.00	93.00	130.00	130.00	130.00	170.00	160.00	82.00	93.00	86.00	95.00	79.00
NIST612-5.FIN2	**Standard**	~	150.00	56.00	56.00	85.00	94.00	110.00	58.00	60.00	86.00	79.00	65.00	83.00	100.00	86.00	63.00	81.00	72.00	83.00	62.00
NIST612-3.FIN2	**Standard**	~	110.00	53.00	44.00	56.00	62.00	60.00	60.00	46.00	58.00	55.00	46.00	61.00	61.00	61.00	54.00	56.00	57.00	59.00	55.00
NIST612-4.FIN2	**Standard**	~	65.00	32.00	25.00	31.00	34.00	32.00	31.00	28.00	29.00	31.00	23.00	31.00	33.00	33.00	35.00	32.00	29.00	31.00	31.00
MASS1-2.FIN2	**Standard**	~	1.12	0.06	0.35	0.02	0.00	0.00	0.01	0.02	-0.01	0.00	0.00	0.00	0.00	0.00	0.00	0.00	0.00	0.00	0.00
MASS1-5.FIN2	**Standard**	~	1.05	-0.05	0.49	0.02	0.08	0.00	0.01	0.00	0.00	0.00	0.00	0.00	0.00	0.00	0.00	0.00	0.00	0.00	0.00
MASS 1-3.FIN2	**Standard**	~	1.02	-0.01	0.33	0.04	0.02	0.00	0.04	0.00	0.03	0.00	0.00	0.00	0.00	0.00	0.00	0.00	0.01	0.00	0.00
MASS1-1.FIN2	**Standard**	~	0.76	0.00	0.17	0.01	0.01	0.00	-0.01	0.00	-0.01	0.00	0.00	0.00	0.00	0.00	0.00	0.00	0.00	0.00	0.00
CP32 2SP2	**Sphalerite**	**Calcite**	89.10	6.05	~	10.40	17.70	4.42	7.02	1.96	3.32	0.26	1.50	0.29	1.18	0.14	0.53	0.14	~	0.12	~
CP32 2PO3	**Pyrrhotite**	**Calcite**	28.90	5.52	~	13.60	26.30	5.40	9.90	2.70	3.99	0.21	1.26	0.23	1.35	0.05	0.23	0.05	~	0.04	0.06
CP32 2PO4	**Pyrrhotite**	**Calcite**	20.30	9.00	~	22.90	49.00	9.60	21.30	5.10	3.00	0.61	2.80	0.47	2.09	0.22	0.88	0.14	~	0.09	0.19
CP32 2PO5	**Pyrrhotite**	**Calcite**	30.10	5.74	6.30	8.70	19.50	2.82	8.00	2.01	1.71	0.17	2.03	0.29	1.06	0.06	0.14	0.08	~	0.04	0.02
CP32 2SP6	**Sphalerite**	**Calcite**	53.30	6.10	~	11.80	18.70	3.08	7.30	1.32	1.23	0.23	1.10	0.30	0.72	0.06	0.42	0.11	~	0.09	0.03
CP32 2SP7	**Sphalerite**	**Calcite**	25.00	1.61	~	4.60	8.40	1.19	3.30	0.59	0.71	0.05	0.37	0.05	0.17	0.03	0.05	~	~	0.05	0.28
CP32 2PO1	**Pyrrhotite**	**Calcite**	57.90	6.70	~	8.80	19.80	2.35	8.94	2.47	1.79	0.21	1.16	0.31	0.57	0.12	0.27	0.04	~	0.15	0.39
CP32 2PO2	**Pyrrhotite**	**Calcite**	0.85	0.08	~	0.26	0.47	0.06	0.23	0.04	0.02	~	0.01	~	0.01	~	~	~	~	~	0.02
CP32 2SP3	**Sphalerite**	**Calcite**	36.40	6.74	~	6.64	14.50	1.60	7.00	2.06	0.81	0.24	1.16	0.24	0.68	0.10	0.70	0.05	~	0.05	0.03
CP32 2SP4	**Sphalerite**	**Calcite**	~	~	~	~	~	~	~	~	~	~	~	~	~	~	0.02	0.00	~	~	~
CP32 2SP5	**Sphalerite**	**Calcite**	6.30	2.28	~	1.33	3.50	0.52	2.43	0.70	0.16	0.06	0.30	0.08	0.23	0.04	0.20	0.01	~	~	0.03
CP32 2SP1	**Sphalerite**	**Calcite**	25.50	13.60	~	9.94	24.50	2.89	14.30	4.41	1.43	0.58	2.79	0.46	1.19	0.12	0.96	0.08	~	0.03	0.01
CP32 2SP2-DET	**Sphalerite**	**Calcite**	1.73	1.03	0.87	0.04	0.03	0.03	0.34	0.29	0.31	0.02	0.10	0.00	0.05	0.02	0.09	0.00	0.08	0.00	0.02
CP32 2PO3-DET	**Pyrrhotite**	**Calcite**	2.59	1.40	1.49	0.07	0.15	0.00	0.62	0.00	0.76	0.08	0.23	0.00	0.00	0.04	0.00	0.05	0.24	0.00	0.00
CP32 2PO4-DET	**Pyrrhotite**	**Calcite**	2.17	2.26	1.54	0.08	0.07	0.00	0.29	0.35	0.65	0.03	0.17	0.00	0.09	0.10	0.00	0.00	0.13	0.00	0.03
CP32 2PO5-DET	**Pyrrhotite**	**Calcite**	2.41	0.44	1.25	0.12	0.10	0.04	0.48	0.00	0.37	0.05	0.11	0.00	0.00	0.00	0.00	0.03	0.00	0.00	0.00
CP32 2SP6-DET	**Sphalerite**	**Calcite**	1.45	1.15	0.88	0.03	0.07	0.00	0.17	0.00	0.33	0.04	0.14	0.00	0.00	0.02	0.00	0.03	0.00	0.00	0.03
CP32 2SP7-DET	**Sphalerite**	**Calcite**	0.51	0.29	0.28	0.02	0.02	0.00	0.13	0.16	0.10	0.01	0.03	0.00	0.03	0.01	0.00	0.00	0.03	0.00	0.00
CP32 2PO1-DET	**Pyrrhotite**	**Calcite**	2.28	1.32	1.13	0.07	0.09	0.05	0.55	0.31	0.44	0.02	0.00	0.03	0.00	0.03	0.13	0.00	0.11	0.00	0.03
CP32 2PO2-DET	**Pyrrhotite**	**Calcite**	0.04	0.02	0.03	0.00	0.00	0.00	0.00	0.00	0.01	0.00	0.00	0.00	0.00	0.00	0.00	0.00	0.00	0.00	0.00
CP32 2SP3-DET	**Sphalerite**	**Calcite**	0.71	0.11	0.50	0.04	0.05	0.02	0.10	0.13	0.12	0.02	0.09	0.00	0.03	0.01	0.05	0.00	0.10	0.00	0.02
CP32 2SP4-DET	**Sphalerite**	**Calcite**	0.76	0.28	0.61	0.03	0.05	0.00	0.12	0.15	0.16	0.02	0.05	0.02	0.00	0.01	0.00	0.01	0.10	0.00	0.00
CP32 2SP5-DET	**Sphalerite**	**Calcite**	0.97	0.36	0.52	0.02	0.03	0.02	0.21	0.15	0.20	0.03	0.05	0.01	0.04	0.00	0.00	0.04	0.05	0.00	0.03
CP32 2SP1-DET	**Sphalerite**	**Calcite**	0.90	0.37	0.67	0.00	0.04	0.02	0.12	0.15	0.13	0.02	0.00	0.00	0.04	0.00	0.00	0.00	0.00	0.00	0.01

Appendix 5.1 Data calculated using NIST-612 as primary standard for analysis of sample CP32 (12-17-27306). All data shown for each element are measured in ppm. Internal standards used are EPMA concentrations of Fe in pyrrhotite and sphalerite. Detection limits labeled –DET.

Sample Number	Mineral	Paragenetic Phase	Co	Ni	Cu	Zn	Ga	Se	Mo	Ag	Cd	In	Sb	Bi
NIST612-2.FIN2	Standard	~	44.00	41.00	19.00	44.00	43.00	26.00	33.00	22.00	42.00	23.00	39.00	47.00
NIST612-5.FIN2	Standard	~	36.00	75.00	42.00	26.00	30.00	4.00	41.00	24.00	35.00	28.00	29.00	34.00
NIST612-3.FIN2	Standard	~	33.00	77.00	39.00	21.00	28.00	43.00	40.00	24.00	22.00	25.00	25.00	32.00
NIST612-4.FIN2	Standard	~	20.00	53.00	16.00	16.00	20.00	-35.00	28.00	14.00	8.00	16.00	16.00	19.00
MASS1-2.FIN2	Standard	~	66.70	176.50	127900.00	203000.00	51.90	62.00	61.70	64.90	69.50	48.20	54.60	63.70
MASS1-5.FIN2	Standard	~	68.70	183.60	138200.00	209800.00	49.60	52.40	63.30	67.80	72.60	49.80	55.40	66.80
MASS 1-3.FIN2	Standard	~	65.60	182.00	125300.00	200400.00	49.60	47.10	60.10	63.30	66.20	48.70	53.80	63.60
MASS1-1.FIN2	Standard	~	66.10	176.30	135600.00	208800.00	50.40	57.70	60.90	67.80	72.80	50.10	55.10	65.80
CP32 2SP2	Sphalerite	Calcite	234.20	~	1150.00	587000.00	3.58	22.30	~	470.00	916.00	7.79	115.00	~
CP32 2PO3	Pyrrhotite	Calcite	658.00	1250.00	17.00	~	~	~	3.00	690.00	~	~	20.40	~
CP32 2PO4	Pyrrhotite	Calcite	585.00	1443.00	7.60	~	~	~	4.20	14.00	~	~	16.20	~
CP32 2PO5	Pyrrhotite	Calcite	582.00	1260.00	25.00	98.00	~	~	~	13.90	~	~	14.20	1.12
CP32 2SP6	Sphalerite	Calcite	283.80	~	820.00	685000.00	3.30	18.00	~	53.40	1002.00	9.50	38.30	~
CP32 2SP7	Sphalerite	Calcite	131.00	156.00	470.00	120000.00	0.78	3.10	3.30	26.00	200.00	1.60	16.20	0.03
CP32 2PO1	Pyrrhotite	Calcite	587.00	1225.00	7.00	200.00	~	~	2.98	33.80	~	~	24.20	~
CP32 2PO2	Pyrrhotite	Calcite	12.00	26.40	0.32	~	~	~	~	29.00	~	~	20.00	11.00
CP32 2SP3	Sphalerite	Calcite	191.90	~	472.00	468000.00	2.80	9.10	~	51.00	739.00	6.27	27.00	~
CP32 2SP4	Sphalerite	Calcite	108.20	~	13300.00	520000.00	3.93	5.00	~	357.00	1310.00	1.73	3.35	~
CP32 2SP5	Sphalerite	Calcite	231.40	~	3600.00	652000.00	5.19	13.00	~	167.00	1220.00	6.11	42.00	0.02
CP32 2SP1	Sphalerite	Calcite	265.00	~	3700.00	636000.00	3.82	13.00	~	1110.00	1033.00	9.54	202.00	~
CP32 2SP2-DET	Sphalerite	Calcite	0.15	3.22	1.47	3.36	0.28	1.20	0.22	0.27	0.39	0.07	0.07	0.02
CP32 2PO3-DET	Pyrrhotite	Calcite	0.23	5.27	1.78	5.09	0.42	2.00	0.41	0.39	0.50	0.12	0.14	0.02
CP32 2PO4-DET	Pyrrhotite	Calcite	0.23	5.76	2.06	4.64	0.49	2.22	0.48	0.55	0.83	0.08	0.12	0.01
CP32 2PO5-DET	Pyrrhotite	Calcite	0.21	5.35	2.03	4.94	0.47	2.13	0.42	0.42	0.54	0.12	0.13	0.03
CP32 2SP6-DET	Sphalerite	Calcite	0.14	3.82	1.18	2.51	0.31	1.32	0.25	0.28	0.46	0.07	0.07	0.02
CP32 2SP7-DET	Sphalerite	Calcite	0.05	1.38	0.45	1.15	0.12	0.53	0.11	0.10	0.15	0.02	0.03	0.00
CP32 2PO1-DET	Pyrrhotite	Calcite	0.19	5.81	2.03	4.75	0.39	1.98	0.35	0.42	0.53	0.09	0.10	0.03
CP32 2PO2-DET	Pyrrhotite	Calcite	0.01	0.11	0.05	0.09	0.01	0.05	0.01	0.01	0.01	0.00	0.00	0.00
CP32 2SP3-DET	Sphalerite	Calcite	0.09	2.20	0.85	1.86	0.14	0.94	0.18	0.18	0.20	0.02	0.05	0.01
CP32 2SP4-DET	Sphalerite	Calcite	0.10	2.33	0.85	2.27	0.22	0.89	0.23	0.19	0.25	0.04	0.05	0.01
CP32 2SP5-DET	Sphalerite	Calcite	0.09	2.87	0.97	2.53	0.20	1.16	0.21	0.21	0.25	0.05	0.07	0.01
CP32 2SP1-DET	Sphalerite	Calcite	0.10	2.45	0.94	2.80	0.21	1.12	0.22	0.21	0.33	0.03	0.07	0.01

Appendix 5.2 Data calculated using MASS-1 as primary standard for analysis of sample CP32 (12-17-27306). All data displayed is for each element is measured in ppm. Internal standards used are EPMA concentrations of Fe in pyrrhotite and sphalerite. Detection limits labeled –DET.

Sample Number	Mineral	Paragenetic Phase	Co	Ni	Cu	Zn	Ge	As	Se	Ag	Cd	In	Sb	Au	Tl	Bi
NIST612-2.FIN2	**Standard**	~	~	~	~	~	~	~	~	~	~	~	~	~	~	~
NIST612-5.FIN2	**Standard**	~	~	~	~	~	~	~	~	~	~	~	~	~	~	~
NIST612-3.FIN2	**Standard**	~	~	~	~	~	~	~	~	~	~	~	~	~	~	~
NIST612-4.FIN2	**Standard**	~	~	~	~	~	~	~	~	~	~	~	~	~	~	~
MASS1-2.FIN2	**Standard**	~	67.00	179.00	134000.00	207000.00	50.00	65.00	53.00	67.00	70.00	50.00	55.00	47.00	50.00	66.00
MASS1-5.FIN2	**Standard**	~	67.00	179.00	134000.00	207000.00	49.90	65.00	53.00	67.00	70.00	50.00	55.00	46.90	50.00	66.00
MASS 1-3.FIN2	**Standard**	~	67.00	181.00	135000.00	208000.00	50.00	65.00	53.00	67.00	70.00	50.00	55.00	47.00	50.00	66.00
CP26 1PO2	**Pyrrhotite**	**Calcite**	0.95	1.70	1.83	0.23	0.07	27.40	~	0.76	~	~	10.70	0.00	0.33	0.02
CP26 1PY1	**Pyrite**	**Rhodochrosite**	29.10	0.50	0.47	0.28	~	2.70	2.20	0.22	0.01	~	0.13	0.02	0.03	0.46
CP26 1PO3	**Pyrrhotite**	**Calcite**	56.30	29.30	24.50	0.37	0.12	8.27	~	21.60	0.01	~	88.00	0.02	1.44	0.34
CP26 1PY2	**Pyrite**	**Rhodochrosite**	31.70	4.06	0.17	~	~	~	1.60	0.60	0.01	~	0.08	~	0.07	4.30
CP26 1PO4	**Pyrrhotite**	**Calcite**	83.00	70.00	18.30	0.33	0.21	14.70	~	11.90	~	~	64.00	~	0.79	4.20
CP261PY3	**Pyrite**	**Rhodochrosite**	36.40	6.40	0.32	~	~	~	~	0.20	~	~	0.42	~	~	1.14
CP262PY1	**Pyrite**	**Rhodochrosite**	106.00	187.00	12.40	~	0.05	~	~	2.45	~	~	0.10	~	1.61	0.01
CP262PY2	**Pyrite**	**Rhodochrosite**	51.50	29.10	21.60	0.29	0.09	2.55	~	9.51	0.03	~	1.63	~	1.07	0.29
CP262PY3	**Pyrite**	**Rhodochrosite**	54.40	35.50	~	~	~	~	~	~	~	~	~	~	~	0.02
CP262PY4	**Pyrite**	**Rhodochrosite**	57.30	42.30	0.75	~	~	~	2.00	~	0.09	~	~	~	~	0.04
CP262PY5	**Pyrite**	**Rhodochrosite**	49.70	32.40	0.21	0.40	~	~	~	~	0.02	~	~	0.02	0.05	0.02
CP26 1PO2-DET	**Pyrrhotite**	**Calcite**	0.00	0.02	0.00	0.01	0.00	0.00	0.01	0.00	0.00	0.00	0.00	0.00	0.00	0.00
CP26 1PY1-DET	**Pyrite**	**Rhodochrosite**	0.00	0.09	0.03	0.07	0.01	0.02	0.03	0.01	0.01	0.00	0.00	0.00	0.00	0.00
CP26 1PO3-DET	**Pyrrhotite**	**Calcite**	0.00	0.03	0.01	0.03	0.00	0.01	0.01	0.00	0.00	0.00	0.00	0.00	0.00	0.00
CP26 1PY2-DET	**Pyrite**	**Rhodochrosite**	0.00	0.08	0.02	0.06	0.01	0.01	0.03	0.01	0.01	0.00	0.00	0.00	0.00	0.00
CP26 1PO4-DET	**Pyrrhotite**	**Calcite**	0.00	0.04	0.02	0.04	0.00	0.01	0.02	0.00	0.00	0.00	0.00	0.00	0.00	0.00
CP261PY3-DET	**Pyrite**	**Rhodochrosite**	0.01	0.14	0.06	0.14	0.01	0.02	0.06	0.01	0.01	0.00	0.00	0.01	0.00	0.00
CP262PY1-DET	**Pyrite**	**Rhodochrosite**	0.00	0.06	0.02	0.06	0.01	0.01	0.02	0.00	0.01	0.00	0.00	0.00	0.00	0.00
CP262PY2-DET	**Pyrite**	**Rhodochrosite**	0.00	0.06	0.02	0.05	0.01	0.01	0.02	0.00	0.01	0.00	0.00	0.00	0.00	0.00
CP262PY3-DET	**Pyrite**	**Rhodochrosite**	0.01	0.17	0.05	0.12	0.02	0.03	0.06	0.01	0.01	0.00	0.00	0.01	0.00	0.00
CP262PY4-DET	**Pyrite**	**Rhodochrosite**	0.00	0.14	0.06	0.13	0.01	0.02	0.06	0.01	0.02	0.00	0.00	0.01	0.00	0.00
CP262PY5-DET	**Pyrite**	**Rhodochrosite**	0.00	0.10	0.05	0.12	0.01	0.02	0.04	0.01	0.00	0.00	0.00	0.00	0.01	0.00

Appendix 5.3 Data calculated using MASS-1 standard for analysis of sample CP26 (12-17-13792). All data displayed for each element is measured in ppm. Internal standards used are EPMA concentrations of Fe in pyrrhotite and sphalerite. Detection limits labeled –DET.

Sample Number	Mineral	Paragenetic Phase	Co	Cu	Zn	Ga	Se	Ag	Cd	In
NIIST612-1.FIN2	**Standard**	~	50.00	47.00	30.00	47.00	-18.00	14.00	45.00	43.00
NIST612-2.FIN2	**Standard**	~	-10.00	-13.00	-8.00	-10.00	9.00	-2.00	-6.00	-11.00
NIST612-5.FIN2	**Standard**	~	34.00	31.00	29.00	26.00	23.00	12.00	26.00	25.00
NIST612-3.FIN2	**Standard**	~	29.00	33.00	49.00	25.00	-14.00	20.00	17.00	24.00
NIST612-4.FIN2	**Standard**	~	22.00	21.00	6.00	19.00	31.00	15.00	15.00	17.00
MASS1-2.FIN2	**Standard**	~	67.50	134400.00	208000.00	48.90	48.00	66.60	68.50	50.10
MASS1-4.FIN2	**Standard**	~	67.50	137800.00	211000.00	50.60	63.00	67.90	76.80	49.90
MASS1-5.FIN2	**Standard**	~	66.90	131800.00	203400.00	51.40	44.00	66.50	66.30	50.50
MASS 1-3.FIN2	**Standard**	~	65.50	129400.00	206100.00	50.00	54.00	66.50	71.10	49.80
MASS1-1.FIN2	**Standard**	~	67.60	137500.00	209200.00	49.50	53.00	67.40	70.50	50.00
C23 1SP1	**Sphalerite**	**Rhodochrosite**	224.00	51.50	670000.00	2.12	9.00	5.01	1216.00	0.12
C23 1SP2	**Sphalerite**	**Rhodochrosite**	236.00	15.40	631000.00	0.34	13.00	2.45	1081.00	~
C23 1SP3	**Sphalerite**	**Rhodochrosite**	239.80	53.00	633000.00	3.30	~	4.69	1218.00	~
C23 1SP4	**Sphalerite**	**Rhodochrosite**	201.00	16.40	638000.00	~	17.70	3.87	1219.00	~
C23 2SP1	**Sphalerite**	**Rhodochrosite**	291.30	20.10	644000.00	2.69	7.00	3.51	1169.00	11.66
C23 2SP2	**Sphalerite**	**Rhodochrosite**	307.60	24.80	649000.00	2.92	19.00	2.10	1184.00	19.60
C23 2SP3	**Sphalerite**	**Rhodochrosite**	48.50	25.80	607000.00	7.57	10.00	2.58	1079.00	9.91
C23 2SP4	**Sphalerite**	**Rhodochrosite**	73.10	26.40	573000.00	6.76	6.00	2.55	1042.00	15.21
C23 3SP1	**Sphalerite**	**Rhodochrosite**	157.00	20.00	579000.00	1.17	11.00	3.60	1126.00	0.07
C23 3SP2	**Sphalerite**	**Rhodochrosite**	130.80	17.90	655000.00	1.80	16.00	2.81	1085.00	2.35
C23 3SP3	**Sphalerite**	**Rhodochrosite**	154.10	130.00	540000.00	3.34	10.10	8.40	1078.00	0.07
C23 3SP4	**Sphalerite**	**Rhodochrosite**	214.00	11.90	677000.00	~	9.40	3.70	1094.00	0.41
C23 1SP1-DET	**Sphalerite**	**Rhodochrosite**	0.14	1.31	12.54	0.26	1.17	0.22	0.41	0.02
C23 1SP2-DET	**Sphalerite**	**Rhodochrosite**	0.14	0.95	11.77	0.26	1.24	0.25	0.39	0.02
C23 1SP3-DET	**Sphalerite**	**Rhodochrosite**	0.15	1.10	13.59	0.25	1.17	0.26	0.38	0.02
C23 1SP4-DET	**Sphalerite**	**Rhodochrosite**	0.12	1.10	11.00	0.23	1.32	0.19	0.39	0.02
C23 2SP1-DET	**Sphalerite**	**Rhodochrosite**	0.11	0.88	10.00	0.22	1.14	0.19	0.37	0.02
C23 2SP2-DET	**Sphalerite**	**Rhodochrosite**	0.14	0.88	9.68	0.18	1.15	0.21	0.39	0.02
C23 2SP3-DET	**Sphalerite**	**Rhodochrosite**	0.12	1.38	11.90	0.25	1.25	0.18	0.36	0.02
C23 2SP4-DET	**Sphalerite**	**Rhodochrosite**	0.13	1.28	10.84	0.21	1.15	0.22	0.24	0.01
C23 3SP1-DET	**Sphalerite**	**Rhodochrosite**	0.12	1.08	9.51	0.15	1.03	0.20	0.24	0.01
C23 3SP2-DET	**Sphalerite**	**Rhodochrosite**	0.13	1.04	11.41	0.17	0.99	0.22	0.33	0.02
C23 3SP3-DET	**Sphalerite**	**Rhodochrosite**	0.09	0.99	9.29	0.18	0.87	0.16	0.29	0.01
C23 3SP4-DET	**Sphalerite**	**Rhodochrosite**	0.09	1.01	10.08	0.19	1.10	0.21	0.29	0.01

Appendix 5.4 Data calculated using MASS-1 standard for analysis of sample C23 (12-18-18450). All data displayed for each element is measured in ppm. Internal standards used are EPMA concentrations of Fe in pyrrhotite and sphalerite. Detection limits labeled –DET.

Appendix 6 – Microthermometric Data

Sample Number	FIA	Tm	Th	NaCl equiv	%Lw
Calcite					
12-19-17587	FIA 33	-5.30	250.00	8.28	80.00
17587	FIA 33	-5.20	270.00	8.14	75.00
17587	FIA 33	-5.70	255.00	8.81	80.00
17587	FIA 33	-6.00	251.00	9.21	85.00
17587	FIA 33	-5.50	252.00	8.55	80.00
17587	FIA 34	-6.10	232.00	9.34	85.00
17587	FIA 34	-6.20	215.00	9.47	80.00
17587	FIA 34a	-6.50	231.00	9.86	70.00
17587	FIA 34b	-5.90	220.00	9.08	60.00
Quartz I					
12-18-18054	FIA 3	-3.80	279.80	6.16	90.00
18054	FIA 3	-3.20	278.20	5.26	90.00
18054	FIA 3a	-3.40	278.50	5.56	50.00
18054	FIA 4	-3.90	271.10	6.30	90.00
18054	FIA 4	-4.80	270.40	7.59	90.00
18054	FIA 4a	-5.20	272.30	8.14	70.00
18054	FIA 5a	-3.90	268.10	6.30	70.00
18054	FIA 5	-3.80	288.60	6.16	80.00
18054	FIA 5	-3.80	~	6.16	80.00
18054	FIA 6	-3.60	269.50	5.86	80.00
18054	FIA 6	-4.10	278.80	6.59	80.00
18054	FIA 6a	-3.40	310.70	5.56	95.00
18054	FIA 7	-4.10	279.90	6.59	70.00
12-18-18005	FIA 10	-2.70	274.20	4.49	90.00
18005	FIA 10	-2.70	272.60	4.49	90.00
18005	FIA 10a	-2.60	277.70	4.34	70.00
18035	FIA 14	-3.10	281.10	5.11	80.00
12-18-18035	FIA 14a	-2.20	280.30	3.71	70.00
18035	FIA 16	-2.10	281.30	3.55	80.00
18035	FIA 16	-2.10	280.80	3.55	80.00
18035	FIA 17	-2.10	287.80	3.55	75.00
18035	FIA 17	-2.20	287.10	3.71	70.00

Appendix 6.1 shows microthermometric data for fluid inclusions. Temperature (Tm, Th) shown is measured in °C unless otherwise stated. NaCL equiv. is measured in wt.%.

Sample Number	FIA	Tm	Th	NaCl equiv	%Lw
Rhodochrosite					
12-18-18035	FIA 18	-9.10	272.30	12.96	80.00
18035	FIA 19	-6.10	267.50	9.34	95.00
18035	FIA 20	-5.70	~	8.81	95.00
18035	FIA 20	-6.00	277.70	9.21	90.00
18035	FIA 21	-6.10	273.10	9.34	90.00
18035	FIA 22	-8.10	293.10	11.81	75.00
12-18-18450	FIA 23	-6.00	275.40	9.21	90.00
18450	FIA 24	-6.20	273.50	9.47	70.00
18450	FIA 25	-5.50	274.60	8.55	75.00
18450	FIA 26	-4.10	274.90	6.59	70.00
12-18-18054b	FIA 27	-5.40	274.40	8.41	90.00
18054b	FIA 28	-5.70	278.10	8.81	90.00
18054b	FIA 29	-6.10	275.70	9.34	80.00
18054b	FIA 29a	-6.00	275.50	9.21	90.00
18054b	FIA 30	-2.00	205.00	3.39	80.00
18054b	FIA 31	-5.10	290.00	8.00	80.00
18054b	FIA 32	-4.80	292.00	7.59	85.00
Quartz II					
12-18-13223	FIA 1	-4.70	199.40	7.45	90.00
13223	FIA 1	-4.30	~	6.88	90.00
13223	FIA 1	-3.90	198.90	6.30	95.00
13223	FIA 2	-4.00	195.40	6.45	95.00
13223	FIA 2	-4.30	~	6.88	95.00
13223	FIA 2	-4.10	195.10	6.59	95.00
12-17-8269	FIA 8	-2.30	186.10	3.87	95.00
8269	FIA 9	-3.90	~	6.30	95.00
8269	FIA 9	-4.10	178.70	6.59	95.00
12-18-18005	FIA 11	-2.70	198.00	4.49	90.00
18005	FIA 11	-1.50	188.00	2.57	95.00
18005	FIA 11	-1.40	199.00	2.41	90.00
18035	FIA 12	-1.20	220.70	2.07	95.00
18035	FIA 12	-1.10	176.70	1.91	95.00
18035	FIA 12	-1.20	168.00	2.07	95.00
18035	FIA 13	-1.20	165.00	2.07	95.00
18035	FIA 15	-2.10	180.20	3.55	95.00
18035	FIA 15	-2.20	175.30	3.71	90.00

Appendix 6.1 Continued

Appendix 7 – Geochronological Data

	Weight (mg)	U (ppm)	Th (ppm)	Pb (ppm)	Th/U	TCPb (pg)	$^{206}Pb/^{204}Pb$	$^{206}Pb/^{238}U$		$^{207}Pb/^{235}U$		$^{207}Pb/^{206}Pb$		r
Sample Number: 20-154-85														
1	2.90	2215.28	808.49	100.53	0.36	5.16	3262.61	0.04	0.00	0.75	0.00	0.13	0.00	0.95
2	5.50	1300.09	315.51	49.48	0.24	4.12	4098.48	0.04	0.00	0.44	0.00	0.09	0.00	0.95
3	5.00	270.16	39.31	7.72	0.15	4.21	562.09	0.03	0.00	0.28	0.00	0.08	0.00	0.48

Model Ages (Ma)

$^{206}Pb/^{238}U$		$^{207}Pb/^{235}U$		$^{207}Pb/^{206}Pb$		%Disc
263.38	0.34	567.71	0.64	2102.41	0.81	89.19
237.83	0.34	372.17	0.50	1326.27	1.02	83.55
172.51	0.25	251.09	0.78	1070.23	6.18	84.99

Model 2 Solution (±95%-conf.) on 3
Lower intercept 161±530Ma
Upper intercept 2969±8900Ma
MSWD=14872 Probability of fit=0

Appendix 7.1 Data for geochronology of zircon including the isotopic ratios, ages (highlighted in grey), model age and errors

Sample Name	**^{206}Pb (cps)**	**^{204}Pb (cps)**	**^{207}Pb/^{206}Pb**	**2 s**	**^{207}Pb/^{235}U**	**2 s**	**^{206}Pb/^{238}U**	**2 s**	**r**
MON-1A	40778	57	0.05370	0.00087	0.12539	0.00469	0.01693	0.00057	0.902
MON-2B	46298	91	0.05354	0.00074	0.12542	0.00449	0.01699	0.00056	0.924
MON-3A	48556	95	0.06376	0.00131	0.15294	0.00754	0.01740	0.00078	0.909
MON-4A	76861	148	0.06951	0.00422	0.16278	0.01167	0.01698	0.00065	0.530
MON-5A	126680	260	0.07999	0.01000	0.19298	0.02527	0.01750	0.00069	0.299
MON-6A	132337	49	0.05100	0.00057	0.11436	0.00356	0.01626	0.00047	0.934
MON-6B	135440	82	0.05079	0.00065	0.11432	0.00406	0.01632	0.00054	0.934
MON-7A	43905	104	0.05960	0.00234	0.13329	0.00670	0.01622	0.00051	0.626
MON-9A	42048	105	0.05401	0.00092	0.12875	0.00472	0.01729	0.00056	0.886
MON-10A	43117	119	0.05177	0.00076	0.12006	0.00470	0.01682	0.00061	0.928
MON-10B	54021	179	0.06282	0.00361	0.14385	0.00971	0.01661	0.00059	0.526
MON-11A	75339	537	0.12478	0.01657	0.31498	0.04342	0.01831	0.00068	0.268
MON-12A	8086	101	0.11764	0.01463	0.29506	0.03815	0.01819	0.00065	0.275
MON-13A	56854	76	0.05602	0.00154	0.13290	0.00561	0.01721	0.00055	0.757
MON-14A	26449	53	0.05094	0.00138	0.11953	0.00511	0.01702	0.00056	0.773
MON-14B	31739	43	0.05042	0.00094	0.12167	0.00506	0.01750	0.00065	0.895
MON-15A	65494	150	0.07806	0.00890	0.19255	0.02302	0.01789	0.00064	0.301
MON-16A	35363	29	0.05153	0.00086	0.11594	0.00436	0.01632	0.00055	0.896
MON-16B	36137	39	0.05065	0.00088	0.11845	0.00558	0.01696	0.00074	0.929
MON-17A	41451	28	0.05496	0.00168	0.12344	0.00556	0.01629	0.00054	0.733
MON-17B	42001	16	0.05455	0.00196	0.12434	0.00608	0.01653	0.00055	0.679
MON-20A	48214	17	0.05488	0.00108	0.12631	0.00507	0.01669	0.00058	0.870
MON-21A	137662	261	0.07604	0.00600	0.18407	0.01566	0.01756	0.00056	0.374
MON-22A	49931	84	0.06089	0.00428	0.14684	0.01221	0.01749	0.00078	0.535
MON-23A	81018	27	0.05170	0.00072	0.11755	0.00422	0.01649	0.00054	0.921
MON-24A	150978	12	0.04975	0.00059	0.11109	0.00434	0.01619	0.00060	0.953
MON-24B	42482	32	0.05269	0.00162	0.12189	0.00597	0.01678	0.00064	0.779
MON-25A	53850	52	0.05546	0.00112	0.12445	0.00464	0.01627	0.00051	0.839
MON-26A	127385	14	0.05254	0.00124	0.12268	0.00489	0.01694	0.00054	0.805
MON-27A	59365	4	0.05480	0.00096	0.13100	0.00478	0.01734	0.00055	0.876
Standards									
NIG-10	49722	130	0.06487	0.00080	0.24596	0.01028	0.02750	0.00110	0.955
NIG-2	50829	93	0.06831	0.00096	0.25966	0.01149	0.02757	0.00116	0.948
NIG-3	27667	90	0.06972	0.00102	0.26694	0.01092	0.02777	0.00106	0.934
NIG-7	50299	67	0.06452	0.00075	0.24778	0.00921	0.02785	0.00098	0.949
NIG-1	54764	102	0.06963	0.00087	0.26741	0.00891	0.02785	0.00086	0.927
NIG-4	42340	107	0.06928	0.00101	0.26786	0.00955	0.02804	0.00091	0.912
NIG-9	49893	155	0.06485	0.00092	0.25290	0.01207	0.02828	0.00129	0.955
NIG-5	30975	100	0.06455	0.00112	0.25394	0.01060	0.02853	0.00108	0.910
NIG-6	40243	62	0.06498	0.00084	0.25801	0.01187	0.02880	0.00127	0.960
NIG-8	35616	109	0.06539	0.00095	0.26430	0.01761	0.02932	0.00191	0.976

Appendix 7.2 Geochronology of monazites showing the isotopic ratios used to calculate the ages.

Sample Name	**^{207}Pb*/^{206}Pb* age (Ma)**	**2σ error (Ma)**	**^{207}Pb*/^{235}U age (Ma)**	**2σ error (Ma)**	**^{206}Pb*/^{238}U age (Ma)**	**2σ error (Ma)**	**% discordance**
MON-1A	359	36	120	4	108	4	70.4
MON-2B	352	31	120	4	109	4	69.7
MON-3A	734	43	145	7	111	5	85.6
MON-4A	914	120	153	10	109	4	88.9
MON-5A	1197	228	179	21	112	4	91.4
MON-6A	241	25	110	3	104	3	57.3
MON-6B	231	29	110	4	104	3	55.3
MON-7A	589	83	127	6	104	3	83.0
MON-9A	372	38	123	4	110	4	70.9
MON-10A	275	33	115	4	108	4	61.4
MON-10B	702	118	136	9	106	4	85.6
MON-11A	2026	218	278	33	117	4	95.0
MON-12A	1921	208	263	29	116	4	94.8
MON-13A	453	60	127	5	110	3	76.4
MON-14A	238	61	115	5	109	4	54.7
MON-14B	214	42	117	5	112	4	48.2
MON-15A	1148	211	179	19	114	4	90.8
MON-16A	265	38	111	4	104	3	61.1
MON-16B	225	40	114	5	108	5	52.3
MON-17A	411	67	118	5	104	3	75.2
MON-17B	394	79	119	5	106	3	73.8
MON-20A	407	44	121	5	107	4	74.4
MON-21A	1096	150	172	13	112	4	90.5
MON-22A	635	144	139	11	112	5	83.1
MON-23A	272	32	113	4	105	3	61.8
MON-24A	183	27	107	4	104	4	43.9
MON-24B	316	68	117	5	107	4	66.6
MON-25A	431	45	119	4	104	3	76.5
MON-26A	309	53	117	4	108	3	65.5
MON-27A	404	39	125	4	111	4	73.2
Standards							
NIG-10	770	26	223	8	175	7	78.3
NIG-2	878	29	234	9	175	7	81.1
NIG-3	920	30	240	9	177	7	81.9
NIG-7	759	24	225	7	177	6	77.7
NIG-1	917	26	241	7	177	5	81.8
NIG-4	907	30	241	8	178	6	81.4
NIG-9	770	30	229	10	180	8	77.7
NIG-5	760	36	230	9	181	7	77.2
NIG-6	774	27	233	10	183	8	77.4
NIG-8	787	30	238	14	186	12	77.4

Appendix 7.3 Ages of monazites measured using LA-ICP-MS U-Pb. These are highlighted in grey.